Titre: Title:	Influence of Hard Turning on the Surface Characteristics and Fatigue Life of 300M Ultra-High Strenght Steel
Auteur: Author:	Jihane Ajaja
Date:	2019
Type:	Mémoire ou thèse / Dissertation or Thesis
Référence: Citation:	Ajaja, J. (2019). Influence of Hard Turning on the Surface Characteristics and Fatigue Life of 300M Ultra-High Strenght Steel [Thèse de doctorat, Polytechnique Montréal]. PolyPublie. https://publications.polymtl.ca/4139/

POLYTECHNIQUE MONTRÉAL

affiliée à l'Université de Montréal

Influence of Hard Turning on the Surface Characteristics and Fatigue Life of 300M Ultra-High Strength Steel

JIHANE AJAJA

Département de génie mécanique

Thèse présentée en vue de l'obtention du diplôme de *Philosophiae Doctor*

Génie mécanique

Décembre 2019

POLYTECHNIQUE MONTRÉAL

affiliée à l'Université de Montréal

Cette thèse intitulée :

Influence of Hard Turning on the Surface Characteristics and Fatigue Life of 300M Ultra-High Strength Steel

présentée par **Jihane AJAJA**

en vue de l'obtention du diplôme de *Philosophiae Doctor*

a été dûment acceptée par le jury d'examen constitué de :

Marek BALAZINSKI, président

Myriam BROCHU, membre et directrice de recherche

Richard R. CHROMIK, membre et codirecteur de recherche

Étienne PESSARD, membre

Vincent DEMERS, membre externe

DEDICATION

"Perplexity is the beginning of knowledge".

Gibran Khalil Gibran

À Baba & Mama
Adile & Itri
Aymen

ACKNOWLEDGEMENTS

I would like to thank Prof. Myriam Brochu and Prof. Richard Chromik for their guidance and support throughout this project. The knowledge I gained and the abilities I developed with their assistance are invaluable. They inspired me to become a better engineer and researcher with their high level of work ethics.

I would like to thank Dr. Walid Jomaa for his guidance and corrections during my research project. I gained valuable knowledge and experience in working with him.

I would like to thank Prof. Philippe Bocher for his guidance and corrections during the redaction of all my publications. His constructive criticism allowed me to increase the quality of my publications.

I would like to thank Mrs. Cristina del Vasto for the training, help and support she offered me during this project.

I would like to thank Dr. Elvi Dalgaard and Ms. Melinda Bissinger for the opportunities they created for me. Thank you for the flexibility you gave me to help me balance work and school.

Thanks to all my coworkers from Polytechnique Montréal, P&WC and other institutions. Thanks to all my close friends who supported me all these years. They motivated me when the motivation was difficult to find and helped me stay positive when it was hard to be.

Last but certainly not least, I would like to thank my family for their unconditional love and support. Mama, Baba, Adile, Itri. Je ne serais pas là aujourd'hui sans vous. Aymen, merci d'avoir toujours été présent durant ces années où je l'ai été moins. Les mots ne sauront jamais quantifier la gratitude et l'amour que je porte pour chacun d'entre vous.

Last, I would like to thank the Consortium of Research and Innovation in Aerospace in Quebec (CRIAQ), Pratt & Whitney Canada, Héroux-Devtek, the Natural Sciences and Engineering Research Council of Canada (NSERC) and the Mathematics of Information Technology and Complex Systems (MITACS) for supporting my project financially.

RÉSUMÉ

Le tournage dur est un procédé d'usinage fiable utilisé dans le cadre d'opérations de finitions pour les matériaux durs (45 HRC et plus). Ce procédé génère des surfaces ayant des propriétés modifiées qui peuvent être conçues sur mesure, pourvu que les conditions de coupes soient soigneusement sélectionnées. Le tournage étant un procédé complexe impliquant de nombreux paramètres interagissant les uns avec les autres, l'usage d'une technique d'optimisation à objectifs multiples est une approche efficace pour optimiser multiples caractéristiques de surface de façon simultanée.

Les paramètres de coupes de l'usinage dur peuvent être optimisés dans le but de générer une rugosité de surface faible ainsi que des contraintes résiduelles de compression élevées. Ainsi, il est attendu du tournage dur qu'il puisse produire des surfaces adaptées améliorant la performance en fatigue. Toutefois, ceci n'est vrai que si le matériau usiné est exempt de défauts internes pouvant agir comme sites préférentiels pour l'initiation de fissures. Dans le cas des aciers à ultra haute performance tel que le 300M, la résistance à la fatigue est très élevée et la taille critique d'inclusion très faible. Par conséquent, lorsque les défauts internes sont plus sévères que les défauts de surface, ils agissent comme sites préférentiels pour l'initiation de fissures et la fatigue devient un mécanisme interne plutôt qu'un phénomène de surface.

Ce projet comprend deux volets. Tout d'abord, un plan d'expérience fut développé pour évaluer l'influence des paramètres de coupe sur les caractéristiques de surfaces générées par le tournage dur. Un plan Taguchi L9 fut utilisé et quatre facteurs de contrôle – outil de coupe (*T*), vitesse de coupe (*V*), avance (*f*) and profondeur de passe (*D*) – furent évalués à trois différents niveaux (faible, moyen, élevé). Les tests d'usinages furent exécutés et les caractéristiques de surfaces évaluées. Les paramètres de rugosité de surface Ra, Rv and Rz varièrent entre respectivement 0.26 – 1.62 μm, 0.77 – 2.80 μm et 1.36 – 6.76 μm. Les contraintes résiduelles de surface axiales (*ASRS*) et circonférentielles (*HSRS*) varièrent respectivement entre 26 et -953 MPa et 326 et - 384 MPa. L'épaisseur de la couche blanche *WL* varia entre 0.69 et 1.24 μm. Une approche d'optimisation à objectifs multiples fut ensuite utilisée pour déterminer les conditions de coupes optimales permettant de produire des caractéristiques d'intégrité de surface pouvant améliorer la vie en fatigue sur la base des résultats du plan d'expérience. Les paramètres de coupe optimisés permirent de réduire le paramètre de rugosité de surface *Ra* de 50% et d'augmenter les contraintes résiduelles axiales de surface en compression de 307% par rapport à la condition de référence. La condition

optimisée impliqua l'usage d'un outil de coupe céramique composite, d'une vitesse de coupe faible (V = 50 m/min), d'une avance faible (f = 0.051 mm/rev) ainsi que d'une profondeur de passe élevée (D = 0.762 mm).

Ensuite, un ensemble de quatre conditions de coupe fut utilisé pour usiner des spécimens de fatigue dans le but d'évaluer l'influence des caractéristiques de surface générées par le tournage dur de finition sur la vie en fatigue de l'acier 300M ayant une dureté de 55 HRC. Ces conditions exclurent les combinaisons de vitesse de coupe et d'avance élevées pour éviter la création de défauts d'usinage. À nouveau, les tests d'usinages furent exécutés et les caractéristiques de surfaces évaluées. Les caractéristiques d'intégrité de surface *Ra, ASRS* and *HSRS* varièrent respectivement entre 0.30 et 1.21 μm, -438 et 14 MPa et -50 et 131 MPa. Les spécimens de fatigue caractérisés furent assujettis à des essais de fatigue en flexion rotative RR Moore (R = -1) a une contrainte d'amplitude de 965 MPa et une vitesse de rotation de 3300 RPM. Les vies en fatigue obtenues varièrent entre $1.0 \cdot 10^5$ et $9.8 \cdot 10^6$ cycles. Une analyse fractographique démontra que 57% des ruptures en fatigue furent causées par des initiations de fissures à des marques d'usinage en surface tandis que 43% des ruptures en fatigue furent causées par des initiations de fissures à des inclusions en sous-couche. L'ensemble des données de vie en fatigue pu être décrit par une unique distribution Weibull à deux paramètres ce qui démontre que les quatre conditions de coupe évaluées peuvent être considérées équivalentes en termes de vie en fatigue. La compétition entre les mécanismes d'initiation de fissure aux marques d'usinage et aux inclusions en sous-couche dans les échantillons usinées sous les conditions C1, C3 et C4 démontre que ces conditions ne peuvent être optimisées subséquemment. Au besoin, la propreté du matériau devrait être améliorée pour envisager une amélioration supplémentaire de la vie en fatigue. Enfin, il fut démontré que la relation de Murakami permettant la caractérisation de la sévérité des défauts sous-estime les valeurs de K_{max} pour les rugosités de surface.

Les publications formant le noyau de cette thèse sont les premières publiées sur l'acier à ultra haute performance 300M. Les résultats présentés au Chapitre 4 peuvent être utilisées pour la sélection de paramètres de coupe qui permettront de générer des caractéristiques d'intégrité de surface désirées. Les résultats présentés au Chapitre 5 peuvent être utilisés comme référence dans le cadre d'une nouvelle étude sur l'influence du tournage dur sur la vie en fatigue.

ABSTRACT

Hard turning is a reliable machining process used for finishing operations on hardened materials (45 HRC and above). It produces surfaces with altered properties which can be tailored to specific requirements provided cutting conditions are carefully selected. Because turning is a complex process involving many parameters interacting with each other, the use of a multi-objective optimization technique is effective for optimizing multiple surface characteristics simultaneously.

Hard turning cutting parameters can be optimized to generate low surface roughness and highly compressive residual stresses. Thus, it is expected that hard turning can produce engineered surfaces enhancing fatigue performance. However, this is only true if the machined material does not contain internal defects which can act as preferential crack initiation sites. In high strength steels such as 300M, fatigue strengths are very high and critical inclusion sizes very small. Therefore, when internal defects are more severe than surface defects, inclusions act as preferential sites for crack initiation and fatigue becomes an internal mechanism rather than a surface phenomenon.

This project is two-fold. First, a design of experiment (DoE) was developed to investigate the influence of cutting parameters on surface characteristics generated by hard turning. A Taguchi L9 design was used where four control factors – cutting tool (*T*), cutting speed (*V*), feed rate (*f*) and depth of cut (*D*) – were evaluated at three different levels (low, medium, high). Machining tests were performed, and surface characteristics were evaluated. Surface roughness parameters *Ra*, *Rv* and *Rz* varied between 0.26 – 1.62 μm, 0.77 – 2.80 μm and 1.36 – 6.76 μm respectively. Axial (*ASRS*) and hoop (*HSRS*) surface residual stresses varied between 26 and -953 MPa and 326 and - 384 MPa respectively. The white layer *WL* thickness was found to range between 0.69 and 1.24 μm. A multi-objective optimization approach (Taguchi-PCA-GRA) was then used to determine optimum cutting conditions leading to surface integrity characteristics enhancing fatigue life based on results from the DoE. Optimized cutting parameters allowed reducing surface roughness parameter *Ra* by 50% and increasing axial compressive surface residual stresses by 307% with respect to the reference data. Those conditions involved the use of a mixed ceramic tool, a low cutting speed (V = 50 m/min), a low feed rate (f = 0.051 mm/rev) and a high depth of cut (D = 0.762 mm).

Second, a set of four cutting conditions was used to machine fatigue specimens in order to evaluate the influence of surface characteristics on the fatigue life of finish hard turned 55 HRC 300M steel. These conditions excluded combinations of high feed rate and high cutting speed to avoid generating machining defects. Again, machining tests were performed, and surface characteristics evaluated. The resulting average surface integrity characteristics *Ra*, *ASRS* and *HSRS* ranged between respectively 0.30 and 1.21 μm, -438 and 14 MPa and -50 and 131 MPa. Characterized specimens were subjected to RR Moore rotating bending fatigue tests (R = -1) at a stress amplitude of 965 MPa and a rotation speed of 3300 RPM. Resulting fatigue lives ranged between $1.0 \cdot 10^5$ and $9.8 \cdot 10^6$ cycles. A fractographic analysis showed that 57% of fatigue failures initiated from a feed mark while 43% initiated from a subsurface inclusion. The entire fatigue life data set was best described by a single two-parameter Weibull distribution showing that the four cutting conditions evaluated can be considered as equivalent in terms of fatigue life. The competition between crack initiation at feed marks and subsurface inclusions in specimens machined under conditions C1, C3 and C4 shows that those conditions cannot be optimized further. If the need be, the material's cleanliness should be improved to further increase fatigue life. Last, the use of Murakami's equation to characterize the severity of defects was shown to underestimate K_{max} values for surface roughness.

The publications that form the core of this thesis are the first published in the open literature when it comes to 300M ultra-high strength steel. The results presented in Chapter 4 can be used to select hard turning cutting parameters that will generate desired surface integrity characteristics. The results presented in Chapter 5 can be used as a reference to investigate further the influence of hard turning on fatigue life.

TABLE OF CONTENTS

LIST OF TABLES

LIST OF FIGURES

LIST OF SYMBOLS AND ABBREVIATIONS

$\sigma_{app}(d_s)$	Applied stress at crack initiation position [MPa]
$\sigma_{RS}(d_s)$	Axial residual stress at crack initiation position [MPa]
σ_{axial}	Axial stress [MPa]
Δ_{ij}	Difference between comparative and original sequences
ξ	Distinguishing coefficient
λ_i	Eigen value
σ_w	Fatigue strength [MPa]
ϕ	Factor equal to $0.226 + HV \cdot 10^{-4}$
Γ	Grey relational grade (GRG)
γ	Grey relational coefficient (GRC)
σ_h	Hydrostatic stress [MPa]
σ_{hoop}	Hoop stress [MPa]
$\bar{\eta}_i$	Mean value at optimum
$\Delta_{min}, \Delta_{max}$	Minimum and maximum value of Δ_{ij}
σ_{net}	Net applied stress [MPa]
$\hat{\eta}$	Predicted mean of the performance characteristic value
ψ_{ir}	Principal components
α	Scale parameter of the Weibull distribution function
β	Shape parameter of the Weibull distribution function
η_{ij}	Signal-to-noise ratio for surface characteristic *i* and experiment *j*
η_i^*	Signal-to-noise ratio nominal value
η_o	Signal-to-noise ratio for starting condition
ρ	Spearman correlation coefficient

$\sigma_{x_{ij}}$	Standard deviation of x_{ij}
$\sigma_{x_{ir}}$	Standard deviation of x_{ir}
σ_a	Stress amplitude [MPa]
η_m	Total mean of the performance characteristic value
α_j	Weighted PQLR scores
YS	0.2% Yield strength [MPa]
AD	Anderson-Darling statistic
Ra	Arithmetic surface height [μm]
R_Z	Average peak-to-valley height [μm]
R_{ir}	Correlation matrix
V	Cutting speed [m/min]
T	Cutting tool material
D	Depth of cut [mm]
d_s	Distance between the center of an inclusion and the material's surface [μm]
f(x)	Distribution function
el	Elongation (%)
V_{ir}	Eigen vector
N_f	Fatigue life [cycles]
f	Feed rate [mm/rev]
d_i	Inclusion diameter [μm]
i, j	i^{th}surface characteristic, j^{th} experiment
Rku	Kurtosis
k, p	k^{th} replicate, total number of replicates
R_V	Maximum depth of valleys [μm]

Rt, a	Maximum peak-to-valley [μm]
K_{max}	Maximum stress intensity factor [MPa·m^{½}]
$K_{max,surf}$	Maximum surface intensity factor [MPa·m^{½}]
$K_{max,sub}$	Maximum subsurface intensity factor [MPa·m^{½}]
Rsm, b	Mean spacing of the asperities [μm]
x_{ij}	Normalized surface characteristic value (comparative sequence)
q	Number of process parameters
P	Pearson correlation coefficient
Z_{ij}	Principal component scores
x_{io}	Reference sequence for surface characteristic i
Rq	Root mean square [μm]
$\sqrt{\text{area}}$	Root square projected area function [μm]
$\sqrt{area_{inc}}$	Root square projected area function for surface roughness [μm]
$\sqrt{area_R}$	Root square projected area function for inclusions [μm]
$\bar{x}$, $\bar{y}$	Sample mean of first and second variable
Rsk	Skewness
r	Specimen's radius [μm]
S_x, S_y	Standard deviation for sample mean $\bar{x}$ and $\bar{y}$
R	Stress ratio
y_{ijk}	Surface characteristic value for replicate k
y_i^*	Surface characteristic nominal value
m	Total number of surface characteristics
n	Total number of experiments
N	Total number of specimens

w_i	Weighting factor for surface characteristics i
$ASRS$	Axial surface residual stress [MPa]
CPF	Cumulative percent failure
DL	Deformed layer [μm]
DOE	Design of experiment
ECCI	Electron channeling contrast imaging
FM	Feed mark
GRA	Grey relational analysis
HSRS	Hoop surface residual stress [MPa]
PCA	Principal component analysis
PDF	Probability density function
PQLR	Proportion quality loss reduction
SBI	Subsurface inclusion
SI	Surface integrity
UTS	Ultimate tensile strength [MPa]
WL	White layer thickness [μm]

CHAPTER 1 INTRODUCTION

1.1 Context

300M ultra-high strength steel is used in the manufacturing of landing gear components where maximum strength to weight ratios are required. Those components include cylindrical parts such as pistons which are machined by hard turning. Hard turning involves roughing, semi-finishing and finishing operations which generate final parts dimensions and surface integrity. Therefore, since finish hard turning operations are expected to have a direct influence on fatigue performance, they should be optimized to generate surface characteristics that will not promote early fatigue failure, including low surface roughness and highly compressive surface residual stresses.

Considering that landing gear components are subjected to high frequency low amplitude vibrations including break-induced vibrations, the high cycle fatigue behavior of the material is of particular interest. For this reason, the HCF behavior of hard turned 55 HRC 300M steel will be investigated as part of the current research project.

This project is part of MANU510 which is a larger CRIAQ project involving two industrial partners, Héroux-Devtek and Pratt & Whitney Canada, and four universities; École Polytechnique, McGill University, École de Technologie Supérieure and Concordia University. This research collaboration was established to develop links between the various aspects involved with the turning process and resulting surface integrity with the fatigue behavior of 300M and Inconel 718 for landing gear and turbine blade applications respectively.

1.2 Document Organization

This manuscript is an article-based thesis containing seven chapters including two articles.

- Chapter 2 provides a critical review of the literature.
- Chapter 3 presents the methodology and the organization of the document.
- Chapter 4 is an article entitled “Hard turning multi-performance optimization for improving the surface integrity of 300M ultra-high strength steel”. This article addressed the first main objective of this research project.

- Chapter 5 is an article entitled “High cycle fatigue behavior of hard turned 300M ultra-high strength steel”. This article addressed the second main objective of this research project.
- Chapter 6 discusses the general conclusions reported in chapters 4 and 5.
- Chapter 7 establishes the limitation of this work and provides recommendations for future studies on the topics discussed.

CHAPTER 2 CRITICAL LITERATURE REVIEW

This chapter will review the different topics of relevance to the current research project. Section 2.1 and 2.2 will present the material and process to be studied, namely 300M ultra-high strength steel and hard turning. Section 2.3 will discuss the influence of hard turning cutting parameters on the surface integrity of the material. Section 2.4 will discuss the selection of an optimization approach for the case studied while section 2.5 will report on the influence of surface integrity characteristics on the fatigue behavior of the material. Last, section 2.6 will present empirical models developed to predict the fatigue life of high strength steels.

2.1 300M Ultra-High Strength Steel

300M ultra-high strength steel is a medium carbon low alloy steel produced by vacuum arc remelting, a process used to produce high purity steels with very low inclusion content. The "ultra-high strength steel" designation refers to the family of steels with a minimum yield strength of 1380 MPa [8] which includes AISI 4340 from which 300M was derived by increasing the silicon content to a maximum of 1.80% and adding a maximum of 0.10% vanadium per AMS6257E. The addition of silicon to 4340 allowed increasing the tempering temperature to 300°C [9], preventing temper embrittlement. The addition of vanadium allowed restricting grain growth during austenitization [10] resulting in higher [11] and deeper [12] levels of hardenability, increased solid-solution strengthening and better resistance to softening at high temperatures [12]. The required chemical composition as prescribed by the material's standard is presented in Table 1. Following a hardening heat treatment, the material should have a martensitic microstructure and its properties should conform to the minimum longitudinal tensile properties presented in Table 2. The inclusion content is controlled by the material's specification as specified in Table 3. The grain size should be ASTM 6 or finer.

Table 1 : Chemical composition (wt. %) as per AMS6257E.

	C	Mn	Si	P	S	Cr	Ni	Mo	V	Cu	Fe
AMS6257E min.	0.40	0.65	1.45	-	-	0.70	1.65	0.35	0.05	-	bal.
AMS6257E max.	0.44	0.90	1.80	0.010	0.008	0.95	2.00	0.45	0.10	0.35	bal.

Table 2 : Minimum longitudinal tensile properties as per AMS6257E.

Yield strength [MPa]	Tensile strength [MPa]	Elongation [%]
1586	1931	8

Table 3: Inclusion content classified by inclusion type and severity level per AMS6257E.Values correspond to length [µm] or number of counts when in parenthesis.

Inclusion type	Severity	
	Thin	Heavy
A	261.0	127.0
B	76.8	76.8
C	75.6	75.6
D	(9)	(4)

2.2 Hard Turning Process

Hard turning is increasingly replacing the traditionally used grinding process for finishing operations because it provides several advantages over grinding including a reduced processing time [13, 14], a reduction in production costs [14, 15] and greater flexibility [14, 15]. Generally speaking, we refer to hard turning when the material to be machined has a hardness above 45 HRC [16]. The turning process is carried out in a lathe where the cutting tool is fed into a rotating workpiece as shown in Figure 1 a). When the tool moves along the main direction of the workpiece, it removes material and consequently, reduces its diameter. As shown in Figure 1 b), the tool has two faces: the rake face and the flank face. When the tool edge enters the workpiece, the material ahead of the tool shears over the rake face leading to chip formation [17]. As seen in Figure 1 a), there are three main parameters involved with the turning process: the cutting speed V, the feed rate f and the depth of cut D. These parameters are tailored to the turning process depending on if it is a roughing or finishing operation. Roughing operations are carried out to generate the part geometry and involves large amounts of material removal while finishing operations are carried out to achieve final dimensions, tolerances and surface finish, and involves small amounts of material removal. Therefore, the selection of cutting parameters and cutting tools depends on the workpiece material and hardness as well as the type of turning operation.

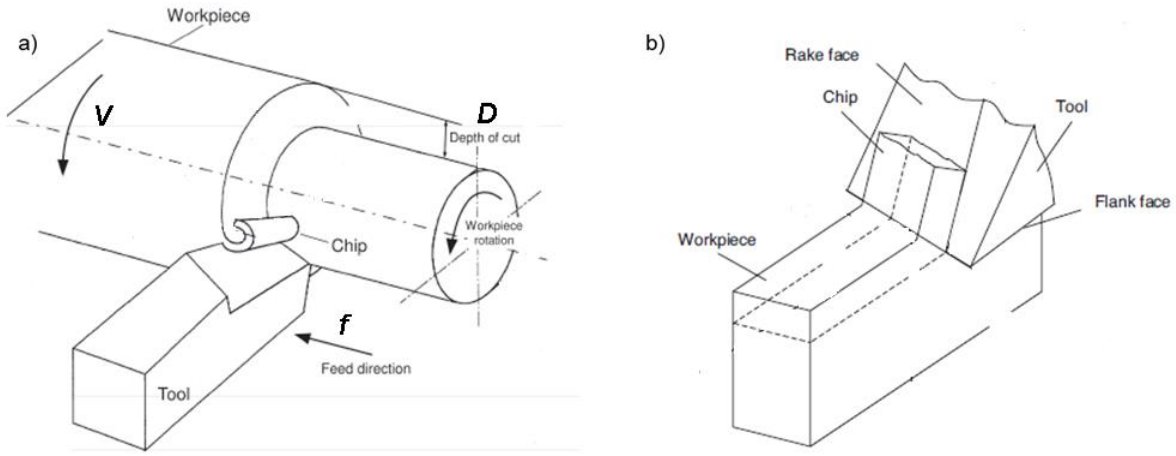

Figure 1 : Turning process (a) and cutting tool geometry (b) [17].

2.3 Influence of Hard Turning on the Surface Integrity of Hardened 4340 and 300M Steels

Machining processes including hard turning are known to alter the surface integrity of materials. Surface integrity is concerned with the topological aspect of a surface and its mechanical and metallurgical characteristics [17, 18]. Those characteristics can be divided into three categories: (i) topological aspects representing deviations from a perfectly flat surface, (ii) mechanical characteristics representing the altered mechanical properties and stress state of the surface and (iii) metallurgical characteristics representing the change in the material's microstructure. Considering the very large number of parameters involved with the cutting process, the following section will report on the influence of four main parameters on surface integrity, namely cutting speed, feed rate, depth of cut and cutting tool material (*T*). Due to the very limited amount of available studies published on 300M, this review will also include studies published on 4340.

Table 4 summarizes the hard turning conditions tested and resulting ranges of surface integrity characteristics published in the gathered literature. Both coated and uncoated tools were used to machine 4340 and 300M hardened steels with hardness varying between 37 and 69 HRC. The following ranges of *f*, *V* and *D* were evaluated: $0.05 \leq f$ [mm/rev] ≤ 0.175, $60 \leq V$ [m/min] ≤ 300 and $0.1 \leq D$ [mm] ≤ 2.5. Most studies only investigated the influence of those parameters on the arithmetic average surface roughness parameter *Ra*. However, few studies also investigated the influence of cutting tool material [19] and workpiece hardness [19, 20] on *Ra* while others investigated the influence of cutting parameters on residual stresses [1, 2, 21, 22]. The range of

cutting conditions evaluated generated *Ra* values ranging between 0.04 and 15.96 µm. They also generated axial and hoop surface residual stress (*ASRS*, *HSRS*) values ranging between 127 and 385 MPa and -54 and 600 MPa respectively.

The following section will discuss the main results and trends reported in the literature. Combined with the tools manufacturer's recommendations, the conclusions drawn from the literature will be used to support the selection of cutting parameters presented in Chapter 3.

Table 4: Literature review of studies on the influence of hard turning on the surface integrity of 4340 and 300M steels.

Ref.	Workpiece material	Workpiece hardness [HRC]	Tool material	*f* [mm/rev]	*V* [m/min]	*D* [mm]	*Ra* [µm]	*ASRS* [MPa]	*HSRS* [MPa]
[23]	4340	49	CVD ceramic coated carbide	0.05, 0.09, 0.13	100, 160, 220	0.2, 0.4, 0.6	0.57 – 0.99	-	-
[24]	4340	45	CVD ceramic coated carbide	0.1, 0.2, 0.3	100, 150, 200	0.5, 1.5, 2.5	3.70 – 5.84	-	-
[25]	4340	48	Ceramic	0.12, 0.18, 0.24	140, 280, 420	0.5, 1.0, 1.5	2.70 – 4.75	-	-
[26]	4340	48	CVD ceramic coated carbide	0.1, 0.18, 0.26	80, 140, 200, 260	0.8, 1.0	0.50 – 2.45	-	-
[27]	4340	69	CBN	0.02, 0.06, 0.1, 0.15	90, 150, 200, 250	0.1, 0.2, 0.3, 0.4	0.04 – 1.14	-	-
[20]	4340	42	Carbide	0.1, 0.2, 0.3, 0.4	60, 120, 180	0.5, 1.0, 1.5, 2.0	0.52 – 6.78	-	-
[20]	4340	50	PCBN	0.1, 0.2, 0.3, 0.4	60, 120, 180	0.5, 1.0, 1.5, 2.0	0.35 – 2.43	-	-
[19]	4340	37	Carbide, CBN, Ceramic	0.08, 0.16, 0.24	60, 90, 120	0.1, 0.2, 0.3	0.48 – 5.06	-	-
[19]	4340	43	Carbide, CBN, Ceramic	0.08, 0.16, 0.24	60, 90, 120	0.1, 0.2, 0.3	1.60 – 9.54	-	-
[19]	4340	46	Carbide, CBN, Ceramic	0.08, 0.16, 0.24	60, 90, 120	0.1, 0.2, 0.3	1.19 – 15.96	-	-
[21]	4340	37	Cermet	0.075, 0.1, 0.125, 0.15, 0.175, 0.2	200, 255, 300	0.5	0.27 – 1.9	127 – 381	-16 – 593
[22]	4340	37	Cermet	0.075, 0.1, 0.125, 0.15, 0.175, 0.2	200, 255, 300	0.4	0.28 – 1.93	154 – 385	123 – 600
[1]	300M	50	CVD ceramic coated carbide	0.1, 0.12, 0.15, 0.17, 0.2	60, 80, 100, 120, 150, 200, 250	0.1, 0.2, 0.3, 0.4, 0.5	0.28 – 1.17	-	-

[1]	300M	50	Ceramic	0.1, 0.12, 0.15, 0.17, 0.2	60, 80, 100, 120, 150, 200, 250	0.1, 0.2, 0.3, 0.4, 0.5	0.28 – 1.17	-	-54 – 270
[2]	300M	52	Ceramic coated ceramic	0.1, 0.2	150	0.2, 0.4	0.42 – 1.82	*	
[3]	300M	47	Ceramic coated carbide	0.1, 0.15, 0.20, 0.25, 0.30	300, 400, 500, 600	0.1, 0.15, 0.20, 0.25, 0.3	0.77 – 3.22	-	-

* Principal residual stresses reported.

2.3.1 Effect of Cutting Parameters, Tool Material and Workpiece Hardness on Surface Roughness

The effect of cutting parameters (*f, V, D*) on surface roughness parameter *Ra* was investigated by all studies reported in Table 4. Because machining tests were performed using different cutting parameters, tool material and workpiece hardness, specific comparisons between studies are difficult. Therefore, this section will discuss the trends obtained between the parameters investigated and surface roughness.

In studies where the contribution of cutting parameters was evaluated using a single cutting tool material, the feed rate *f* was found to contribute the most to *Ra* [21-23, 27]. The only parameter found to have a greater contribution to *Ra* was cutting tool material which was determined in the only study where the cutting tool material was varied. In this study published by Çaydaş et al. [19], the feed rate was found to have the second highest contribution to *Ra* which is consistent with results from other studies.

Figure 2 shows the influence of both *f* and *V* on *Ra* for 48 HRC 4340 steel machined using a ceramic coated carbide tool [26]. Results demonstrate that *Ra* increases with increasing *f* for all cutting speeds, in agreement with results published in [1-3, 20, 21, 23, 24, 27] for both 4340 and 300M steels machined with varying cutting tools (material and coating) and workpiece hardness (37-69 HRC). This was attributed to the higher amount of vibration and heat generation at the tool/workpiece interface resulting from higher cutting forces [23, 24, 26] due to the larger contact area between the cutting tool and workpiece [26]. However, Das et al. [23] also showed that although *Ra* increases with increasing *f* for $0.09 \leq f$ [mm/rev] ≤ 0.13, it decreases with increasing *f* for $0.05 \leq f$ [mm/rev] ≤ 0.09. Figure 2 also shows that *Ra* decreases with increasing *V* and that the sensitivity of *Ra* to *f* increases with increasing cutting speed. A decrease in *Ra* with increasing *V* for $100 \leq V$ [m/min] ≤ 220 was also reported by Das et al. [23].This was attributed to either softening of the workpiece material resulting in decreasing cutting forces [19, 23, 26] or reduced built-up edge at the chip/tool interface resulting in improved surface finish [23]. However, other studies reported varying trends for different ranges of cutting speed. Chinchanikar et al. [24] showed that for $f = 0.2$ mm/rev and $D = 1.5$ mm, *Ra* decreases between 100 and 150 m/min and plateaus between 150 and 200 m/min. Similarly, Zheng et al. [3] showed that for $f = 0.15$ mm/rev and $D = 0.15$ mm, *Ra* increases between 200 m/min and 400 m/min and plateaus between 400 and

600 m/min. Singh et al. [25] reported that for f = 0.18 mm/rev and D = 1.0 mm, *Ra* increases between 140 and 280 m/min and decreases between 280 and 420 m/min. Similarly, Zhang et al. [1] showed that for 50 HRC 300M steel machined using a ceramic coated carbide tool, *Ra* increases between 60 and 120 m/min and decreases between 120 and 250 m/min for f = 0.1 mm/rev and D = 0.2 mm. Nevertheless, it showed that for the same cutting parameters, *Ra* decreases with increasing V when using a ceramic tool.

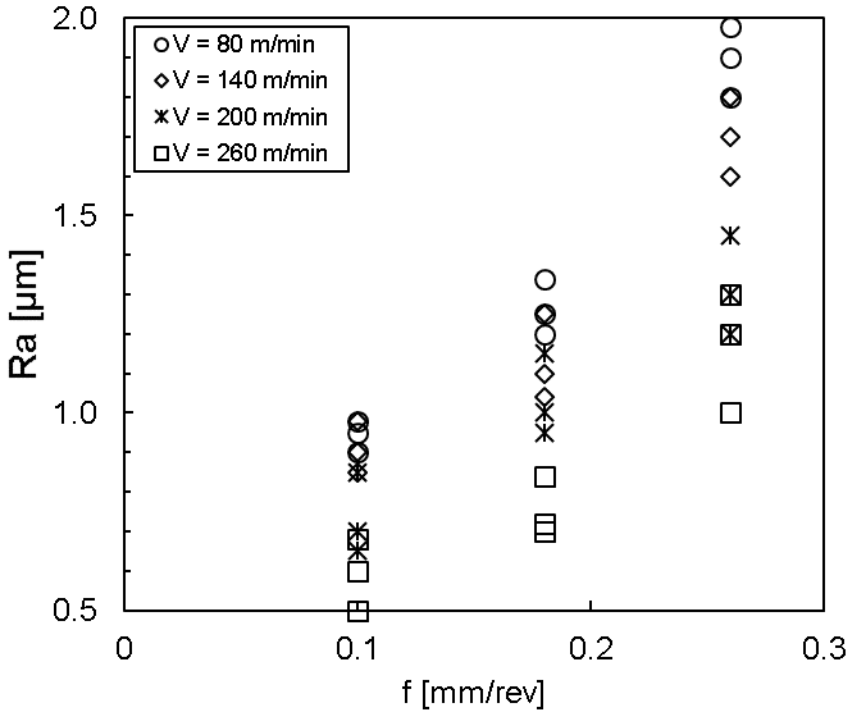

Figure 2:Influence of f and V on *Ra* at constant D = 1.0 mm based on data from Suresh et al. [26].

The analysis of the trends between D and *Ra* was inconclusive. Singh et al. [25] reported an increase in *Ra* with increasing D for all feed rates and cutting speeds evaluated. Similarly, Chinchanikar et al. [24] reported an increase in *Ra* with increasing D at f = 0.2 mm/rev and V = 150 m/min. Results reported by Suresh et al. [26] show an increase in *Ra* with increasing D for f = 0.1 mm/rev and V = 80 m/min while it shows a decrease in *Ra* with increasing D for f = 0.26 mm/rev and V = 260 m/min. Finally, results published by Zheng et al. [3] demonstrate an increase in *Ra* for $0.1 \leq D$ [mm] ≤ 0.2 while they show a plateau for $0.15 \leq D$ [mm] ≤ 0.3 at f = 0.15 mm/rev and V = 500 m/min.

Both Lima et al. [20] and Zhang et al. [1] reported tool-dependent results. Using an uncoated carbide tool combined with a feed rate of 0.2 mm/rev and a depth of cut of 120 m/min, Lima et al. [20] observed a plateau in *Ra* between 0.5 and 1.5 mm followed by an increase in *Ra* between 1.5 and 2.0 mm. However, results generated using a PCBN tool were found to be insensitive to variations in *D*. Similarly, Zhang et al. [1] reported no variation in *Ra* with respect to *D* when using a coated carbide tool while they reported a decrease in *Ra* for $0.1 \leq D$ [mm] ≤ 0.2 and an increase in *Ra* for $0.2 \leq$ D [mm] ≤ 0.5 at $f = 0.1$ mm/rev and $V = 100$ m/min when using an uncoated ceramic tool.

In summary, the analysis of the results published in the literature shows the complexity of the relationship between hard turning cutting parameters and surface roughness. Overall, there is an agreement on the importance of the contribution of feed rate to *Ra*. Different combinations of parameters generated similar *Ra* values and trends varied according to ranges of parameters evaluated. Therefore, for each study reviewed, cutting conditions leading to minimum and maximum Ra values are reported in Table 5. For the purpose of the current research project, the assessment of the influence of finish cutting conditions on surface roughness in hard turned 55 HRC will require the investigation of both the effect of tool material and cutting parameters *f*, *V* and *D*. Further, considering that all studies focused only on surface roughness parameter *Ra*, other surface roughness parameters should be evaluated including amplitude, spacing and statistical parameters. Last, since different combinations of cutting parameters lead to similar roughness values, surface profiles should be analyzed to determine if they demonstrate similar characteristics.

Table 5: Summary of cutting conditions generating minimum and maximum *Ra* values.

Ref.	Workpiece material	Workpiece hardness [HRC]	Tool material	f [mm/rev]	V [m/min]	D [mm]	min. Ra [µm]	max. Ra [µm]
[23]	4340	49	CVD ceramic coated carbide	0.09	220	0.2	0.57	
				0.05	100	0.2		0.99
[24]	4340	45	CVD ceramic coated carbide	0.1	150	1.5	3.70	
				0.3	150	1.5		5.84
[25]	4340	48	Ceramic	0.12	420	0.5	2.70	
				0.18	280	1.5		4.75
[26]	4340	48	CVD ceramic coated carbide	0.1	260	0.8	0.50	
				0.26	80	0.8		2.45
[27]	4340	69	CBN	0.02	90	0.1	0.04	
				0.15	250	0.1		1.14
[20]	4340	50	PCBN	0.1	120	1	0.35	
		42	Carbide	0.4	120	1		6.78
[19]	4340	37	CBN	0.08	60	0.1	0.48	
		46	Carbide	0.24	60	0.3		15.96
[21]	4340	37	Cermet	0.075	200	0.5	0.27	
				0.2	300	0.5		1.9
[22]	4340	37	Cermet	0.075	200	0.4	0.28	
				0.2	300	0.4		1.93
[1]	300M	50	CVD ceramic coated carbide	0.1	60	0.2	0.28	
				0.1	120	0.2		1.29
[2]	300M	52	Ceramic coated ceramic	0.1	150	0.2	0.42*	
				0.2	150	0.4		1.82*
[3]	300M	47	Ceramic coated carbide	0.1	500	0.15	0.77	
				0.3	500	0.15		3.22

* Different tool edge preparation

2.3.2 Effect of Cutting Parameters on Residual Stresses

The effect of cutting parameters on residual stresses generated by hard turning of 4340 and 300M steels was investigated by a few authors only [2, 21, 22, 28]. Coto et al. [21] and Navas et al. [22] both investigated the influence of cutting parameters on axial (*ASRS*) and hoop (*HSRS*) surface residual stresses generated by hard turning of 37 HRC 4340 steel machined using an uncoated cermet tool. Figure 3 gathers their results and demonstrate both the effect of *f* and *V* on *ASRS*. Figure 3 a) shows the data for constant *D* = 0.5 mm while Figure 3 b) shows the data for *D* = 0.4 mm. For all feed rates, an increase in *V* led to a decrease in tensile *ASRS* with the exception where *f* = 0.075 mm/rev and *D* = 0.4 mm. In this case, *ASRS* are found to become less tensile with increasing *V* between 200 and 255 m/min while they are found to become more tensile with increasing *V* between 255 and 300 m/min. Further, results show that higher feed rates usually generate higher tensile *ASRS* with again, the exception where *f* = 0.075 mm/rev and *D* = 0.4 mm which generated the highest amount of tensile *ASRS* at 200 and 300 m/min. Overall, none of the conditions studied generated compressive *ASRS*.

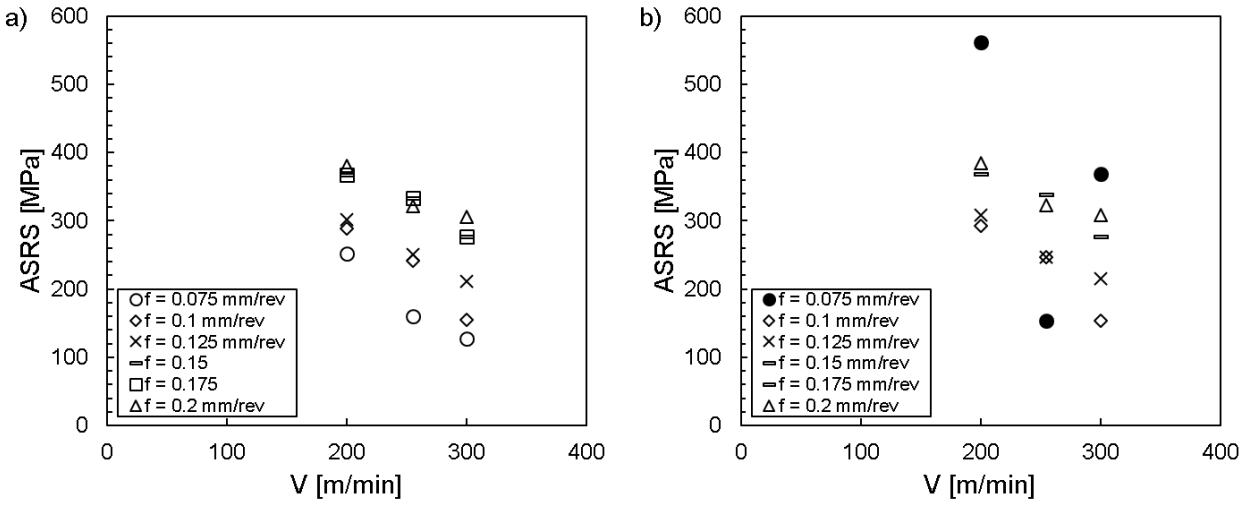

Figure 3: Influence of *f* and *V* on *ASRS* for a) *D* = 0.5 mm based on [21] and b) *D* = 0.4 mm based on data from Navas et al. [22].

Figure 4 shows the influence of both *f* and *V* on *HSRS*. Figure 4 a) shows the data for constant *D* = 0.5 mm while Figure 4 b) shows the data for *D* = 0.4 mm. As for *ASRS*, *HSRS* become less tensile at higher cutting speeds with the exception where *f* = 0.075 mm/rev and *D* = 0.4 mm. In this case, H*SRS* are found to become more tensile with increasing *V* between 200 and 255 m/min while they

are found to become less tensile with increasing *V* between 255 and 300 m/min (reverse trend with respect to *ASRS*).

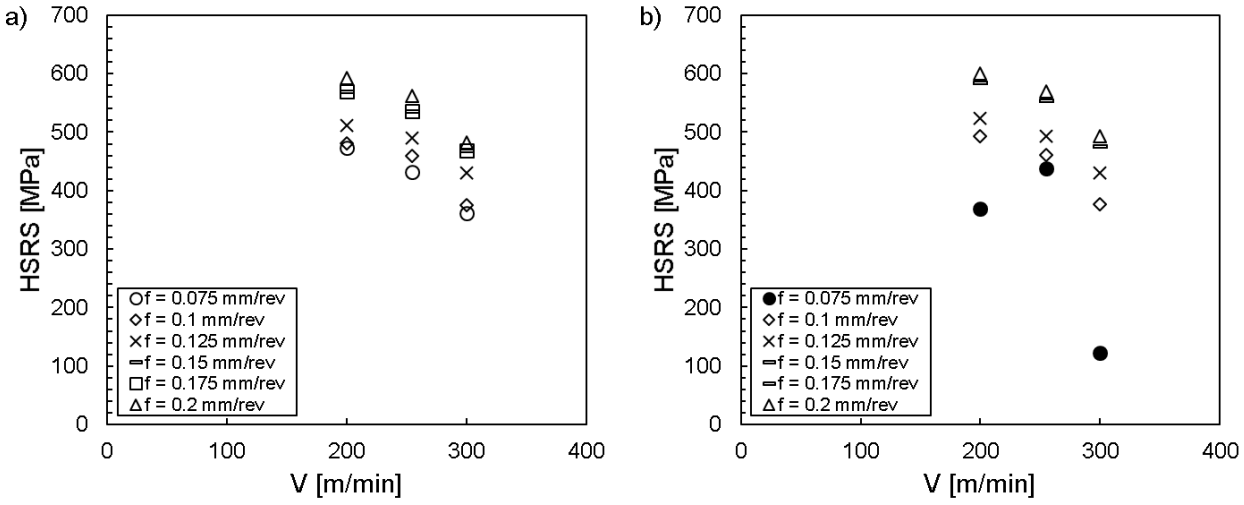

Figure 4: Influence of *f* and *V* on *HSRS* for a) *D* = 0.5 mm based on [21] and b) *D* = 0.4 mm based on data from Navas et al. [22].

Results reported by Zhang et al. [1] on residual stresses generated by hard turning of 50 HRC 300M steel, show that for a 140 m/min increase in *V*, *HSRS* increased from -54 to 269 MPa for constant *f* = 0.1 mm/rev and *D* = 0.2 mm. However, the opposite trend was observed when varying *D*. At constant *f* = 0.1 mm/rev and *V* = 100 m/min, a 0.5 mm increase in *D* was found to shift *HSRS* from tensile (204 MPa) to compressive (-46 MPa). Also, results show a decrease in tensile *HSRS* for $0.1 \leq f\,[\text{mm/rev}] \leq 0.15$ while they show an increase in tensile *HSRS* for $0.15 \leq f\,[\text{mm/rev}] \leq 0.2$.

Figure 5 shows the influence of cutting speed on hoop residual stress profiles. Increasing *V* was found to increase significantly the maximum compressive residual stress beneath the surface. However, its position was found to be located at around 20 µm and to plateau at around 50 µm for all cutting speeds. Figure 6 shows the influence of feed rate on hoop residual stress profiles. Results show that increasing *f* has the same influence as increasing *V*. Finally, Figure 7 shows the influence of *D* on hoop residual stress profiles. Increasing *D* from 0.2 to 0.7 mm generated both a significant increase in the maximum compressive residual stress and shifted its position deeper below the surface.

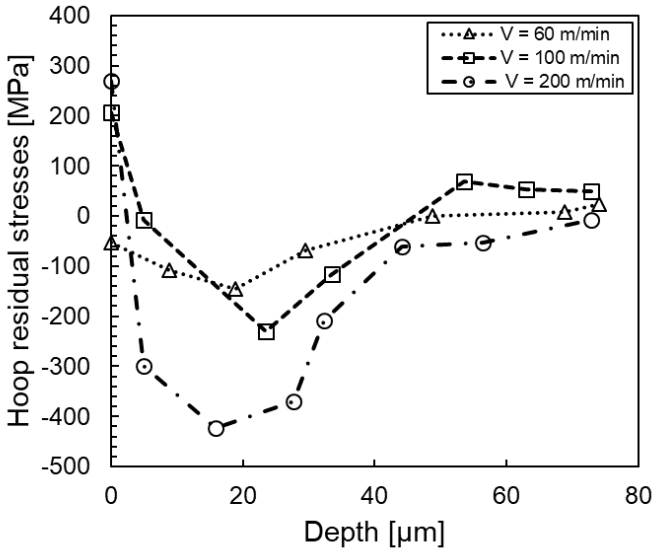

Figure 5: Influence of cutting speed on hoop residual stress profiles for constant f = 0.1 mm/rev and D = 0.2 mm based on data from Zhang et al. [1].

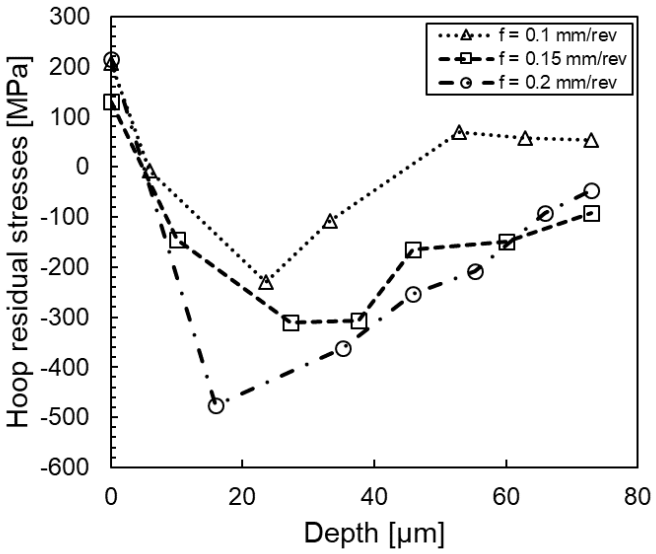

Figure 6: Influence of feed rate on hoop residual stress profiles for constant V = 100 m/min and D = 0.2 mm based on data from Zhang et al. [1].

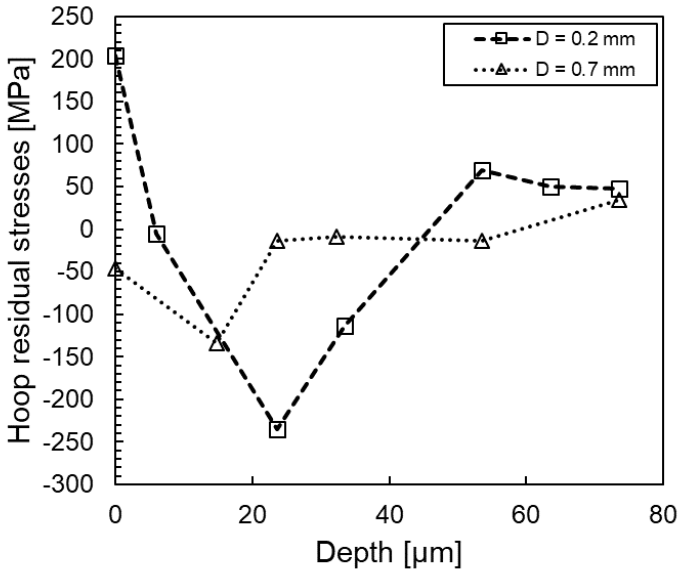

Figure 7: Influence of depth of cut on hoop residual stress profiles for constant f = 0.1 mm/rev and V = 100 m/min based on data from Zhang et al. [1].

In summary, the analysis of the influence of cutting parameters *f, V* and *D*, on residual stresses show some differences between the limited amount of results published on 4340 and 300M steels, mainly due to differences in the cutting parameters studied. While an increase in *V* was found to generate a decrease in tensile *HSRS* for hard turned 4340, the reverse trend was obtained for 300M. However, the same conclusion was drawn for both materials with respect to the effect of *f* ; results demonstrated that increasing feed rate led to higher tensile *HSRS*. With regard to 300M, increasing *D* was found to have the same influence as increasing *f*. Also, increasing either *f, V* or *D* was found to increase the maximum compressive hoop residual stress beneath the surface. Since different combinations of parameters generated similar surface residual stresses, cutting conditions leading to minimum and maximum *ASRS* and *HSRS* values were gathered in Table 6. In light of the results presented hereabove, this project will investigate the influence of *f, V* and *D* on both surface and in-depth axial and hoop residual stresses in hard turned 300M.

Table 6: Summary of cutting conditions generating minimum and maximum *ASRS* and *HSRS* values.

Ref.	Workpiece material	Workpiece hardness [HRC]	Tool material	f [mm/rev]	V [m/min]	D [mm]	min. ASRS [MPa]	max. ASRS [MPa]	min. HSRS [MPa]	max. HSRS [MPa]
[21]	4340	37	Cermet	0.075	300	0.5	127			
				0.2	200	0.5		381		
				0.15	300	0.5			-16	
				0.2	200	0.5				593
[22]	4340	37	Cermet	0.075/0.1	255/300	0.4	154			
				0.075	200	0.4		562		
				0.075	300	0.4			123	
				0.2	200	0.4				600
[1]	300M	50	CVD ceramic coated carbide	0.1	60	0.2	-		-54	
				0.1	200	0.2				269

2.4 Influence of Surface Integrity on the Fatigue Behavior of Hardened 300M

Umezawa et al. [29] reported that fatigue crack initiation in hard steels occurs at the surface in the low cycle fatigue (LCF) regime due to the formation of extrusions/intrusions during slip while it occurs inside the material in the high cycle fatigue (HCF) regime due to the presence of non-metallic inclusions. However, this is true if the surface condition is such that the surface is considered "smooth" and therefore, that there are no defects at the surface. In fact, Murakami [30] reported that the following factors should be considered when evaluating the fatigue behavior of machined specimens because the surface condition has a significant influence on fatigue strength:

(i) Machining-induced surface roughness;

(ii) Machining-induced residual stresses;

(iii) Work hardening or softening due to plastic deformation and

(iv) Microstructural changes due to plastic deformation.

Figure 8 shows stress(S)-life(N) curves for various stress ratios in unnotched (Kt = 1.0) hardened 300M steel specimens. Considering high cycle fatigue to be associated with low stress amplitudes, elastic deformations and fatigue lives roughly above 10^5 cycles [31] it is expected that testing conditions involving applied stresses well below the yield strength of the material will lead to fatigue crack initiation at interior non-metallic inclusions based on Umezawa's statement reported above.

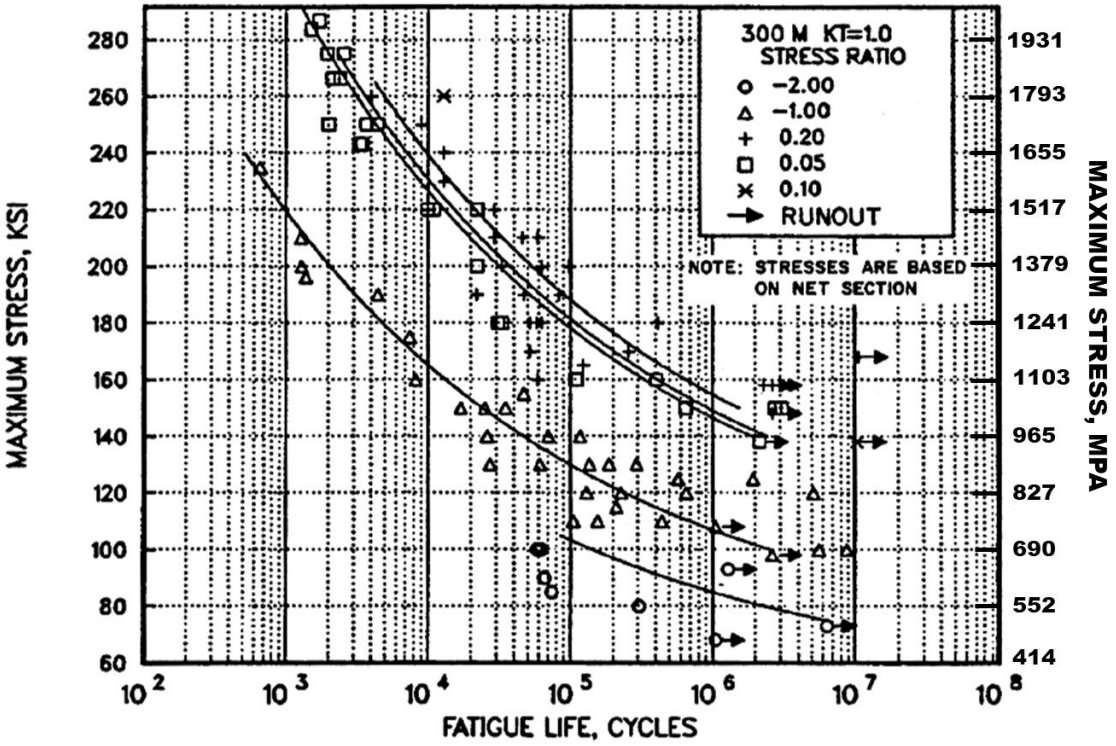

Figure 8: S/N curves corresponding to varying stress ratios under axial loading conditions for unnotched 300M hardened steel with an ultimate tensile strength of 1930 MPa (280 ksi) [32]

Although a large amount of studies has been published on fatigue properties of high strength steels in the very high cycle fatigue regime (VHCF, > 10^7 cycles), there are only a few studies focusing on the high cycle fatigue (HCF) regime. Numerous studies reporting on the VHCF range demonstrate that in high strength steels, failures initiate from interior non-metallic inclusions [33-35]. Therefore, considering that failures in the LCF regime, where applied stresses exceed the yield strength, are expected to result from surface crack initiations, the HCF domain becomes of significant importance because it lies between the LCF and VHCF regimes where a transition in crack initiation mechanism occurs.

There is practically no literature available both on fatigue properties of 300M hardened steel and the influence of surface characteristics generated by machining on its fatigue behavior. Therefore, since this project is concerned with the HCF behavior of hard turned 300M steel, the following section will first present results published on the fatigue behavior of machined 4340 hardened steel. Then, it will present results available on the influence of surface characteristics generated by other surface treatments such as shot peening on the fatigue behavior of hardened 300M steel.

2.4.1 Effect of Surface Characteristics on Fatigue Properties of 4340 and 300M Hardened Steels

The influence of machining on the fatigue behavior of 52-54 HRC 4340 steel has been studied by Matsumoto et al. [36] and Buddy Damm [37].

Matsumoto et al. [36] investigated the influence of fly cutting in two cutting directions as well as grinding on fatigue strength. Finishing fly cutting operations were performed using a feed rate, cutting speed and depth of cut of respectively 0.06 mm/rev, 108 m/min and 0.11 mm and generated a surface roughness *Ra* of 0.2 µm in both cutting directions. Finish grinding was performed using a wheel speed of 2350 rpm, a table speed of 10.15 m/min, a feed of 1.27 mm/pass and a depth of cut of 0.004 mm. Grinding generated an average surface roughness *Ra* of 0.2 µm which is comparable to fly cutting. However, both processes generated completely different surface roughness profiles as shown in Figure 9. Figure 10 shows residual stress profiles measured in the axial and hoop directions for all three specimens tested. The different cutting processes generated different profile shapes and the maximum compressive stress was found below the surface for fly cutting while it was found at the surface for grinding. Also, the most compressive residual stresses were generated by fly cutting in the direction perpendicular to the length of the specimen both for axial and hoop residual stresses.

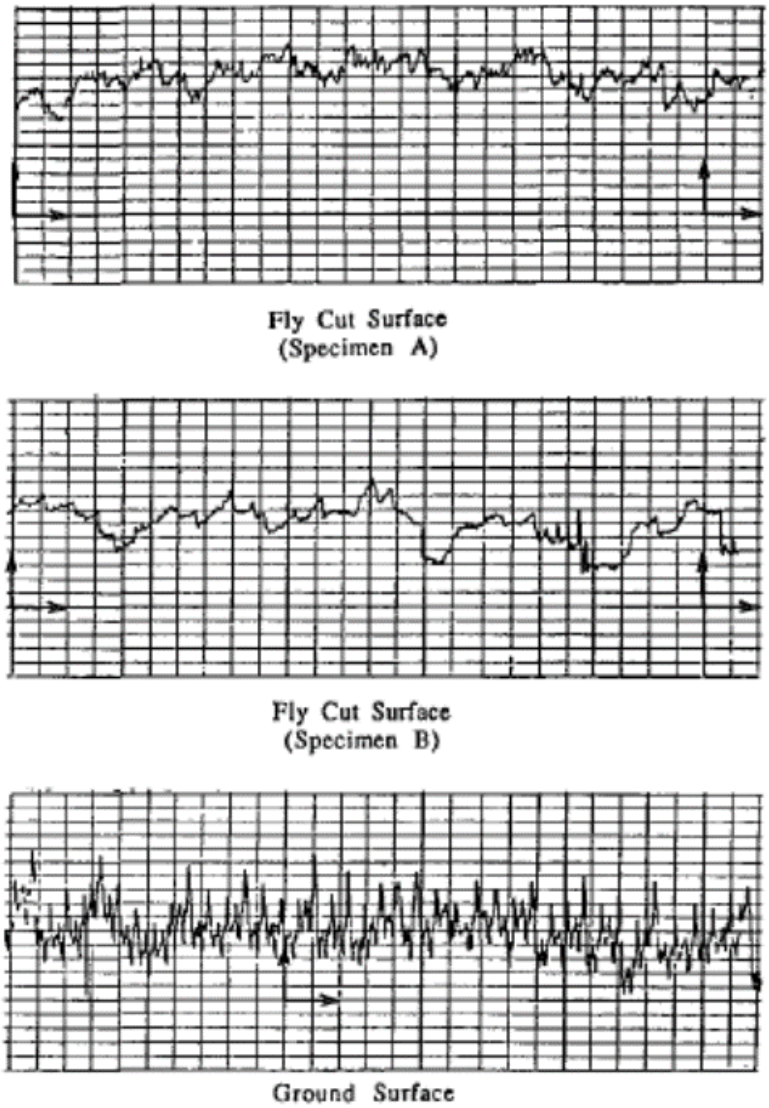

Figure 9: Surface roughness profiles generated by fly cutting and grinding on 52 HRC 4340. Figure copied from Matsumoto et al. [36] where specimen A corresponds to fly cutting with the feed in the perpendicular direction to the length of the specimen while specimen B corresponds to fly cutting with the feed in the direction parallel to the length of the specimen. X and Y axis are assumed to be one the same scale for each case illustrated.

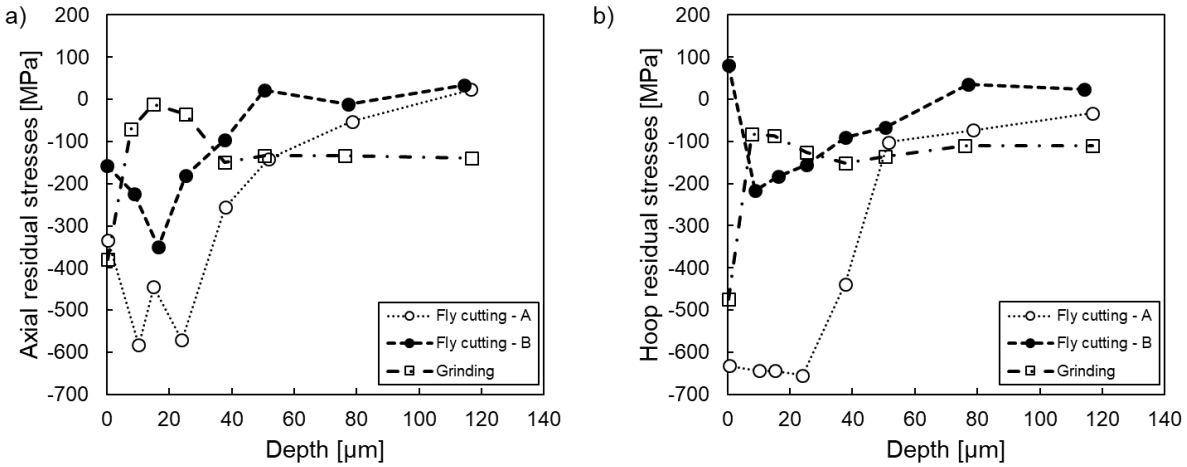

Figure 10: Axial (a) and hoop (b) residual stress profiles for specimens machined with fly cutting using a feed perpendicular (A) and parallel (B) to the length of the specimen as well as grinding based on data from Matsumoto et al. [36]. Dashed lines were only used to connect points, they do not represent a fit.

Figure 11 shows S/N curves for specimens machined under both fly cutting and grinding. Fly cutting generated surfaces leading to higher fatigue strength when compared to grinding. This was attributed in part to the greater depth of compressive residual stresses and in another part, to the lower maximum height of the profile roughness parameter *Rz*. In fact, although all three sets of specimens generated the same average *Ra*, they generated different *Rz* values; 0.91 μm for ground specimens, 0.64 μm for specimens fly cut in the direction perpendicular to the length of the specimens (A) and 0.76 μm for the specimens fly cut in the direction parallel to the length of the specimens (B). Additionally, Figure 11 shows that at higher applied stress values (≈ 910 MPa), ground surfaces generated similar fatigue lives when compared to fly cut specimens B but this result was not discussed by the authors.

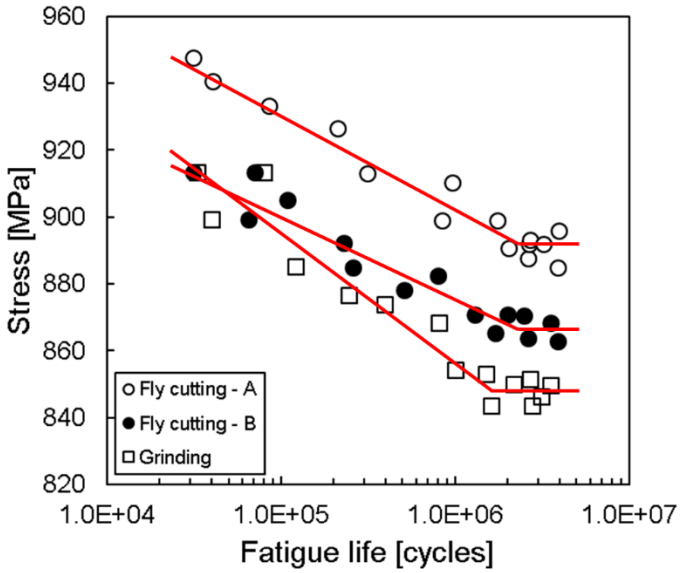

Figure 11:S/N curves for specimens machined using fly cutting in two directions and grinding based on Matsumoto et al. [36]. Fatigue testing performed under axial loading conditions at $R = 0.1$.

Buddy Damm [37] investigated the influence of steel cleanliness and surface characteristics generated by grinding on the fatigue strength of 52 HRC 4340 steel. Specimens were grinded to three different surface finish: fine ($Ra = 0.10 \pm 0.11$ µm), medium ($Ra = 0.25 \pm 0.09$ µm) and rough ($Ra = 0.77 \pm 0.10$ µm). Further, the author stated that all conditions evaluated generated similar residual stress profiles and thus, only the average residual stress profile was reported as shown in

Figure 12. The average maximum compressive (-480 MPa) stress was found at the surface in agreement with results from Matsumoto et al. [36] for grinding. However, since all conditions generated the same residual stress profile, residual stresses cannot explain the variations observed in fatigue strength. It is rather steel cleanliness and surface finish which can explain those variations. The fatigue strength of VIM/VAR specimens at 10^7 cycles was found to be 139 ksi (958 MPa) for the fine surface finish in comparison with 120 ksi (827 MPa) for the rough surface finish. Similarly, the fatigue strength of strand casted specimens at 10^7 cycles was found to be 120 ksi (827 MPa) for the fine surface finish in comparison with 99 ksi (683 MPa) for the rough surface finish. However, considering that crack initiation in strand specimens with fatigue lives of 10^7 cycles occurred at internal inclusions, it cannot be concluded on the relation between surface finish and fatigue strength in this case.

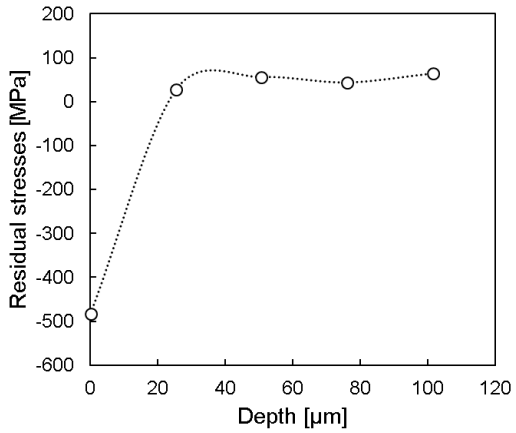

Figure 12: Average residual stress profile for varying steel cleanliness and surface finish based on Buddy Damm [37] (maximum standard deviation = ± 70 MPa).

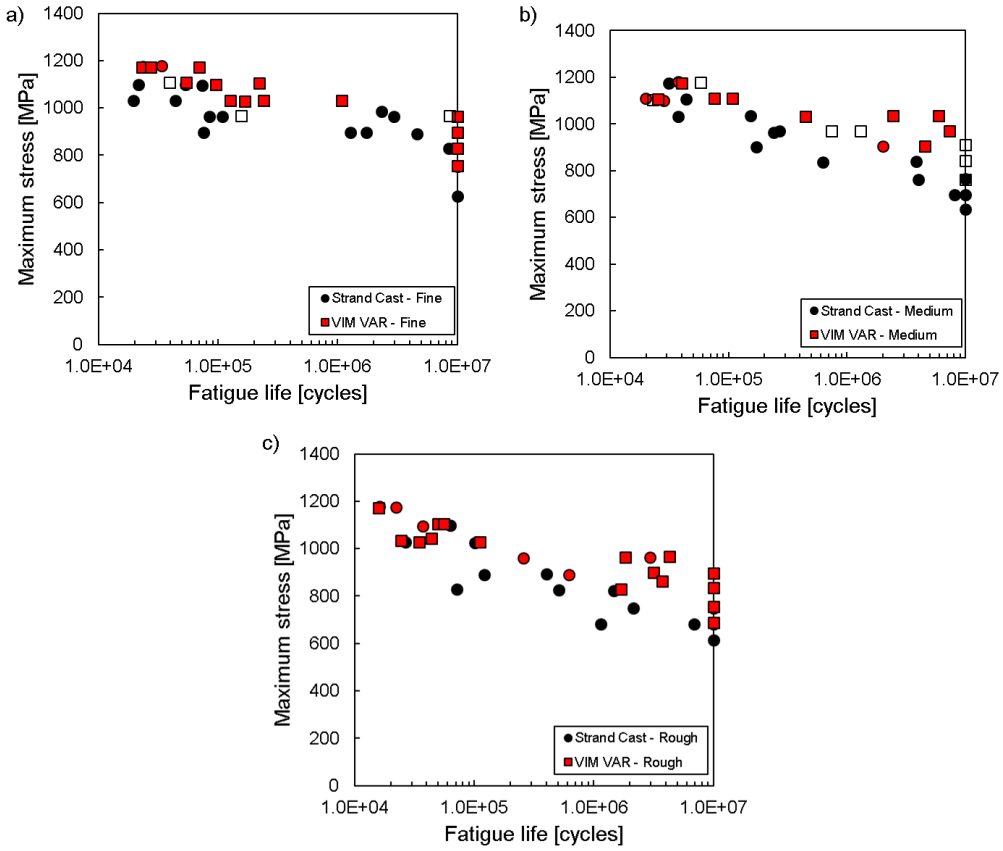

Figure 13: S/N curves for varying steel cleanliness and surface finish based on Buddy Damm [37]. Fatigue tests performed under rotating bending loading conditions. Red markers represent surface crack initiations while black and white markers represent crack initiations at inclusions.

As shown in Figure 13 and summarized in Table 7, failures in the cleaner steel (VIM/VAR) were mostly caused by surface initiations whereas failures in the strand casted steel were mostly due to

initiations from inclusions. The same amount of run-outs were reported in both cases. Further, higher fatigue strengths were obtained for specimens with lower inclusion content. Therefore, under rotating bending loading conditions, surface initiations were found to lead to higher fatigue strengths at 10 million cycles. Lastly as shown in Table 7, the ratio of surface failures/inclusion failures in the cleaner steel varied from 10/13 to 4/7 to 12/12 for the fine, medium and rough surface finish respectively. Therefore, according on those results, a fine surface finish generated more surface-based failures and less inclusion-based failures than a medium surface finish. This unexpected behavior was not explained and creates doubt to whether results for fine and medium finish in the cleaner steel were not inverted.

Table 7: Summary of fractographic results published by Buddy Damm [37] as function of melt practice and surface finish.

Melt Practice	Surface finish condition	Failure initiation site			Run-outs
		Surface	Inclusion	Unknown	
VIM/VAR	Fine	10	3	0	4
	Medium	4	7	2	3
	Rough	12	0	0	4
Strand Cast	Fine	1	14	1	3
	Medium	4	10	1	3
	Rough	5	11	0	3

Dickinson [5] published the only study available in the open literature reporting on the effect of machining on the fatigue behavior of 300M. However, this study did not report on the effect of surface characteristics generated by machining on the fatigue behavior of the material. Rather, it compared the HCF behavior ($R = 0$) of 56-58 HRC 300M steel specimens machined using different processes. Results showed that under unpublished optimum cutting conditions, turned specimens generated a higher fatigue strength at a million cycles when compared to milled specimens (σ_{max}: 993 vs 827 MPa). Results also showed that ground specimens performed better than turned specimens (σ_{max}: 1007 vs 993MPa at 10^6 cycles). Lastly, the author report that a comparison made between ground specimens that were subjected or not to a stress relief treatment, showed that machining-induced residual stresses were beneficial for fatigue life. However, no data demonstrating this statement was published.

A few studies have investigated the influence of surface characteristics generated by other surface treatments, namely shot peening [4] and laser peening [7]on the fatigue behavior of 300M steel.

Bag et al. [4] studied the influence of shot peening on the HCF life of 54 HRC 300M steel under axial loading conditions, a stress ratio R = -1 and a stress amplitude of 931 MPa. They characterized polished, as-machined and shot peened specimens and compared their fatigue lives. Surface roughness *Ra* was measured for all conditions and found to be 0.31 µm for as-machined specimens and ranged between 0.75 and 1.44 µm for shot peened specimens. Axial residual stress profiles were also measured for each condition evaluated as shown in Figure 14. A few observations can be made regarding those profiles. First, all processes generated compressive surface residual stresses including polishing. Second, the maximum compressive residual stress was located at the surface in polished specimens, at 9 µm in as-machined specimens and around 30 µm in shot peened specimens. Third, shot peened surfaces were characterized with significantly high compressive residual stresses in comparison with as-machined and polished surfaces. Last, the depth of the layer affected by shot peening residual stresses was found to be significantly larger than the ones of as-machined and polished specimens.

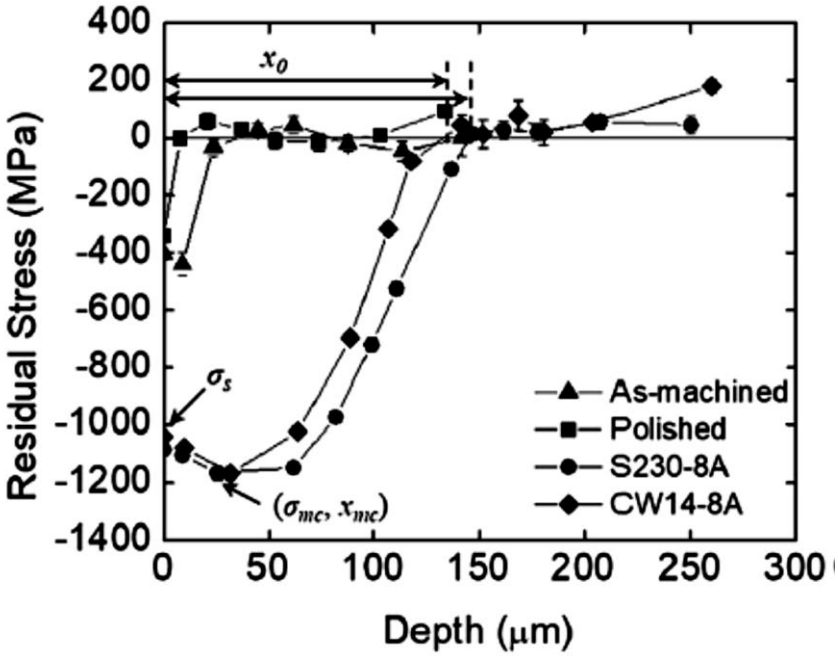

Figure 14: Axial residual stress profiles for varying tested surface conditions. Copied from Bag et al. [4].

Surprisingly, although very different surface conditions were tested, fatigue results presented in Figure 15 demonstrate that similar fatigue lives were obtained for polished, as-machined and peened specimens showing that surface condition does not have a significant influence on fatigue life for specimens tested under axial fatigue loading conditions. This can be attributed to the fact that overall, most failures initiated from subsurface inclusions, independently from the surface condition, implying that interior defects are characterized with a larger stress intensity factor in comparison with surface defects. The scatter obtained in fatigue life was attributed by the authors to the inclusion sizes. This is consistent with an earlier statement from Murakami et al. [38] on high strength steels who reported that there is a relationship between the size of the non-metallic inclusion from which a fatigue crack initiated in a specimen and its fatigue strength.

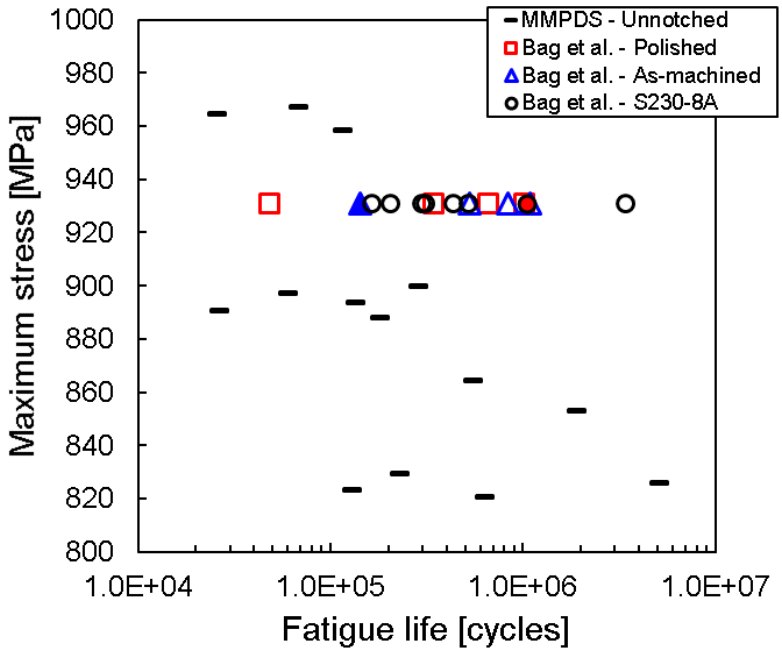

Figure 15: Fatigue life for 54 HRC 300M steel tested under axial loading conditions at R = -1 based on data from [32] and [4]. For data extracted from Bag et al.[4], empty symbols refer to inclusion initiations while full symbols refer to surface initiations. The comparison with data from the MMPDS handbook shows that for the same testing conditions and similar stress amplitudes, Bag et al. [4] reported greater fatigue lives for unnotched specimens.

Pistochini et al. [7] investigated the influence of laser peening on the fatigue behavior of 54 HRC 300M steel. They tested specimens in the as-machined, shot peened and laser peened conditions in a four-point bending fatigue setup at R = 0.1. The axial residual stress profile for the shot peened condition is presented in Figure 16 and compared to the one obtained under the same shot peening

conditions investigated by Bag et al. [4] showing consistency between the profiles. The corresponding fatigue data is presented in Figure 17 and compared with other data sets. Both as-machined and shot peened specimens where tested at stress amplitudes below the material's yield strength (1654 MPa). Results demonstrate a significant improvement in fatigue strength at a million cycle when comparing as-machined and peened specimens. The difference between these results and the ones published by Bag et al. [4] can be explained by the different loading type (four-point bending vs. axial), stress amplitude (1220-1550 vs. 931 MPa) and stress ratio *R* (0.1 vs. -1).

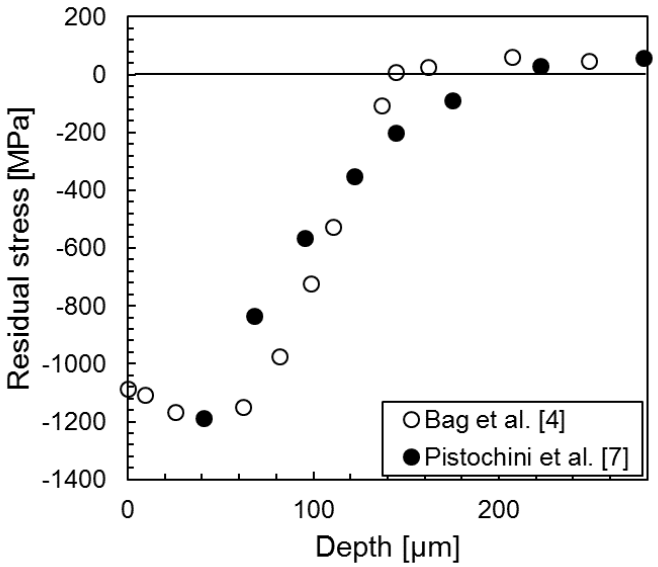

Figure 16: Residual stresses generated by shot peening under identical conditions (based on data from Bag et al. [4] and Pistochini et al. [7]).

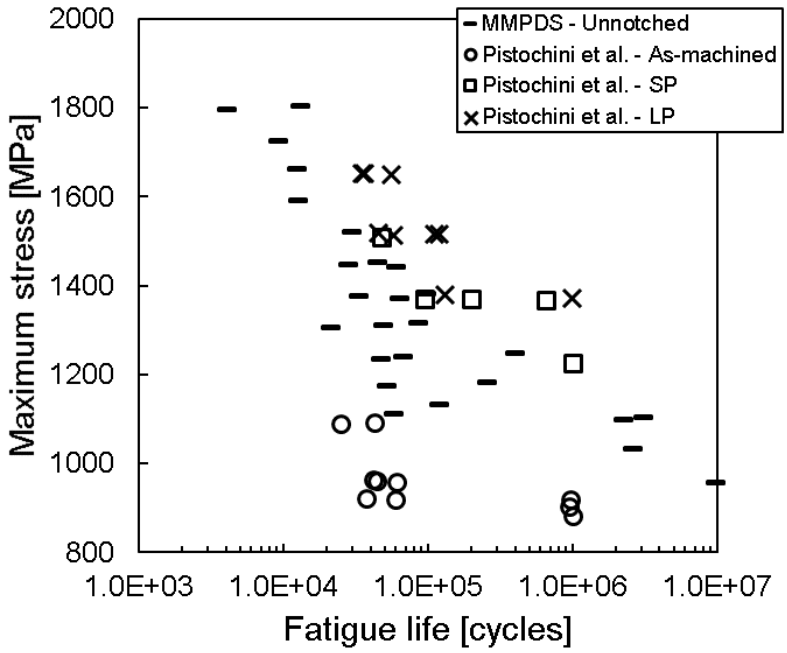

Figure 17: Stress-life data extracted from [7, 32] for hardened 300M steel. Fatigue tests carried out under axial (unnotched specimens only) and four-point bending fatigue conditions at R = 0.1. Surface conditions tested include unnotched [32], as-machined, shot peened and laser peened [7].

In summary, this section demonstrated that the following characteristics can have an influence on the fatigue behavior of hardened 4340 and 300M steels: surface finish (roughness parameters and profile), surface residual stresses, residual stress profiles (including the amplitude of the maximum compressive residual stress and its position), steel cleanliness (inclusion content) and inclusion characteristics (size and position). Considering the possible interactions between all those characteristics and the limited amount of data available in the open literature, it is not possible to draw conclusions from this limited review. Therefore, this research project will investigate both the influence of hard turned surface characteristics and crack initiation mechanism on the HCF behavior of 55 HRC 300M steel.

2.5 Optimization of Hard Turned Components Surface Characteristics

The optimization of hard turning cutting parameters is necessary to generate desired surface integrity characteristics. However, considering the number of variables that may influence the machining process, it can become a complex and time-consuming task. Therefore, the selection of

an optimization technique should respond to the following industrial criteria: simple to use, cost-friendly, accurate optimum and time-effective.

Campos et al. [39] reviewed the main optimization and modeling techniques used in hard turning studies and reported six approaches: (i) Taguchi method and ANOVA, (ii) response surface methodology (RSM), (iii) genetic algorithm (GA), (iv) artificial neural network (ANN), (v) adaptive neuro-fuzzy inference system (ANFIS) and (vi) finite element method (FEM). Those methods have been typically used to minimize surface roughness or tool wear. In particular, methods (i) and (ii) have commonly been used to minimize *Ra* in hard turned 4340 steel [19, 25-27]. However, although either single-objective techniques can be used to solve hard turning optimization problems, the use of a multi-objective technique is the most appropriate approach because the process involves multiple parameters and influences several surface characteristics at a time. Therefore, the multi-objective technique generates a unique optimum which takes into account the influence of several parameters on multiple responses whereas the single-objective method generates an optimum which takes into account the influence of several parameters on one response only.

Because the Taguchi method allows both to design for a minimum sensitivity of controllable factors to process variation [40] and to minimize the number of experiments required using orthogonal arrays (type of DOE) [39], it was combined with the Grey relational analysis (GRA) to solve multi-objective problematics in turning studies [41-43]. Further, it was augmented with the principal component analysis by Rajesh et al. [42] to account for the possible interactions between the parameters evaluated. Therefore, the combination of Taguchi-GRA-PCA is believed to be a suitable choice for optimizing hard turning for the industry because it is simple, requires a minimum of tests only (Taguchi), doesn't require to the use of a costly software (calculations can be done using Excel), generates results rapidly, and has proven itself effective in generating accurate results, in part because it evaluates multiple responses simultaneously (GRA) and in part because it takes into account the existence of correlations between cutting parameters (PCA). For all those reasons, this methodology will be used for the multi-objective optimization of hard turning cutting parameters to generate desired surface characteristics in hardened 300M steel which is a topic that has not been addressed yet in the open literature. The following section will describe in details the approach to be used.

2.5.1 Taguchi-GRA-PCA Multi-Objective Optimization Approach

The combination of the Taguchi and GRA methodologies allows one to evaluate multiple process parameters and optimize several responses simultaneously. The Taguchi method involves the use of the signal-to-noise (η) objective function which has three different forms depending on whether the response studied is to be minimized, maximized or converged towards a nominal value [44]:

Maximum is the best
$$\eta_{ij} = -10 \log \left[\frac{1}{p} \sum_{k=1}^{p} \frac{1}{y_{ijk}^2} \right] \quad \text{Equation (1)}$$

Minimum is the best
$$\eta_{ij} = -10 \log \left[\frac{1}{p} \sum_{k=1}^{p} y_{ijk}^2 \right] \quad \text{Equation (2)}$$

Nominal is the best
$$\eta_{ij} = -10 \log \left[\frac{1}{p} \sum_{k=1}^{p} \left(y_{ijk} - y_i^* \right)^2 \right] \quad \text{Equation (3)}$$

where y_{ijk} is the value of the i^{th} surface characteristic of the k^{th} replicate from experiment j, p the total number of replicates and y_i^* the nominal value. Because the function is logarithmic, the greater is the value of η_{ij}, the smaller is the sensitivity of the response variable y_{ijk} to process variations.

The GRA method is a procedure evaluating multiple responses using one single coefficient named the grey relational grade (*GRG*). The first step involved in the procedure is the normalization of the data. The units of the different responses to be evaluated can vary and the range of evaluation can be very large for a response and very narrow for another one. Therefore, the normalization of the data generates dimensionless quantities which can be compared. In the same order, the following equations should be used when a response is maximized, minimized or converged towards a nominal value:

$$x_{ij} = \frac{\eta_{ij} - \min(\eta_{ij})}{\max(\eta_{ij}) - \min(\eta_{ij})} \quad \text{Equation (4)}$$

$$x_{ij} = \frac{\max(\eta_{ij}) - \eta_{ij}}{\max(\eta_{ij}) - \min(\eta_{ij})} \quad \text{Equation (5)}$$

$$x_{ij} = 1 - \frac{\left| \eta_{ij} - \eta_i^* \right|}{\max\left[\left(\max(\eta_{ij}) - \eta_i^* \right), \left(\eta_i^* - \min(\eta_{ij}) \right) \right]} \quad \text{Equation (6)}$$

where $i = 1, \dots, m, j = 1, \dots, n$ and x_{ij} and η_{ij} represent respectively the comparative and original (signal-to-noise ratios) sequences. Normalized values range between 0 and 1 and represent respectively a poor and a good performance.

The following step involves the calculation of the Grey relational coefficients (*GRCs*). It requires a reference sequence which represents an ideal performance and thus, contains values equal to one. The purpose of the *GRC* is to determine how close the comparability and reference sequences are from one another and is calculated using the following equation:

$$\gamma(x_{i0}, x_{ij}) = \frac{\Delta\min + \xi\Delta\max}{\Delta_{ij} + \xi\Delta\max} \qquad \text{Equation (7)}$$

where $x_{i0} = \{1, \dots, 1\}$, $\Delta_{ij} = \left|x_{i0} - x_{ij}\right|$, $\Delta_{min} = \min \Delta_{ij}$, $\Delta_{max} = \max \Delta_{ij}$ and $\xi \in [0,1]$. The distinguishing coefficient ξ is only used to expand or compress the range of the *GRC* and is set to 0.5 as suggested in [45].

The last next step in the procedure is the calculation of the Grey relational grades (*GRGs)*. The *GRG* is calculated using Equation (8) and represents the performance of an experiment based on all the responses evaluated. The highest GRG calculated corresponds to the set of cutting parameters leading to the best surface integrity.

$$\Gamma\left(x_{i0}, x_{ij}\right) = \sum_{i=1}^{m} w_i \cdot \gamma(x_{i0}, x_{ij}) \qquad \text{Equation (8)}$$

where w_i represents the weighting factor for the i^{th} response parameter with $\sum_{i=1}^{m} w_i = 1$. Here, the weighting factors are determined using the first principal component which contributes the most to the overall variance. The first principal component is calculated using the eigen vector corresponding to the highest eigen value determined from the correlation matrix and described using Equation (9).

$$\psi_{ir} = \sum_{i=1}^{m} x_{ir} \cdot V_{ir} \qquad \text{Equation (9)}$$

where $r = 1, \dots, m$ and V_{ir} represents the eigenvector. Then, using the first principal component ψ_{i1}, the weighting factors can be calculated using Equation (10).

$$w_i = \psi_{i1}^{\ 2} \qquad \text{Equation (10)}$$

2.6 Fatigue Life Modelling

The ability to model fatigue life leads to better engineering designs, avoiding the use of overly conservative fatigue life estimates and early withdrawal of in-service components. Therefore, modelling of fatigue life should aim to improve processes involved with the manufacturing of high performance components in order to not only predict the fatigue life of components for varying processing conditions, but to determine optimum processing conditions under which fatigue life is maximized.

2.6.1 Short Crack Growth Modelling

"Small crack" theories have been developed to model the fatigue-life of metallic materials. Some theories have attempted to model the propagation behavior of short cracks by modifying the LEFM theory to account for closure effects [46, 47]. However, those models have not considered the effect of microstructural features on the growth of such cracks. Thus, they are not appropriate for the scope of this study because the effect of turning finishing conditions on fatigue life is constrained in a depth with a size of the order of microstructural features. Other models taking into consideration the effect of microstructure, mainly the blocking effect of microstructural barriers, have been proposed in the literature. These models will be discussed further.

2.6.1.1 Chan and Lankford's Model

Chan and Lankford [48] proposed a model based on the strain at the crack tip which accounts for crystallographic anisotropy and grain boundaries barrier effects. If crack-tip slipping is restricted as the crack approaches a grain boundary, the propagation rate decreases. Assuming that the plastic range, measured by the crack-tip opening displacement, for a short crack is higher than that for a long one and that the crack tip plastic range follows a power law, they proposed the following relationship to calculate the plastic range:

$$\Delta\varepsilon_p = C\Delta K^n \left[1 - k(\Phi)\left(\frac{D - 2\mathrm{X}}{D}\right)^m\right] \quad \text{Equation (11)}$$

where $\Delta\varepsilon_p$ represents the plastic range, C a constant of integration, ΔK the stress intensity factor, $k(\Phi)$ a function depending on the crystallographic orientation of the neighbouring grain, D the average grain diameter, X the distance from the crack tip to the nearest grain boundary and where m and n represent fitting power constants. The crystallographic function $k(\Phi)$ can be formulated in terms of resolved shear stresses required for slip activation in a grain A containing the crack and a neighbouring grain B:

$$k(\Phi) = 1 - \frac{\tau_B}{\tau_A} \quad \text{Equation (12)}$$

leading to:

$$\Delta\varepsilon_p = C\Delta K^n \left[1 - \left(1 - \frac{\tau_B}{\tau_A}\right)\left(\frac{D - 2\mathrm{X}}{D}\right)^m\right] \quad \text{Equation (13)}$$

If $\tau_B/\tau_A > 1$, that is if $\tau_B > \tau_A$, $\Delta\varepsilon_p$ will increase as the crack approaches a grain boundary and vice-versa. Considering that crack advance occurs through the failure of a crack tip element when the cumulated plastic deformation strain exceeds a critical plastic value ε_p^*, the number of cycles leading to the failure of the crack tip element is represented by:

$$\Delta N = \frac{\varepsilon_p^*}{\Delta\varepsilon_p} \quad \text{Equation (14)}$$

and the resulting propagation rate is:

$$\frac{da}{dN} = C\frac{\Delta\mathrm{X}'}{\varepsilon_p^*}\left[1 - \left(1 - \frac{\tau_B}{\tau_A}\right)\left(\frac{D - 2\mathrm{X}}{D}\right)^m\right] \quad \text{Equation (15)}$$

where $\Delta\mathrm{X}'$ represents the size of the crack tip element.

2.6.1.2 Hobson's model

Hobson [49] proposed an empirical model combining two equations: (i) one representing the growth of a short crack which takes into consideration the grain boundary effect and (ii) another

one describing the crack growth behavior until failure which is based on the LEFM theory. The general equation used to represent the short crack growth is as follows:

$$\frac{da}{dN} = C_1(d-a)^{1-x}a^x \qquad \text{Equation (16)}$$

where $(d-a)$ represents the remaining slip band plastic zone and a the crack length and where C_1 and x are fitting parameters. When the crack has reached the grain boundary diameter, that is when $d = a$, the crack growth rate $\frac{da}{dN}$ is null. Cracks with length greater than one grain diameter size are modelled according to the following relationship:

$$\frac{da}{dN} = C_2[\Delta K^m - \Delta K_{th}^m] \qquad \text{Equation (17)}$$

where C_2 and m are fitting parameters determined using data points near the threshold only. The model was found to predict the behavior of a crack from initiation to failure according to the experimental data. However, this approach confines the short crack behavior to one single grain which is not representative of all materials for which this behavior can extend to a few grain diameters in size.

2.6.1.3 Navarro-Rios Model

Navarro and de Los Rios developed their model based on Bilby's theory. They implemented the concept of the microstructural barrier for a crack growing along a slip band [50]. They represented a crack as a system consisting of three distinct regions: (i) the crack itself, (ii) the plastic zone and (iii) the barrier zone [51] as shown on Figure 18 where a represents the position of the crack tip on the x axis, D the grain diameter, i the number of half grains and r_0 the size of the barrier. The second axis represented by ξ is a dimensionless axis representing the plastic zone size. Here, $\eta_i = a/c_i$ where $c_i = \frac{iD}{2} + r_0$ and represents the size of the half crack, plastic zone and barrier.

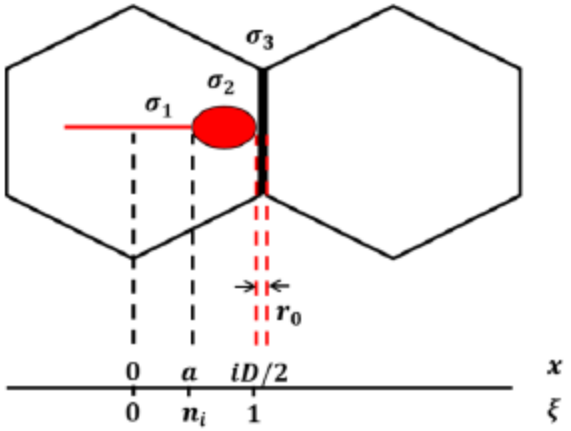

Figure 18: Basic illustration of the N-R model.

In each of the zones described, there is a back stress reacting to the applied load [52]. In the crack zone, the only resistance stress can be a closure stress σ_1 acting on the crack flanks which can result either from the stress field of other dislocations or the effect of solute atoms and precipitates. In the plastic zone, the back stress σ_2 is the resistance to plastic deformation and corresponds to the cyclic yield stress ${\sigma_{YS}}^c$ of the material and in the barrier zone, it corresponds to the barrier strength σ_3, for instance, the grain boundary strength σ_{GB}. In order for the crack to propagate to the next grain, it has to be able to overcome the stress at the microstructural barrier which corresponds to the condition for crack arrest [53]:

$$\sigma_{arrest} = \frac{m_i}{m_1}\frac{\sigma_{FL} - \sigma_1}{\sqrt{i}} + \sigma_1 \qquad \text{Equation (18)}$$

Here, σ_{FL} corresponds to the fatigue limit of the material, σ_1 is the closure stress, i the number of half grains affected by the ongoing fatigue process, $m_1$is the orientation factor in the first grain and m_i the grain orientation factor in the subsequent grains which accounts for the crystallographic misfit between the neighbouring grains [52]. If the applied stress is greater than σ_{arrest}, plastic slip will transfer to the second grain, the plastic zone will cover the entire new grain and the crack will grow. Similarly, these steps will be repeated for each subsequent grain [54].

Considering the crack propagation rate to be proportional to the crack tip opening displacement ($CTOD$), de Los Rios and Navarro proposed a Paris-type relationship for the crack growth where

$CTOD$ is function of the variables described here above, and where A_2 and m_2 are material constants.

$$CTOD = f(\sigma_1, \sigma_2, \sigma_3, \eta_i, \xi_i) \quad \text{Equation (19)}$$

$$\frac{da}{dN} = A_2(CTOD)^{m_2} \quad \text{Equation (20)}$$

2.6.2 The N-R Model Applied to the Case of Machined Components

To the best of the author's knowledge, Kuroda et al. [55] are the only one who used the N-R model to model the fatigue life of machined specimens. They considered the effect of surface finish by adding a notch factor to the crack arrest condition and the effect of residual stresses by combining the residual stresses resulting from machining with the closure stress σ_1.

Since a roughness profile resulting from machining consists of a sequence of micro-notches rather than a single notch, the authors used a notch factor Z_i function of the mean distance between microstructural barriers (D), the half-width of the notch (β) and the depth of the notch (α). Together, the effects of surface roughness and residual stresses were implemented to express the condition for crack arrest as follows:

$$\sigma_{arrest} = Z_i \left[\frac{m_i}{m_1}\frac{\sigma_{FL} - \sigma_1}{\sqrt{i}} + \sigma_1\right] \quad \text{Equation (21)}$$

The authors reported a discrepancy between the experimental data and the fatigue life predictions using the N-R model. They suggested that the actual form of the model was not suitable for austenitic stainless steels because the model assumes that grain boundaries are the most significant barriers and that closure stresses are not relaxed which might not be the case for the material studied.

2.7 Summary of the Literature

This review shows the limitations of the available data regarding both the influence of hard turning on the surface integrity of 300M and the influence of surface integrity on the fatigue performance of the material. The following conclusions summarize the key elements highlighted by this review:

- For constant tool material, feed rate is the parameter with the greatest contribution to surface roughness.
- The influence of a cutting parameter on surface roughness and residual stresses is dependent on the influence of other cutting parameters and magnitude.
- Significantly different combinations of cutting parameters can lead to similar surface integrity characteristics.
- The hybrid Taguchi-GRA-PCA method is a suitable optimization approach for hard turning.
- Under HCF and VHCF regimes, crack initiation in high strength steels was found to be mostly inclusion-based. However this conclusion is valid for the conditions published only.
- The relationship between surface characteristics and fatigue life can be described by a model of the type Navarro-Rios.

2.8 Problem Definition

The number of studies reporting on the influence of turning on the surface integrity and on the influence of surface integrity on the fatigue behavior of 300M ultra-high strength steel is limited. The constrained range of turning cutting parameters studied and the wide combinations of parameters tested makes it impossible to select a set of parameters that will allow generating desired surface integrity characteristics based on the published literature. Also, the few studies reporting on the fatigue behavior of machined 300M steel, either compare the effect of machining processes on fatigue performance using unpublished cutting conditions or use as-machined specimens as a comparison base for laser- and shot- peened specimens. Therefore, two questions arise:

1. How can we optimize finish turning cutting parameters to generate the best surface integrity characteristics in terms of fatigue performance?
2. How do surface characteristics influence the fatigue behavior of finish hard turned 300M ultra-high strength steel?

2.9 Objectives

This thesis has two main objectives which are derived from the problem definition:

1. Determine the set of hard turning cutting parameters leading to the best surface integrity in terms of fatigue performance. To produce 300M components with optimized fatigue life, surface integrity characteristics will be optimized. This will be achieved by (i) determining the most suitable optimization approach for the case studied and by (ii) measuring mainly surface roughness and residual stresses. The following two questions will be answered:
    - What is the influence of finishing hard turning conditions on the surface integrity of hardened 300M?
    - What finish hard turning cutting conditions are the most effective in minimizing simultaneously surface roughness and tensile residual stresses?
2. Study the influence of surface characteristics on the fatigue behavior of finish hard turned 300M. The following relationships will be studied:
    - Surface integrity characteristics and rotating bending high cycle fatigue life.
    - Crack initiation types, maximum stress intensity factor and high cycle fatigue life.

CHAPTER 3 METHODOLOGY AND ORGANIZATION

This section provides a detailed experimental methodology developed to (i) determine the set of hard turning cutting parameters leading to the best surface integrity in terms of fatigue performance and to (ii) study the influence of surface characteristics on the fatigue behavior of finish hard turned 300M. It is followed by a presentation of two articles written and published to respond to those two objectives.

3.1 Experimental Methodology

The microstructure and mechanical properties of the material were characterized to ensure the material's conformity with AMS6257E. All specimens used were extracted from the material in the bar form.

3.1.1 Material Characterization

The chemical composition of the material was measured via spark atomic emission spectrometry according to ASTM E415-14 to ensure it meets the requirements from AMS6257E. Because materials properties depend on grain size, the material was etched to verify that the average prior-austenite grain diameter is no greater than ASTM 6 as per AMS6257E. To do so, a polished specimen was etched using a solution heated to 80-90 °C consisting of a mixture of water saturated with picric acid, HCl (1 mL in 500 mL of water) and 15 mL of wetting agent. The average grain size was measured according to the intercept procedure described in ASTM E112.

A specimen was cut in the transverse direction using an Acuttom precision cutter, grinded starting at 120 grits and polished to 0.05 μm using a Tegramin automatic system. The specimen was polished carefully to ensure its surface was flat and strain-free and etched using a 2% Nital solution. The martensitic structure of the quenched and tempered material was revealed using an electron channeling contrast imaging technique (ECCI) under a voltage of 10 kV. This technique involves the use of backscattered electrons in a scanning electron microscope.

Another specimen was prepared using the method described above to ensure the inclusion content lied within the limits prescribed by AMS6257E. The inclusion count was performed according to the method D described in ASTM E45 for steels with low inclusion content. Results revealed the

presence of MnS inclusions (Type A) with length below the maximum value of 261 µm reported in Table 3 (see section 2.1) as shown in Figure 19.

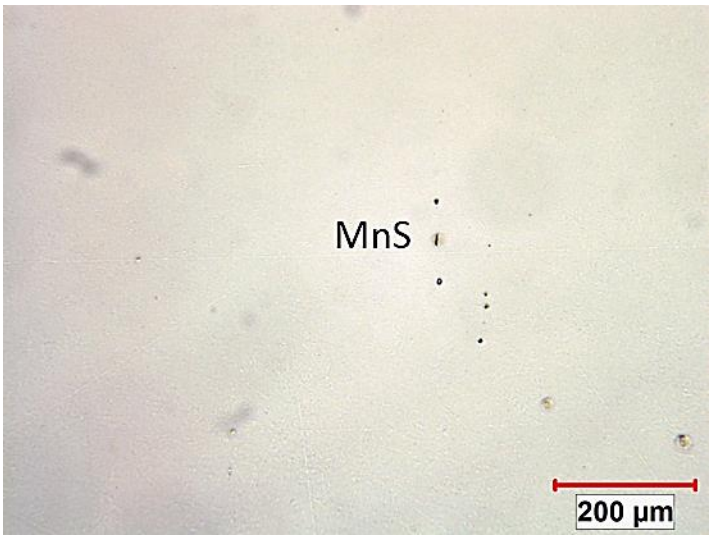

Figure 19: MnS inclusions observed in 55 HRC 300M steel produced by vacuum arc remelting.

3.1.2 Mechanical Properties

Tensile properties were evaluated to ensure the batch of material used meets the minimum requirements prescribed by AMS6257E. Four specimens with the geometry and dimensions presented in Figure 20 were tested according to ASTM E8-8M. Specimens were tested at a strain rate of 0.015 ± 0.006 mm/mm/min and deformation was measured using an extensometer. The following properties were measured in the longitudinal direction: ultimate tensile strength (UTS), 0.2% yield strength (YS) and elongation (%).

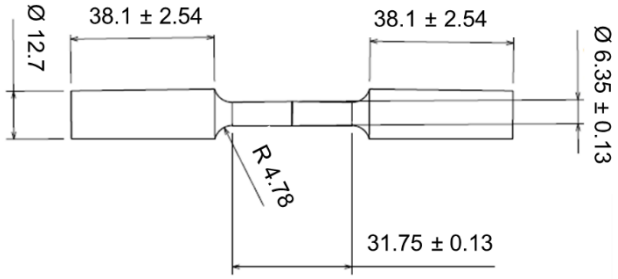

Figure 20: Tensile test specimen. Dimensions are given in millimeters.

3.1.3 Machining Tests

Two sets of machining tests were performed to respond to objectives (i) and (ii) presented at the beginning of this section. First, nine cutting conditions were evaluated according to a Taguchi L9 design of experiment (DOE) as shown in Table 8.

Table 8: Hard turning cutting parameters. First set of machining tests. *T*, *V*, *f* and *D* represent respectively the tool material, cutting speed, feed rate and depth of cut.

Cutting condition	Control factors			
		[m/min]	[mm/rev]	[mm]
1	Carbide	50	0.051	0.254
2	Carbide	75	0.127	0.508
3	Carbide	100	0.203	0.762
4	Ceramic	50	0.127	0.762
5	Ceramic	75	0.203	0.254
6	Ceramic	100	0.051	0.508
7	PCBN	50	0.203	0.508
8	PCBN	75	0.051	0.762
9	PCBN	100	0.127	0.254

Four specimens per cutting condition were machined to the geometry and dimensions presented in Figure 21. Vibration occurred during several machining tests and was attributed to the material's hardness, small specimens' size and machine capability. This resulted in the loss of several specimens and thus, the setup was optimized to make it stiffer and eliminate vibration during the machining of other specimens. However, although 36 specimens were machined successfully, fatigue tests could not be completed because slipping occurred at the collets due to fretting at the interface between the specimen's grips and the collets used to fix specimens in the fatigue testing machine. Since this set of machined specimens only allowed us to respond to objective (i), a second set of specimens had to be machined with the limited amount of material remaining.

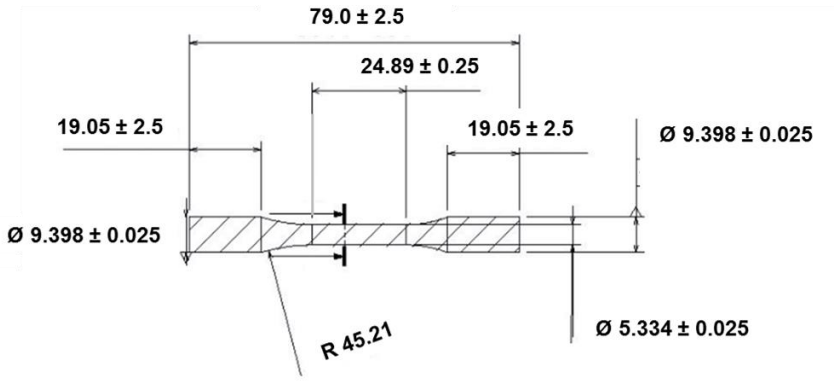

Figure 21 : Fatigue test specimens – first design. Dimensions are in millimeters.

To prepare this second set of machining tests, the following elements have been considered:

- The specimens' size could cannot be increased because increasing the diameter would not allow testing specimens at the required stress level on the RR Moore fatigue testing machine;
- Specimens cannot be machined under high cutting speed and feed rate conditions due to a combination of material's hardness, specimen size and machine capability under such conditions;
- The design of fatigue test specimens has to me modified to integrate internal fillets in the specimens' ends, in order to eliminate the use of collets by fixing the specimens directly in the machine and allow fatigue testing to be carried until completion.

Cutting conditions selected for the second set of machining tests are presented in Table 9. The number of specimens machined for each condition is also reported on this table. As can been seen, the number of specimens is not equal for all conditions. A series of three specimens per condition was first machined according to the new design illustrated in Figure 22. The remaining quantity of material available only allowed to machine three more specimens. Either one new condition with three specimens was added to this plan, either three specimens were machined for a selected cutting condition to increase its statistical power. The second option was chosen, and three more specimens were machined for condition C4.

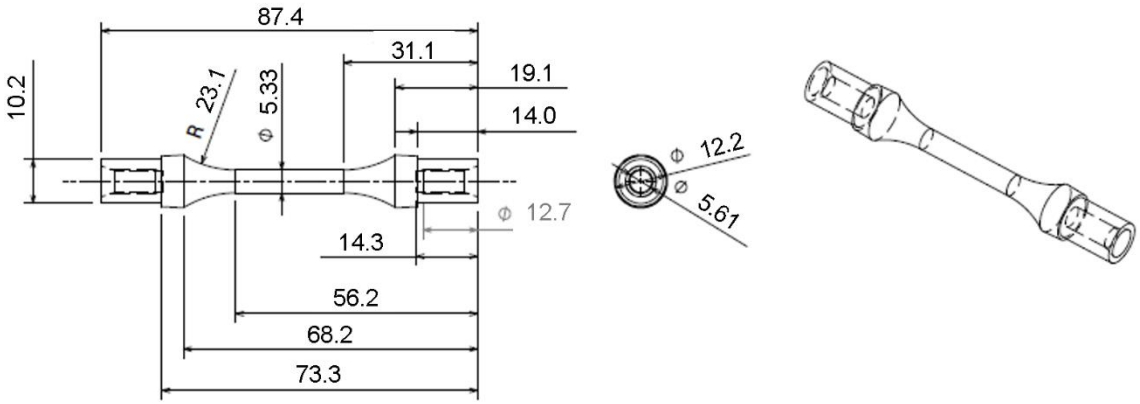

Figure 22: Fatigue test specimens – second design. Dimensions are in millimeters.

Table 9 : Hard turning cutting parameters. Second set of machining tests.

Cutting condition	Number of specimens	Cutting speed, *V* [m/min]	Feed rate, *f* [mm/rev]	Depth of Cut, *D* [mm]
C1	3	85	0.053	0.490
C2	3	55	0.152	0.245
C3	3	100	0.053	0.490
C4	5	69	0.053	0.319
Total number of specimens = 14				

3.1.4 Characterization of Fatigue Specimens

3.1.4.1 Residual stresses

Residual stresses were measured by x-ray diffraction which involves the measurement of strain resulting from the deformation of a crystal lattice. Measurements were performed using a µ-X360 portable X-ray residual stress analyzer with a Cr beam source and a 1 mm beam aperture. Residual stresses are calculated from the strain assuming an elastic distortion of the lattice [56]. Measurements were made according to the single angle technique also called the cos alpha method. Under this method, a 2D detector captures the cone of diffracted radiation formed when X-rays diffract from a surface [56]. The intersection area between the diffraction cone and the detector generates what is known as the Debyer-Scherrer ring [57]. The strain is obtained by the comparison of the distorted and perfectly circular rings representative of a stressed an unstressed specimen respectively.

Surface residual stresses were measured on all specimens and a total of three measurements per specimen were recorded. Residual stress profiles were measured on one specimen representative of each cutting conditions. To measure in-depth residual stresses, specimens were electropolished to uncover a new surface at various depths.

3.1.4.2 Surface finish

Surface roughness profiles and parameters were acquired on all specimens in the feed direction using a laser confocal microscope (non-contact method) and a cut-off of 0.8 mm corresponding to one sampling length (the total evaluation length equals 5 times the sampling length; 4 mm).

3.1.4.3 White layer thickness

One specimen per cutting condition was polished and etched with 2% Nital to reveal the presence of a white layer at the top of the machined surface. Ten measurements per specimen were taken on a length of 22 μm using images generated at 25 kV and 50 amps using a scanning electron microscope.

3.1.5 Fatigue Testing and Fractography

Rotating bending fatigue tests (R = -1) were performed on an RR Moore high-speed rotating beam fatigue at a rotation speed of 3300 rpm and stress amplitude σ_a of 965 MPa. Due to all the limitations reported in section 3.1.3, a total of 14 machined specimens have been tested only. The conditions under which tested specimens were machined are summarized in Table 9.

Fractographic images were taken on all specimens using both a laser microscope and an electron scanning microscope to determine the mechanisms under which cracks initiated in finish hard turned 55 HRC 300M steel.

Table 10 summarizes all the tests performed to obtain the data required to meet the objectives of the current research project.

Table 10: Tests summary table.

	Condition	Tests	Evaluation
Base material characterization	Raw material	Metallography	Microstructure Grain size Inclusion content
		Tensile testing	Yield strength Ultimate tensile strength Elongation
Surface integrity characterization	As-machined	Surface roughness	Surface profiles Surface roughness parameters
		Residual Stresses	Surface measurements In-depth profiles
		Metallography	White layer thickness
Fatigue testing	As-machined	Rotating bending testing	Stress ratio R = -1 σ_a = 965 MPa Rotation speed = 3300 rpm
Fractography	Fracture surfaces	Optical microscopy Scanning electron microscopy	Crack initiation site

3.2 Publication Strategy

This manuscript contains two articles which are described below. The purpose of each article is to respond to one of the two project objectives.

Article 1: Hard turning multi-performance optimization for improving the surface integrity of 300M ultra-high strength steel.

This article reports on the optimization of the surface integrity characteristics generated by hard turning of 55 HRC 300M. It concludes on (i) the most suitable optimization approach for the case studied, and on (ii) the set of hard turning cutting parameters allowing to achieve simultaneously minimum surface roughness, compressive surface residual stresses and thin white layer thickness. This article fulfills the requirements of the first objective of this thesis and was published in the International Journal of Advanced Manufacturing Technology. It is available online as of May 23rd 2019.

Article 2: High cycle fatigue behavior of hard turned 300M ultra-high strength steel.

This article reports on the fatigue behavior of finished hard turn 55 HRC 300M steel. It concludes on (i) the most suitable distribution to estimate the probability of failure in the case studied, (ii) the

absence of trends between surface integrity characteristics and fatigue life, (iii) the relationship between the fish-eye asymmetry and the ratio between the inclusion size and its position with respect to the surface and (iv) the relationship between fatigue life and inclusion size. This article fulfills the requirements of the second objective of this thesis and was accepted with minor revisions in the International Journal of Fatigue.

CHAPTER 4 ARTICLE 1: HARD TURNING MULTI-PERFORMANCE OPTIMIZATION FOR IMPROVING THE SURFACE INTEGRITY OF 300M ULTRA-HIGH STRENGTH STEEL

J. Ajaja, W. Jomaa, P. Bocher, R. R. Chromik, V. Songmene, M. Brochu. The International Journal of Advanced Manufacturing Technology. Published online May 23rd 2019.

4.1 Abstract

Hard turning technology was proven effective in enhancing the surface finish and dimensional accuracy of hardened steel. For this reason, it is used for finishing operations in the manufacturing of some critical aircraft landing gear components where bulk material hardness exceeds 45 HRC such as 300M ultra-high strength steel. Nonetheless, the selection of cutting conditions remains critical to ensure generated surface characteristics meet the performance requirements. In this context, this study focuses on the optimization of hard turning cutting conditions to reduce surface roughness, increase compressive surface residual stresses and reduce surface white layer thickness of 300M ultra-high strength steel (55 HRC). To this end, a design of experiments (DoE) is used to investigate the effects of cutting tool (T), cutting speed (V), feed rate (f) and depth of cut (D) during hard turning. The cutting tools materials investigated include PVD AlTiN coated cemented carbide, mixed ceramic, and polycrystalline Cubic Boron Nitride (PCBN), all commonly used in hard turning. Three different optimization approaches are evaluated and compared, namely the single-response Taguchi method and the multi-responses Grey relational analysis (GRA) and proportion quality loss reduction (PQLR) methodologies. Because responses were found to be correlated, the selected multi-responses optimization approaches were combined with the principal component analysis (PCA) method to transform correlated parameters into uncorrelated ones. The effect of cutting parameters and their interactions on surface roughness *Ra* and white layer thickness *WL* were considered in detail, particularly the effect of cutting tool material. Results demonstrate that the PCA-based GRA approach is a very suitable optimization technique for hard turning of 300M steel. Under those optimized conditions, surface roughness *Ra* was decreased by 50%, white layer thickness (*WL*) was decreased by 6% while compressive axial (*ASRS*) and hoop (*HSRS*) surface residual stresses were increased respectively by 307% and 74%.

4.2 Introduction

300M ultra-high strength steel is commonly used in the manufacturing of landing gear components. Many critical features in those components are machined using hard turning technology. Nevertheless, various research studies [13, 58-60] demonstrated that hard turning operations can alter the surface integrity (SI) of a part if cutting parameters and conditions are not adequately chosen. Moreover, a few authors reported that surface characteristics generated by hard turning such as surface roughness [13, 61] and residual stresses [13, 61] influence fatigue life. The complexity of the process arises from the number of cutting parameters involved, availability of commercial cutting tool materials and geometries capable to machine such hard-to-machine materials as well as machining environment (e.g. dry, wet, etc.). All can potentially have a significant influence on the surface integrity of a part.

Considering the very limited amount of literature available on 300M and the fact that this material is a modified version of the well-known AISI 4340 steel, the following literature review will combine the most relevant and recent research studies performed on those two materials. Few studies have investigated the effect of hard turning parameters (cutting speed, feed rate and depth of cut) on the surface integrity of quenched and tempered AISI 4340 [20, 22, 24, 26, 62-67] and 300M ultra-high strength steels [2, 68] with hardness varying between 37 and 57 HRC. In all cases where the effect of feed rate on surface roughness was investigated, an increase in surface roughness was reported for increasing feed rates [2, 24, 26, 67, 68]. For instance, Suresh et al. [26] reported a maximum 188% increase in surface roughness attributed to a change in feed rate from 0.10 to 0.26 mm/rev during turning of 4340 with 48 HRC hardness while Varela et al. reported a 300% increase in surface roughness attributed to a change in feed rate from 0.10 to 0.20 mm/rev during turning of 300M with 52 HRC hardness. When it comes to establishing a relationship between the effects of depth of cut and cutting speed on surface roughness, results are less in agreement. While the effect of depth of cut on surface roughness was found negligible by some researchers [2, 66, 68], it was found dependent on cutting conditions by others [20, 24, 26]. Chinchanikar et al. [24] reported an increase in surface roughness of about 25% at high depth of cut while Suresh et al. [26] reported higher values of surface roughness at low depth of cut. Lima et al. [20] investigated the effect of depth of cut on surface roughness for both 42 and 50 HRC AISI 4340 steels turned using carbide and PCBN tools respectively. A negligible effect was found in the

case of the 42 HRC steel while an unexplained drop in surface roughness was found at a depth of cut of 1mm for the steel with 50 HRC hardness.

The effect of cutting speed on surface roughness is also a subject of debate. While some studies showed a decrease in surface roughness with increase in cutting speed [20, 26], other studies either demonstrated little influence of cutting speed on surface roughness [24] or variable influence, depending on cutting conditions [20, 65]: Coto et al. [65] reported constant surface roughness values for low feed rate (f = 0.075 mm/rev) regardless of the magnitude of the cutting speed but a 25% increase in surface roughness for high feed rate (f = 0.2 mm/rev) when cutting speed was increased from 200 to 300 m/min. Lima et al. [20] reported that surface roughness showed a parabolic trend with respect to cutting speed with a minima at 120 m/min for a 42 HRC 4340 steel while Huiping et al. [68] reported the reverse trend, that is a maxima at 120 m/min, for a 50 HRC 300M steel.

When it comes to residual stresses generated during turning of 300M and AISI 4340 hard steels, even fewer studies are available in the open literature. Research studies [22, 65] demonstrated that surface residual stresses become less tensile when increasing cutting speed during turning of AISI 4340 with 42 HRC hardness. Huiping et al. [68] obtained compressive surface residual stresses during hard turning of 52 HRC 300M for different combinations of cutting conditions but common to all was a low feed rate. In contrast, Varela et al. [2] reported higher compressive surface residual stresses during turning of 300M for higher feed rates, in agreement with conclusions drawn by Jomaa et al. [69] for AISI 4340 with 58-60 HRC hardness.

As mentioned earlier, hard turning can induce microstructural transformations in the form of a white layer. Only few studies have investigated the formation of the white layer during turning of AISI 4340 steel. Akcan et al. [62], investigated the effect of cutting parameters on the formation of the white layer in 56 HRC 4340 steel and showed that high cutting speeds promoted the formation of a white layer. It is the high temperatures and heat generated at the tool/workpiece interface that allow metallurgical transformations to occur. The newly formed martensitic layer was found to have a hardness equivalent to that of a quenched martensite. The authors suggested several mechanisms for the white layer formation: deformation to very large strains followed by dynamic recrystallization, cementite precipitates decomposition or dissolution leading to a nanocrystalline structure which, along with higher hardness, would be responsible for the

featureless appearance of the white layer after etching. More recently, Jomaa et al. [69] reported on the effect of cutting speed and feed rate on the white layer formation during hard turning of induction hardened 4340 steel (60 HRC). The authors observed thin white layers (< 2 µm) as well as severe plastic deformation beneath the machined surfaces. The white layer and plastic deformed layer thicknesses were found to increase with increasing cutting speed and feed rate. Furthermore, experimental and modeling results showed that the workpiece temperature was lower than the nominal austenitic transition temperature of AISI 4340 steel (800°C), suggesting that the formation of austenite is also driven by the hydrostatic stress and the compressive plastic strain induced by hard machining.

Considering the large number of cutting parameters involved in hard turning, a statistical-based optimization study is helpful to improve the surface integrity characteristics of machined components. Only few studies focusing on the optimization of surface integrity characteristics in turning of AISI 4340 steel were published in the open literature. Agrawal et al. [70] used different regression models to study the influence of feed rate, depth of cut and cutting speed on surface roughness (*Ra*). They were able to optimize those process parameters via surface roughness predictions. Mandal et al. [71] used a desirability function combined to the response surface methodology (*RSM*) to minimize surface roughness (*Ra*) by optimizing cutting speed, feed rate and depth of cut. Bin Rashid et al. [27] used the Taguchi single-response method to minimize surface roughness (*Ra*) by optimizing feed rate, cutting speed and depth of cut. Sohrabpoor et al. [72] studied the effect of feed rate, cutting speed, depth of cut, cutting angle and mist inlet pressure on surface roughness (*Ra*) and tool wear (*VB*). They optimized those process parameters using a combination of the Taguchi and Grey Relational Analysis (GRA) methodologies. The latter approach was proven effective by Tzeng et al. [43] in optimizing turning parameters to improve simultaneously roundness and surface roughness parameters. However as suggested by Datta et al. [73], this approach should be improved further using the principal component analysis (PCA) methodology to transform any correlated responses into uncorrelated ones and consequently, eliminate any possible multi-collinearity between different responses studied. One similar approach to Taguchi-GRA-PCA is Taguchi-PQLR-PCA, a combination of the Taguchi, proportion quality loss reduction (PQLR) and PCA methods as presented in [74] by Wu et al.. Those two hybrid multiple-response optimization methods will be compared as part of the current study.

In summary, previous research studies focusing on the optimization of surface integrity in hard turning of AISI 4340 steel were limited mostly to the arithmetic surface roughness parameter and other machinability indexes such as tool wear, cutting forces and temperature. To the best of the authors' knowledge, no studies on the optimization of the overall surface integrity characteristics in hard turning of 300M ultra-high strength steel are available in the open literature. To manufacture 300M hardened steel components meeting industrial requirements in terms of fatigue performance, surface roughness, surface tensile residual stresses and white layer thickness should be all be minimized. For this reason, the multi-response optimization of hard turning parameters is necessary to generate the best surface integrity characteristics possible. To do so, the current study compares three approaches: the single-response Taguchi method and the PCA-based GRA and PQLR multi-responses optimization methodologies. The possibly existing correlations amongst the surface integrity performance responses will be addressed to determine the conditions leading to the best surface integrity in terms of surface roughness, surface residual stresses and white layer thickness.

4.3 Optimization approaches

The single-response optimization method, based on the Taguchi signal-to-noise (η), was used to determine the optimum conditions for respectively (i) three surface roughness parameters individually; *Ra*, *Rv* and *Rz*, (ii) axial surface residual stresses (*ASRS*), (iii) hoop surface residual stresses (*HSRS*), and (iv) white layer thickness (*WL*). The PCA-based GRA and PQLR methodologies were then used to determine the optimum cutting conditions for the full set of surface integrity parameters enumerated in (i) to (iv).

4.3.1 Single-response optimization method

The Taguchi methodology allows evaluating multiple process parameters but optimizing only one single response at a time [44]. This method requires the use of the signal-to-noise ratio (η) as an objective function for which three forms can be applied. The selection of one or more of these forms depend on whether a response should be minimized, maximized or converged towards a nominal value. Since the current study aims to minimize surface roughness parameters and white layer thickness and target a compressive surface residual stress value, the following forms of the signal-to-noise ratio were used [44]:

Minimum is the best

$$\eta_{ij} = -10 \log \left[\frac{1}{p} \sum_{k=1}^{p} y_{ijk}^2 \right] \quad \text{Equation (22)}$$

Nominal is the best

$$\eta_{ij} = -10 \log \left[\frac{1}{p} \sum_{k=1}^{p} \left(y_{ijk} - y_i^* \right)^2 \right] \quad \text{Equation (23)}$$

where y_{ijk} is the value of the i^{th} surface characteristic of the k^{th} replicate from experiment j, p the total number of replicates and y_i^* the nominal value. Because the function is logarithmic, the greater is the value of η_{ij}, the smaller is the sensitivity of the response variable y_{ijk} to process variations, and the greater is the influence of the control factor evaluated on the response.

Optimum conditions are found by averaging the calculated signal-to-noise (η) ratios for each parameter and level according to their distribution in the selected orthogonal array. For each parameter evaluated, the level with the highest positive average η ratio value corresponds to the optimum condition for that parameter.

4.3.2 Multi-response Optimization Approaches

Unlike the single-response Taguchi signal-to-noise method, PCA-based GRA and PQLR methodologies allow evaluating multiple process parameters and optimizing several responses at a time. Figure 23 illustrates the different steps allowing the determination of the optimum cutting conditions in terms of surface integrity (SI) characteristics.

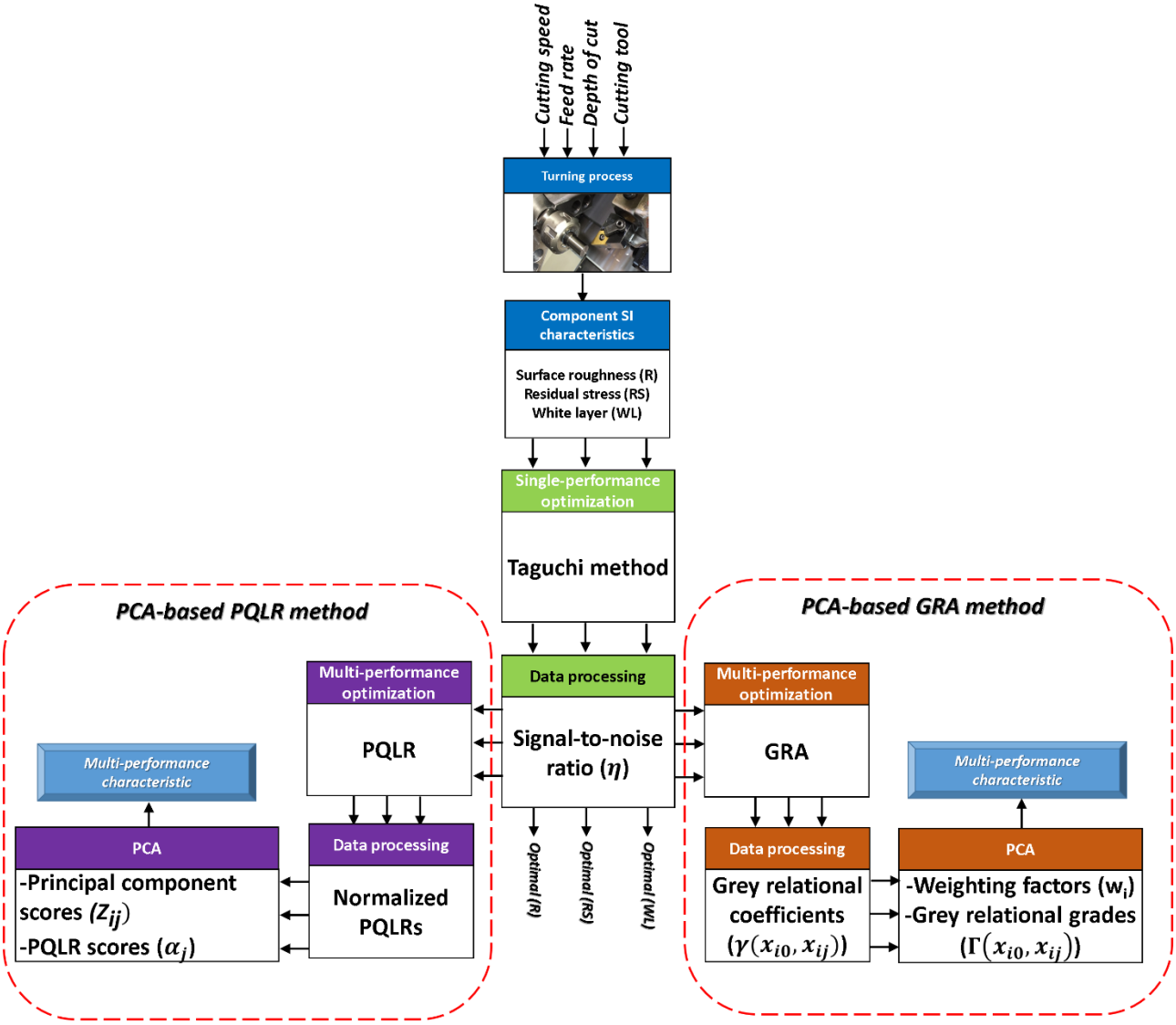

Figure 23: Scheme of the multi-responses optimization approaches applied to turned 300M ultra-high strength steel

4.3.2.1 Principal Component Analysis (PCA)

In multi-objective optimization problems, the multiple characteristics investigated are converted into a single characteristic using weighting factors. The determination of weighting factors w_i is often left to one's judgment [45] which can lead to imprecisions when defining an optimum. Therefore, the principal components analysis (PCA) is a systematic method used to determine the corresponding coefficient for each response based on their variance level. Besides, this method allows one to identify which components are responsible for most of the variance in a process [75]. First, the coefficients from the correlation matrix are calculated using Equation (24).

$$R_{ir}=\frac{cov(x_{ij},x_{ir})}{\sigma_{x_{ij}}\times\sigma_{x_{ir}}} \quad \text{Equation (24)}$$

where x_{ij} represents the normalized surface characteristic value, $cov(x_{ij},x_{ir})$ the covariance between x_{ij} and x_{ir}, $\sigma_{x_{ij}}$ the standard deviation of x_{ij} and $\sigma_{x_{ir}}$ the standard deviation of x_{ir} ($i=1,\dots,m;r=1,\dots,m$). Then, the eigenvalues λ_i and eigenvectors V_{ir} are determined from the correlation matrix using Equation 18. The eigenvectors are constituted from coefficients indicative of the relative weight of each response and used to calculate principal components ψ_{ir} from Equation (26) [76].

$$(R-\lambda_i I_i)V_{ir}=0 \quad \text{Equation (25)}$$

$$\psi_{ir}=\sum_{i=1}^{m}x_{ir}\cdot V_{ir} \quad \text{Equation (26)}$$

In the case where x_{ij} and x_{ir} are on different scales, the correlation matrix is replaced by the covariance matrix.

4.3.2.2 PCA-based GRA Methodology

The Grey relational analysis (GRA) is a method used to solve problems when relationships between process parameters is complicated [45]. It measures the degree of approximation between sequences using a single parameter named the Grey relational grade (*GRG*) [43]. The first step in the GRA consists of normalizing the experimental data corresponding to each performance characteristic as indicators can have different units and some can have a large range of values in comparison with others. For this reason, data pre-processing is required in order to transform response values into dimensionless quantities [77]. For the case where a response is minimized or converged towards a target value, the following equations are used in the same order:

$$x_{ij}=\frac{\max(\eta_{ij})-\eta_{ij}}{\max(\eta_{ij})-\min(\eta_{ij})} \quad \text{Equation (27)}$$

$$x_{ij}=1-\frac{\left|\eta_{ij}-\eta_i^*\right|}{\max\left[(\max(\eta_{ij})-\eta_i^*),(\eta_i^*-\min(\eta_{ij}))\right]} \quad \text{Equation (28)}$$

where $i = 1, \dots, m, j = 1, \dots, n$ and x_{ij} and η_{ij} represent respectively the comparative and original sequences. For each experimental run, one pre-processed value per response is obtained and those values scatter between 0 and 1 where 0 and 1 represent poor and good performances respectively [45]. Therefore, cutting conditions representative of an experimental run with pre-processed response values closer to 1 demonstrate better overall performance.

Grey relational coefficients (*GRCs*) can determine how close the compatibility and reference sequences are one to another and are calculated using Equation (29). The reference sequence refers to an ideal performance represented by pre-processed values x_{i0} equal to 1.

$$\gamma(x_{i0}, x_{ij}) = \frac{\Delta\min + \xi\Delta\max}{\Delta_{ij} + \xi\Delta\max} \qquad \text{Equation (29)}$$

where $x_{i0} = \{1, \dots, 1\}$, $\Delta_{ij} = \left|x_{i0} - x_{ij}\right|$, $\Delta_{min} = \min \Delta_{ij}$, $\Delta_{max} = \max \Delta_{ij}$ and $\xi \in [0,1]$. The distinguishing coefficient ξ is used to expand or compress the range of the *GRC* and is set to 0.5 in the present work as suggested in [45].

Once the *GRCs* are determined, the Grey relational grades (*GRGs*) Γ can be calculated using Equation (30).

$$\Gamma\left(x_{i0}, x_{ij}\right) = \sum_{i=1}^{m} w_i \cdot \gamma(x_{i0}, x_{ij}) \qquad \text{Equation (30)}$$

where w_i represents the weighting factor for the i^{th} response parameter with $\sum_{i=1}^{m} w_i = 1$. The higher the Grey relational grade, the greater the correlation between x_{i0} and x_{ij} [43], the closer the optimum.

In the current case, only the first principal component, accounting for most of the variance, was used to determine the weighting factors, corresponding to the contribution of each response evaluated to the overall variance:

$$w_i = {\psi_{i1}}^2 \qquad \text{Equation (31)}$$

Optimum cutting parameters are found by averaging the values of the calculated Grey relational grades (*GRGs*) for each parameter and level according to their distribution in the selected

orthogonal array. For each parameter evaluated, the level with the highest average *GRG* value corresponds to the optimum condition for that parameter.

4.3.2.3 PCA-based PQLR Methodology

This optimization method requires the selection of a starting experimental condition against which other conditions will be compared. For each response and experiment, a signal-to-noise ratio is calculated and used to determine the proportion of quality loss reduction (PQLR) which can be calculated according to Equation 32 where η_0 represent the signal-to-noise ratio for the chosen starting condition [74].

$$x_{ij} = (PQLR)_{ij} = 10^{-\frac{\eta_{ij}-\eta_0}{10}} \quad \text{Equation (32)}$$

PQLR values are then normalized to calculate the principal component scores Z_{ij} using eigenvectors obtained from the principal component analysis (PCA) [74].

$$Z_{ij} = \left[\frac{x_{ij} - \min x_{ij}}{\max x_{ij} - \min x_{ij}}\right] \cdot \psi_{ir} \quad \text{Equation (33)}$$

In the current case, the first four principal component scores were used to calculate the weighted PQLR scores (α_j) using Equation (34) considering they account for most of the total process variance [74]:

$$\alpha_j = \sum_{j=1}^{n} w_i |Z_{ij}| \quad \text{Equation (34)}$$

Here, weighting factors w_i consist in the contribution of each principal component to the entire variability and are determined using the Eigenvalues extracted from the covariance matrix, where the highest value corresponds to the greatest amount of variability.

Optimum cutting parameters are found by averaging the values of the calculated weighted PQLR scores for each parameter and level according to their distribution in the selected orthogonal array. For each parameter evaluated, the level with the lowest average PQLR weighted score value corresponds to the optimum condition for that parameter. In this case, the lower the weighted PQLR score, the closer the optimum, the better the performance.

4.4 Experimental procedure

4.4.1 Workpiece Material

The material used in the present study is AMS 6257E 300M ultra-high strength steel. Its chemical composition (weight %) was measured by spark atomic emission spectrometry and is as follows: 0.36 %C, 1.53 %Si, 1.76% Ni, 0.84% Mn, 0.73% Cr and 0.07% V. Cylindrical specimens extracted from 15 mm diameter bars, which were quenched and tempered to 55 HRC were used for the machining tests. No stress relief treatment was applied to the specimens. Figure 24 shows the martensitic structure of the material obtained in its quenched and tempered state and was acquired by electron channeling contrast imaging (ECCI).

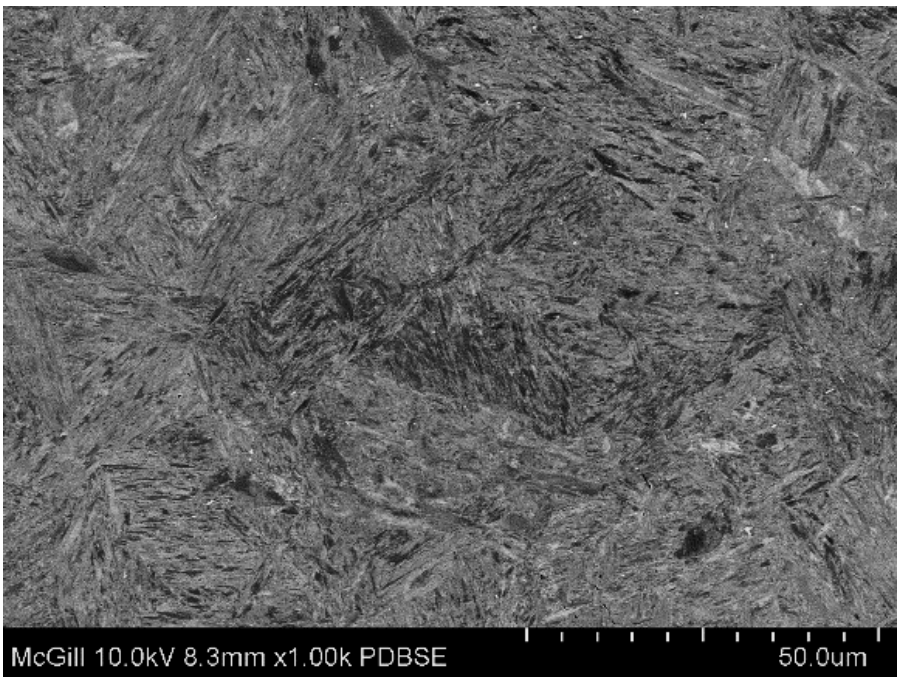

Figure 24: Martensitic structure of 300M ultra-high strength steel quenched and tempered to 55 HRC.

4.4.2 Machining tests

Turning tests were performed on a Mazak QTN-100 CNC lathe under wet cutting conditions (Figure 25). Four cutting parameters, namely cutting speed (V), feed rate (f), depth of cut (D), and cutting tool (T) were investigated. Three cutting tool inserts commonly utilized in hard turning were used; a PVD AlTiN coated cemented carbide DNGA150408 (KC5010), a PVD TiN coated

composite ceramic (Al_2O_3/TiCN) DNGA150408 EFW (KY4400), and a nano-composite coated low-content polycrystalline cubic boron nitride PCBN grade (DNGA150408 S01015MT (KBH20)). All three inserts have a constant nose radius of 0.8 mm. The combination of the tool holder (MDJNR124B) and a tool insert resulted in a rake angle of -5°. Cutting parameters levels were selected to cover various semi-finishing and finishing hard turning operations conditions. To avoid any possible tool wear effects on surface integrity characteristics, a new cutting edge was used for each machining test. All machined specimens were subjected to a macroscopic (visual) and microscopic (optical microscope) inspection. Machining tests were performed according to the design of experiment described in the following section.

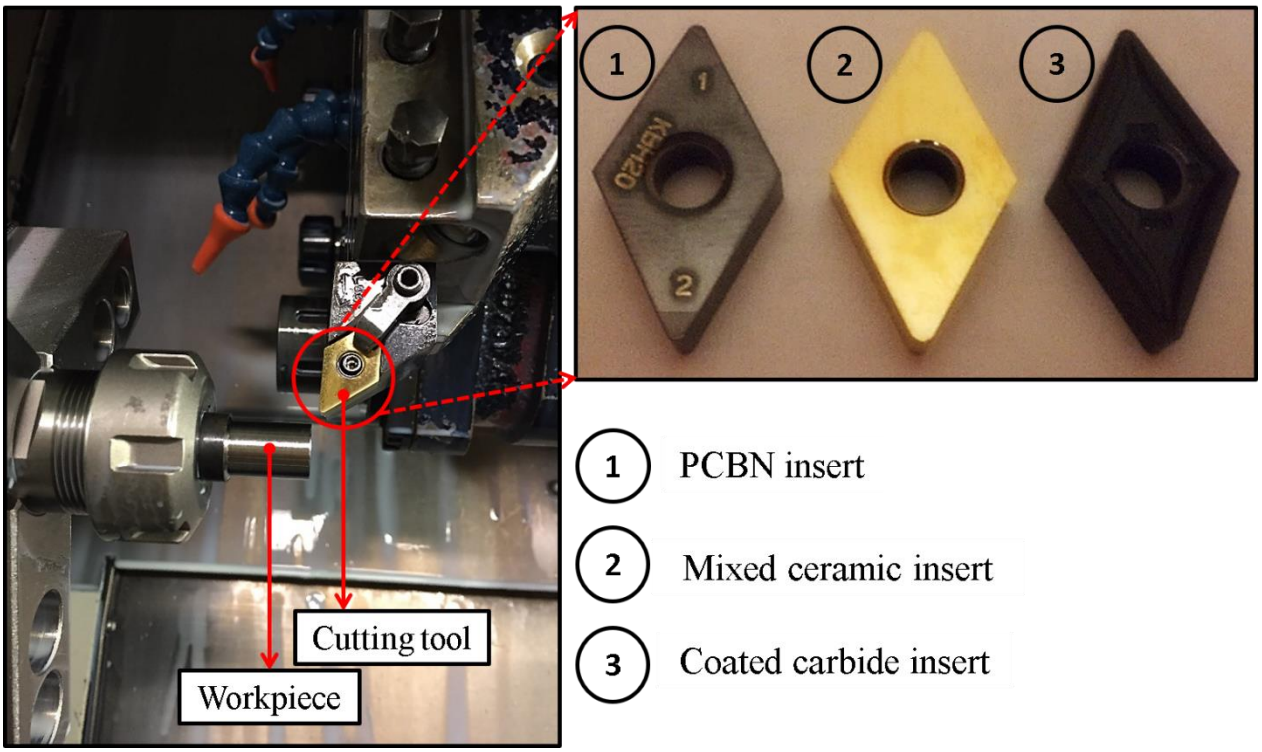

Figure 25: Machining setup and cutting tool inserts

4.4.3 Experimental Design

Cutting parameters levels (Table 11) and machining conditions were selected according to a L_9 Taguchi orthogonal array (Table 12). The use of orthogonal arrays allows for a balanced experimental design where all control factors are weighted equally and where a minimum number

of experiments is required. In the current study, each machining test was repeated three times in order to get a better estimation of the experimental measurements' repeatability and deviation.

Table 11: Hard turning parameters and levels

Level	Control factors			
	Tool material, *T*	Cutting speed, *V* [m/min]	Feed rate, *f* [mm/rev]	Depth of Cut, *D* [mm]
1	Carbide	50	0.051	0.254
2	Ceramic	75	0.127	0.508
3	PCBN	100	0.203	0.762

Table 12: Taguchi L_9 orthogonal design of experiment (DoE).

Run	Control factors							
	Coded				Uncoded			
	T	*V*	*F*	*D*	*T*	*V* [m/min]	*f* [mm/rev]	*D* [mm]
1	1	1	1	1	T1	50	0.051	0.254
2	1	2	2	2	T1	75	0.127	0.508
3	1	3	3	3	T1	100	0.203	0.762
4	2	1	2	3	T2	50	0.127	0.762
5	2	2	3	1	T2	75	0.203	0.254
6	2	3	1	2	T2	100	0.051	0.508
7	3	1	3	2	T3	50	0.203	0.508
8	3	2	1	3	T3	75	0.051	0.762
9	3	3	2	1	T3	100	0.127	0.254

4.4.4 Experimental Measurement Techniques

Surface roughness parameters were measured in the feed direction using a LEXT OLS4100 laser confocal microscope with a cut-off of 0.8 mm. Surface residual stresses were measured in two directions (axial and hoop) according to the cos(α) single-angle method using a μ-X360 portable x-ray residual stress analyzer with a 1 mm beam aperture. One specimen per experimental run was metallographically prepared to perform white layer thickness measurements. Specimens were cut using an Acuttom precision cutter, grinded from 120 grits and polished to 0.05 μm using a Tegramin automatic specimen preparation system. Polished specimens were etched using a Nital 2% solution to reveal the microstructure of the material and white layer thickness measurements were performed on SEM images obtained using a 25.0 kV voltage on a SU3700 scanning electron microscope. Ten measurements were taken on each specimen along the feed direction (longitudinal

direction of the bar) to account for the inhomogeneity of the white layer thickness distribution in a typical specimen.

4.5 Results and discussion

4.5.1 Single response optimization: Taguchi analysis

Experimental measurements of surface roughness parameters and surface residual stresses obtained from the nine experimental runs are presented in Table 13. The arithmetic average *Ra*, maximum depth of valleys *Rv* and average peak-to-valley height *Rz* varied respectively between 0.26 to 1.62 µm, 0.77 to 2.80 µm and 1.36 to 6.76 µm. Axial (*ASRS*) and hoop (*HSRS*) surface residual stresses varied from tensile to compressive levels, respectively from 26 to -836 MPa and 203 to -384 MPa. The white layer thickness *WL* was found to range between 0.69 and 1.24 µm. The highest η ratio for surface roughness parameters *Ra*, *Rv* and *Rz* were obtained under Run 4. Similarly, the highest η ratios for axial and hoop residual stresses were obtained under Runs 6 and 7, respectively, while the highest η ratio for *WL* was obtained under Run 6.

Table 13: Experimental and signal-to-noise (η) values for each response and run.

Run	Experimental values						Signal-to-noise values					
	Ra [µm]	*Rv* [µm]	*Rz* [µm]	*ASRS* [MPa]	*HSRS* [MPa]	*WL* [µm]	*Ra* [dB]	*Rv* [dB]	*Rz* [dB]	*ASRS* [dB]	*HSRS* [dB]	*WL* [dB]
1	0.28	1.13	1.71	-199	54	0.86	10.96	-1.02	-4.64	-62.28	-54.86	1.33
2	0.69	1.63	3.71	-234	-219	0.81	3.22	-4.25	-11.38	-62.05	-48.96	1.84
3	1.58	2.80	5.80	-78	-325	0.82	-3.97	-8.95	-15.26	-63.06	-44.88	1.73
4	**0.26***	**0.77**	**1.36**	-179	-145	0.81	**11.57**	**2.25**	**-2.66**	-62.42	-51.01	1.80
5	0.44	0.98	2.27	26	203	1.24	7.11	0.18	-7.11	-63.67	-56.94	-1.85
6	0.40	1.11	2.38	**-836**	-252	**0.69**	8.22	-0.89	-7.53	**-56.44**	-47.88	**3.21**
7	1.62	2.63	6.76	-121	**-384**	0.86	-4.17	-8.41	-16.60	-62.79	**-41.29**	1.30
8	0.27	0.89	1.60	-155	38	0.89	11.50	1.00	-4.07	-62.58	-54.61	1.03
9	0.62	1.04	2.58	-154	-109	0.77	4.21	-0.38	-8.23	-62.58	-51.84	2.25

*****bold values highlight the optimal responses

Interaction plots were generated to understand and highlight the relationships that may exist among the investigated control factors. The interaction plots for the surface roughness parameter *Ra* are displayed in Figure 26. Results demonstrate that the effect of cutting speed and feed rate on surface roughness is dependent on the cutting tool material used. While carbide inserts were found to perform better (lower roughness) than mixed ceramic and PCBN inserts at low cutting speed, the reverse trend is true for higher cutting speeds (Figure 26a).The surface roughness obtained by

PCBN inserts was found to be strongly affected by the feed rate (Figure 26b) when compared to carbide and mixed ceramic inserts. In general, the surface roughness *Ra* increases with increase in feed rate, in agreement with previous work [12]. However, the feed rate was found to have a marginal effect on *Ra* at the lowest depth of cut (0.254 mm).

Figure 27a shows that the effect of cutting speed on axial surface residual stresses (*ASRS*) was limited when using carbide and mixed ceramic inserts while a strong variation of the response was observed for PCBN inserts. PCBN inserts did not demonstrate a significant interaction with feed rate (Figure 27b) when compared to carbide inserts for which the interaction is strong. The *ASRS* increases withe feed rate with the most significant effects recorded at a depth of cut of 0.508 mm (Figure 27c). As shown in Figure 28 a) and b), hoop surface residual stresses (*HSRS*) were found to be significantly sensitive to the interactions between cutting speed, feed rate and cutting tool. Unlike axial surface residual stress, hoop surface residual stresses generally decrease with feed rate, except for the case where the depth of cut is 0.254 mm (Figure 28 c).

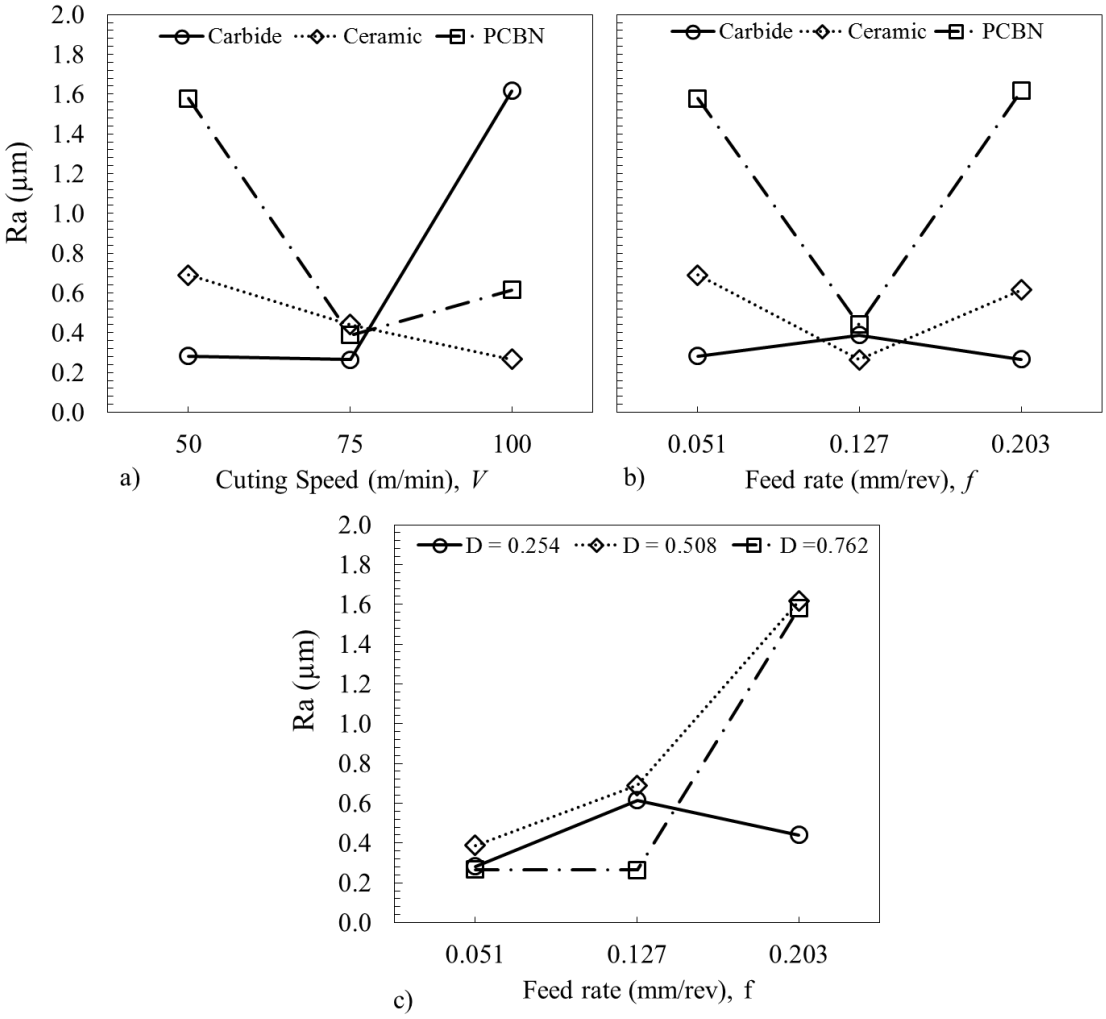

Figure 26: Interaction plots for *Ra*.

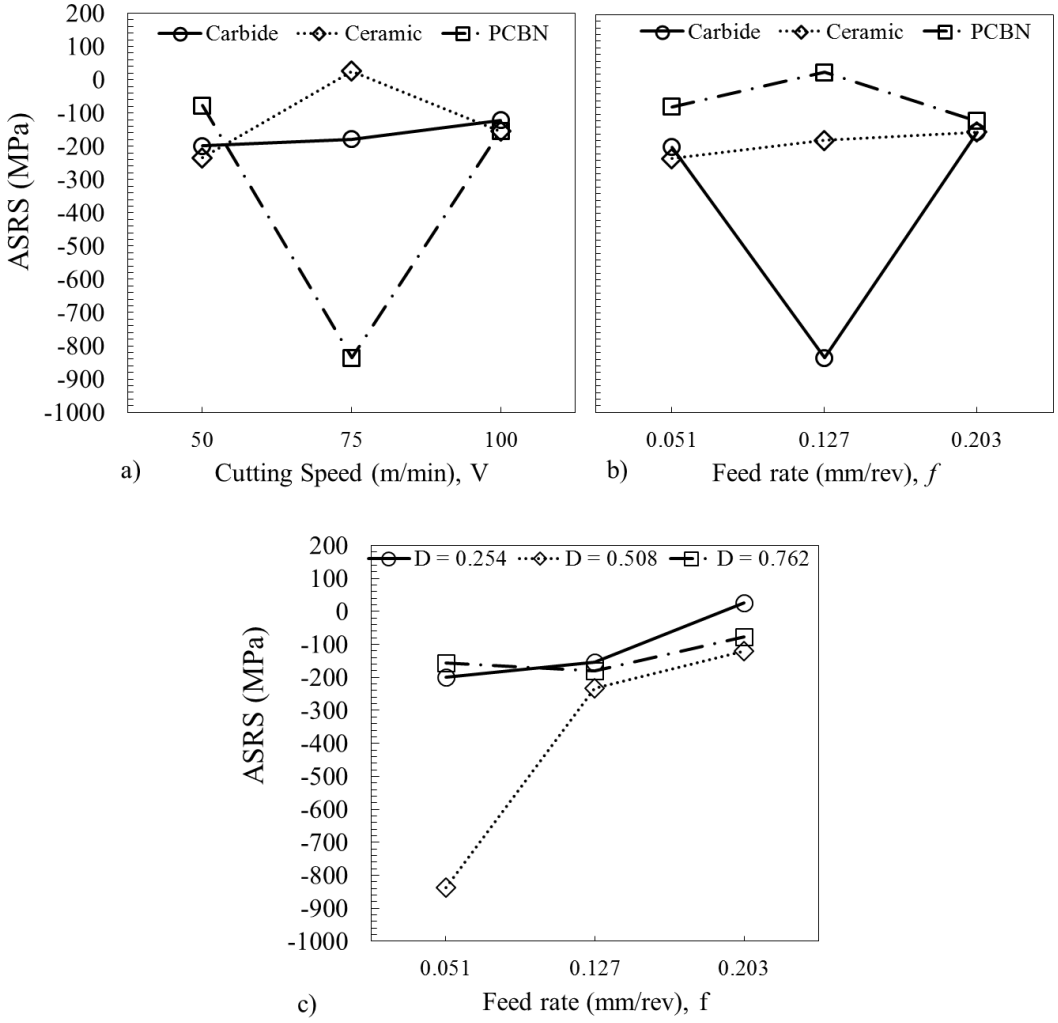

Figure 27: Interaction plots for *ASRS*.

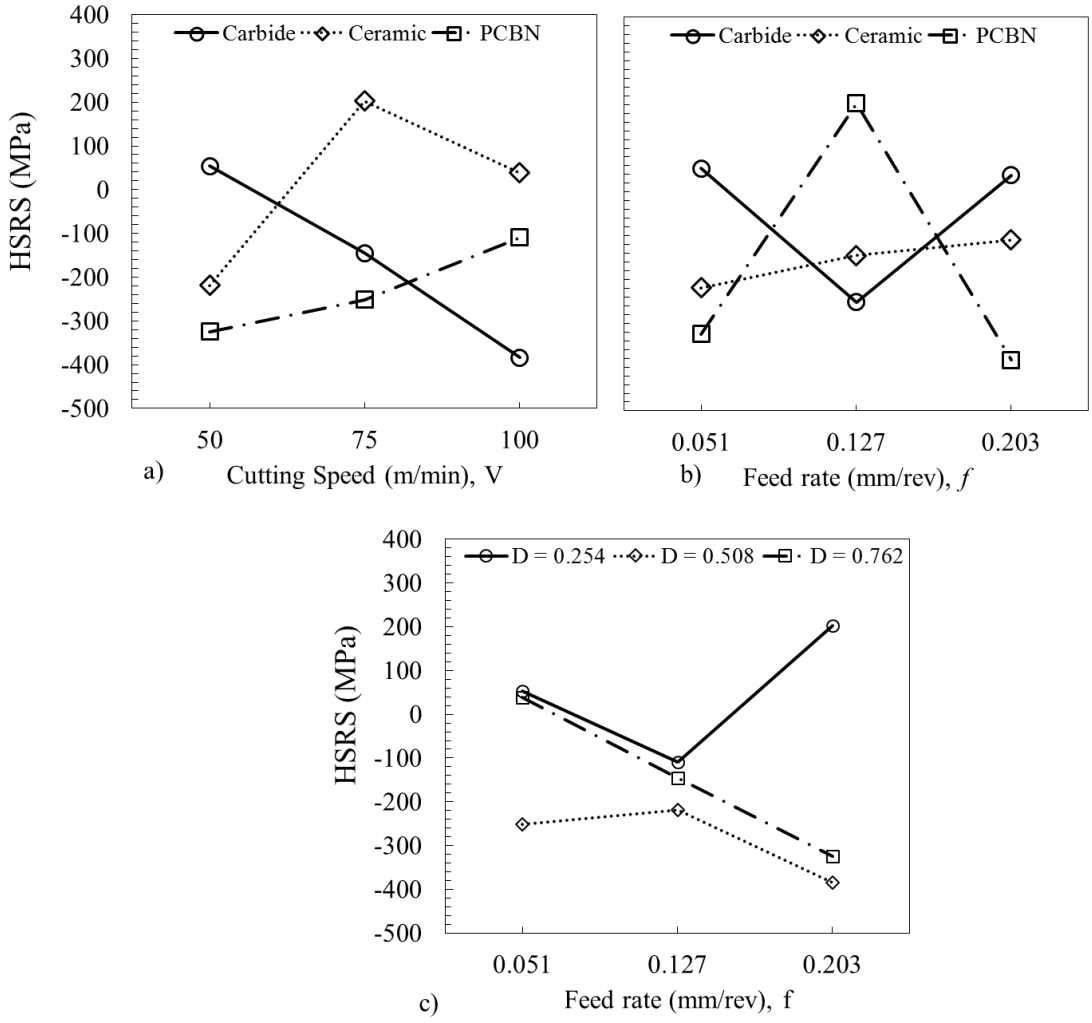

Figure 28: Interaction plots for *HSRS*.

The percent contribution of each control factor to the six responses variance was determined using an analysis of variance (ANOVA) at a confidence level of 95%. Table 14 shows that feed rate *f* has the greatest influence on all surface roughness parameters (contribution of 57% for *Ra*, 41% for *Rv*, and 48% for *Rz*) as well as on *ASRS* (contribution of 27%) while depth of cut *D* and cutting speed *V* have the greatest influence on respectively *HSRS* (contribution of 45% for *D*) and white layer thickness *WL* (contribution of 42% for *D*).

Table 14: Percent contribution of control factors to all responses determined by ANOVA.

Control Factor	Percent contribution (*rank*)					
	Ra	*Rv*	*Rz*	*ASRS*	*HSRS*	*WL*
T	19 (*2*)	32 (*2*)	20 (*3*)	22 (*4*)	10 (*4*)	4 (*4*)
V	10 (*4*)	7 (*4*)	7 (*4*)	24 (*3*)	20 (*3*)	42 (*1*)
F	57 (*1*)	41 (*1*)	48 (*1*)	27 (*1*)	25 (*2*)	30 (*2*)
D	14 (*3*)	20 (*3*)	25 (*2*)	27 (*2*)	45 (*1*)	24 (*3*)

The Taguchi method applied to the surface roughness parameters and white layer thickness used the smaller-the-better function (Equation 1) while the nominal-the-best function (Equation 2) was used for axial and hoop surface residual stresses with target values respectively of -1500 and -500 MPa (Table 13). The optimal combination of control parameters is obtained using the mean η ratio calculated by averaging the η ratios for the experiments performed at the same parameter levels. In the current paper, four different optimum conditions were determined, one per performance characteristic studied. The lowest surface roughness was found at *T2V2f1D1* (new condition) for all three surface roughness parameters evaluated. The highest level of compressive surface residual stresses was found at *T2V3f1D2* (Run 6 in Table 2) for *ASRS* and *T3V1f3D2* (Run 7 in Table 2) for *HSRS*. Finally, the smallest white layer thickness was found at *T1V3f2D2*. Since all these machining conditions are different, it is difficult to find the machining parameters combination that will optimize all the responses at the same time based on the Taguchi method.

4.5.1.1 Confirmation tests

Confirmation tests were carried to validate the obtained optimum cutting conditions. The comparison between predicted values and experimental data obtained at the optimum conditions is necessary to verify the validity of the proposed optimization approach. The estimated values at the optimal level can be predicted using Equation (35) [74]:

$$\hat{n} = n_m + \sum_{i}^{q} (\bar{n}_i - n_m) \qquad \text{Equation (35)}$$

where $\hat{n}$ and n_m represent respectively the predicted and total mean of the performance characteristic values, $\bar{n}_i$ the mean value at the optimum and q the number of process parameters. A set of specimens was machined using machining parameters selected for optimal *Ra*, *Rv*, *Rz*, *ASRS*,

HSRS, and WL. Then, the obtained experimental results were compared to the predicted ones. Results of the confirmation tests together with those of the initial cutting parameters for all responses studied are presented in Table 15. The combination of machining conditions *T1V2f2D2* (Run 2 of the proposed DoE) was selected as a reference since the corresponding cutting tool (*T1*), speed (*V2*), feed rate (*f2*), and depth of cut (*D2*) are recommended by the tool manufacturers and commonly used by the industrial partner in finishing operations.

Unexpectedly, results in Table 5 shows that the minimum surface roughness is obtained at the machining conditions minimizing the white layer thickness (*T1V3f2D2*) rather than at (*T2V2f1D1*). Further, the surface roughness values predicted using Equation 15 are significantly lower than the experimental results. Nonetheless, the predicted minima agree with the values obtained experimentally for axial and hoop surface residual stresses representing the highest level of compressive surface residual stresses.

Compared to the reference condition *T1V2f2D2*, all four optima determined by the Taguchi single-optimization approach performed better. In particular, condition *T2V2f1D1* (new condition) decreased *Ra*, *Rv* and *Rz* by respectively 45%, 30% and 32%. Condition *T2V3f1D2* (Run 6) increased compressive *ASRS* by 257%, condition *T3V1f3D2* (Run 7) increased compressive *HSRS* by 75% and condition *T1V3f2D2* decreased *WL* by 20%. Furthermore, according to the results presented in Table 15, a comparison between predicted and experimental values shows that predictions made using the Taguchi method are overestimated for surface roughness by a factor of two, suggesting the limitations of the single-response optimization approach.

Table 15: Taguchi confirmation tests results.

	Reference condition	Optimum conditions							
		Ra, Rv, Rz		*ASRS*		*HSRS*		*WL*	
Level	*T1V2f2D2*	*T2V2f1D1*		*T2V3f1D2*		*T3V1f3D2*		*T1V3f2D2*	
		Pred.	Exp.	Pred.	Exp.	Pred.	Exp.	Pred.	Exp.
Ra [µm]	0.69	0.13	0.38		0.38		1.61		0.27
Rv [µm]	1.63	0.53	1.14		1.01		2.34		0.78
Rz [µm]	3.71	0.95	2.52		2.44		6.69		2.05
ASRS [MPa]	-234		-938	-836	-836		-121		84
HSRS [MPa]	-219		-298		-252	-384	-384		326
WL [µm]	0.81		0.94		0.69		0.86	0.64	0.65

*Pred.: Prediction
*Exp. Experimental

A close analysis of the machined specimens using a laser confocal microscope revealed significant variation in the surface microgeometry obtained under the four optimum conditions (Figure 29). In fact, the optimal cutting conditions for roughness parameters (*T1V2f2D2*) and axial residual stresses (*T2V3f1D2*) generate different surface microgeometries despite similar arithmetic average *Ra* values (~ 0.38 µm). This dissimilarity can be detected either visually or with the skewness (*Rsk*) and kurtosis (*Rku*) roughness parameters. The *Ra*-based optimal condition (Figure 29b) has a lower positive *Rsk* value (0.355) and a *Rku* value lower than three (2.831) whereas The *ASRS*-based optimal condition (*T2V3f1D2*) generates a surface texture (Figure 29b) with a higher positive *Rsk* value (0.768) and a *Rku* value higher than three (3.238). This means that the surface machined under the *ASRS*-based optimal condition is dominated by sharp peaks. Similarly, despite the significant similarity in *Ra* value (0.274) compared with the *Ra*-based optimal condition, the *WL*-based optimal condition (Figure 29d) generates significantly different surface textures with *Rsk* and *Rku* values equal to 0.997 and 4.094, respectively. The *HSRS*-optimal condition (Figure 29c) generates a higher arithmetic average *Ra* in comparison with the three other optima where the feed marks are very clean and the fluctuations reduced. This can be attributed to the higher feed rate used (0.203 mm/rev) in this condition. To explain this particular trend, one should consider not only the process parameters but also the cutting tool inserts used which can have a significant effect on surface texture as reported by Grzesik et al. [78]. As shown in Figure 29d, despite the medium cutting feed used, the surface profile obtained with the carbide insert experiences large fluctuations with deep scratches at the bottom of the feed marks due to the presence of hard precipitates and carbides in the work material microstructure as observed by Poulachon et al. [79]. This was not observed when mixed ceramic (Figure 29a and b) and PCBN inserts were used as these tool materials have advanced mechanical and chemical properties allowing higher resistance to abrasion when compared to carbide inserts.

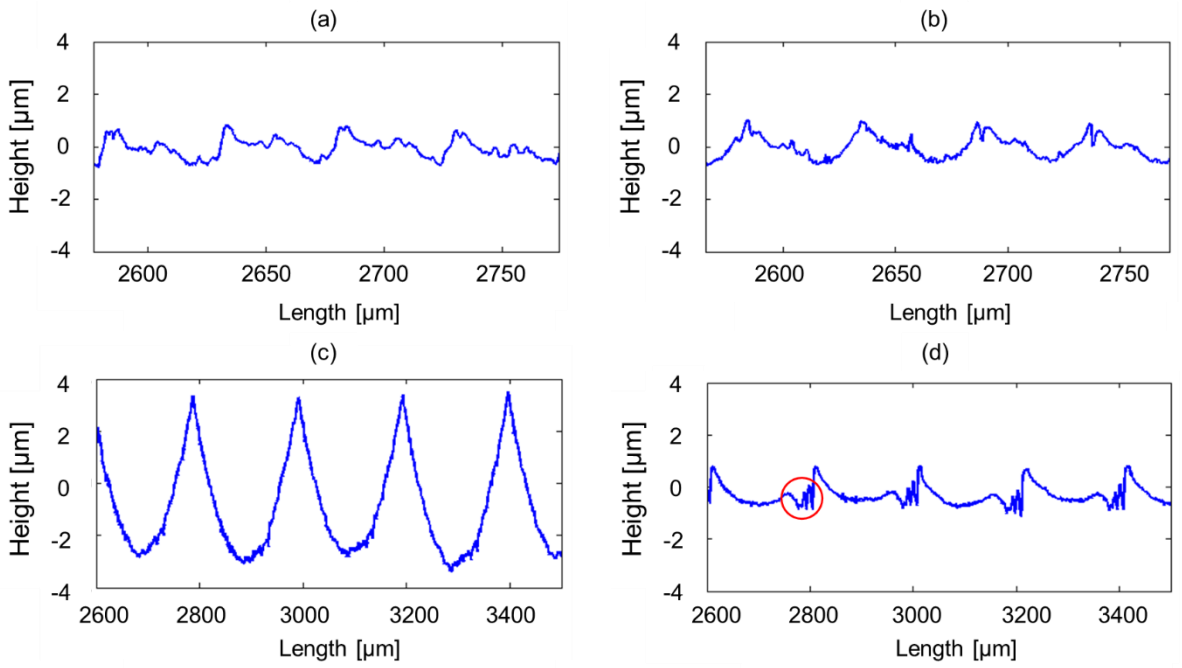

Figure 29: Surface roughness profiles for optimized conditions corresponding to a) surface roughness (*T1V2f2D2*), b) axial residual stress (*T2V2f1D1*), c) hoop residual stress (*T3V1f3D2*), and d) white layer thickness (*T1V3f2D2*).

4.5.2 PCA-based multi-response optimization

Data pre-processing is required prior to further analysis of both PCA-based multi-response optimization methods in order to transform response values into normalized dimensionless quantities. Pre-processed data are listed in Table 16 according to the optimization method used and performance characteristics evaluated.

Table 16: Pre-processed experimental data prior to further analysis.

Run	PCA-based GRA						PCA-based PQLR					
	Ra	*Rv*	*Rz*	*ASRS*	*HSRS*	*WL*	*Ra*	*Rv*	*Rz*	*ASRS*	*HSRS*	*WL*
Ref.	**1.00**	**1.00**	**1.00**	**1.00**	**1.00**	**1.00**	**1.00**	**1.00**	**1.00**	**1.00**	**1.00**	**1.00**
1	0.96	0.71	0.86	0.19	0.13	0.63	0.00	0.09	0.02	0.66	0.61	0.25
2	0.47	0.42	0.37	0.22	0.51	0.73	0.16	0.28	0.27	0.62	0.14	0.17
3	0.01	0.00	0.10	0.08	0.77	0.71	0.95	1.00	0.72	0.84	0.04	0.19
4	1.00	1.00	1.00	0.17	0.38	0.72	0.00	0.00	0.00	0.69	0.23	0.17
5	0.72	0.82	0.68	0.00	0.00	0.00	0.05	0.05	0.07	1.00	1.00	1.00
6	0.79	0.72	0.65	1.00	0.58	1.00	0.03	0.09	0.09	0.00	0.10	0.00
7	0.00	0.05	0.00	0.12	1.00	0.62	1.00	0.87	1.00	0.77	0.00	0.25
8	1.00	0.89	0.90	0.15	0.15	0.57	0.00	0.03	0.02	0.73	0.57	0.30
9	0.53	0.77	0.60	0.15	0.33	0.81	0.12	0.07	0.11	0.73	0.29	0.11

In the case of the PCA-based GRA method, the *GRGs* are determined using the deviation sequences along with weighting factors obtained by PCA. The weighting factors in this particular case were obtained from the first principal component accounting for most of the process variability (61.9 %). The weighting factors corresponding to *Ra, Rv, Rz, ASRS, HSRS, and WL* are w_1= 0.251, w_2 = 0.251, w_3 = 0.256, w_4 = 0.001, w_5 = 0.223, w_6 = 0.018, respectively, with $\sum w_i = 1$.

In the case of the PCA-based PQLR method, the weighted PQLR scores are calculated using principal component scores along with weighting factors obtained by PCA. Here, weighting factors were determined from four out of six principal components accounting for a total of 99.3% of the process variability as shown in Table 17.

Table 17: Eigenvalues and percent contribution of the four major principal components.

	ψ_{i1}	ψi_2	ψi_3	ψi_4	Total
Eigenvalue	0.49	0.19	0.02	0.01	
Contribution (%)	68.6	26.1	3.5	1.1	99.3

Table 18 provides the weighted GRGs and PQLR scores calculated along with their order. In a similar way to the Taguchi-based single response optimization method, the optimum combination can be determined by averaging the weighted GRGs and PQLR scores for each process parameter using the balanced orthogonal array. As illustrated in Figure 30, the optimum conditions obtained from PCA-based GRA and PQLR optimization approaches are respectively *T2V1f1D3* and *T2V2f1D1*. It is worth noting that these optimum conditions are different from the conditions

corresponding to the highest weighted GRGs and lower PQLR score displayed in Table 18. For this reason, confirmation tests were carried out to validate the new optima obtained.

Table 18: Weighted GRGs and PQLR scores and corresponding order.

Run	PCA-based GRA		PCA-based PQLR	
	Weighted Grey relational grade	Order	Weighted PQLR score	Order
1	0.68	3	0.32	4
2	0.48	8	0.41	6
3	0.42	9	1.27	8
4	0.87	1	0.21	2
5	0.58	5	0.65	7
6	0.63	4	0.07	1
7	0.49	7	1.33	9
8	0.76	2	0.35	5
9	0.55	6	0.26	3

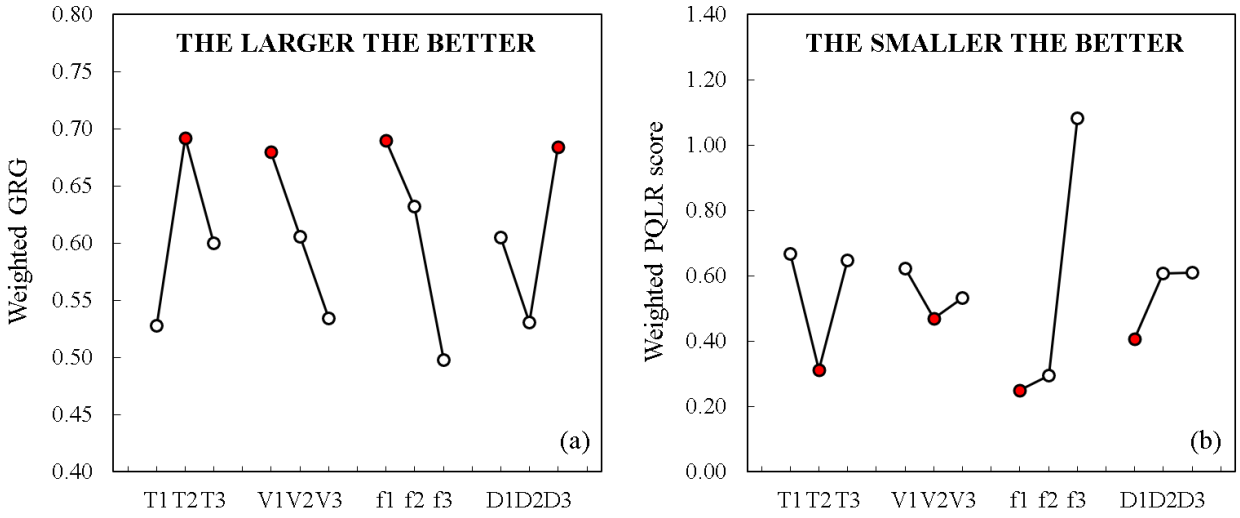

Figure 30: Multi-response optimization results: a) PCA-based Grey method and b) PCA-based PQLR method.

4.5.2.1 Confirmation Tests

Confirmation tests were performed to assess the reliability of the multiple-response optimization approaches used in this study. Experimental results generated using the multi-response optimum conditions are presented in Table 19. PCA-based GRA performed better than both the reference condition *T1V2f2D2* and PCA-based PQLR for all responses evaluated. Specifically, *Ra*, *Rv* and *Rz* were decreased by respectively 50%, 31% and 44%; compressive *ASRS* and *HSRS* increased by

respectively 307% and 74%, and *WL* decreased by 6%. Furthermore, the relative error between the experimental and predicted GRG is about 17% while it can reach values as high as 246 % for the PQLR score, suggesting the better reliability of the PCA-based GRA method as compared to the PCA-PQLR method. This can be attributed to the differences in the construction of both investigated methods. Unlike the PQLR scores, the GRA is based on the optimization of the GRGs which are linked in a direct way to the responses. While the GRGs represent a direct linear combination of the normalized responses values, the PQLR scores are calculated based on a double linearization process between the principal components and the PQLR values. Thus, a part of the experimental information can be lost, resulting in the inaccuracy of the optimization process.

Table 19: PCA-based GRA and PQLR confirmation tests results.

	Reference condition	Optimum condition			
		PCA-based GRA		PCA-based PQLR	
Response		Prediction	Experimental	Prediction	Experimental
	T1V2f2D2	*T2V1f1D3*	*T2V1f1D3*	*T2V2f1D1*	*T2V2f1D1*
Ra [µm]	0.690		0.346		0.379
Rv [µm]	1.632		1.128		1.143
Rz [µm]	3.706		2.068		2.523
ASRS [MPa]	-234		-953		-938
HSRS [MPa]	-219		-380		-298
WL [µm]	0.81		0.76		0.94
GRGs		0.93	0.76		
PQLR Score				-0.19	0.13

Since the calculated optima involve the same cutting tool (*T2*) and feed rate (*f1*) but different cutting speed and depth of cut, it is interesting to investigate how much these parameters affect the surface microgeometry and microstructure. The optimal PCA-based GRA condition produced surface textures (Figure 31a) with negative skewness, that is with more valleys, (*Rsk* = -0.448) while surfaces with positive skewness (*Rsk* = 0.355) were produced under PCA-based PQLR optimum conditions, that is with more peaks (Figure 31b). In addition, both optimal PCA-based GRA and PCA-PQLR conditions generated surfaces with a kurtosis roughness parameter *Rku* lower than 3; that is 2.63 for PCA-based GRA and 2.83 for PCA-based PQLR. Conclusively, the machined surface obtained under the optimal PCA-based GRA condition is better in terms of wear control and bearing surface functionality because a high kurtosis is associated with flat regions

providing low contact stresses and a negative skewness is related to deep valleys providing lubricant reservoirs [80].

For the PCA-based GRA method, the use of low cutting speed and high depth of cut favors two contributive effects. First, the cutting temperature is reduced and second, a high amount of heat generated by material removal can be evacuated by the chips due to their larger width; the inverse being true for the PCA-based PQLR method. In fact, the use of larger depths of cut increases the cutting forces which in turn favors the mechanical effect, the latter being known to introduce compressive residual stresses and large plastic deformations [69]. This results in higher *HSRS* (Table 19) and larger thickness of the deformed layer (*DL*) as shown in (Figure 31a).

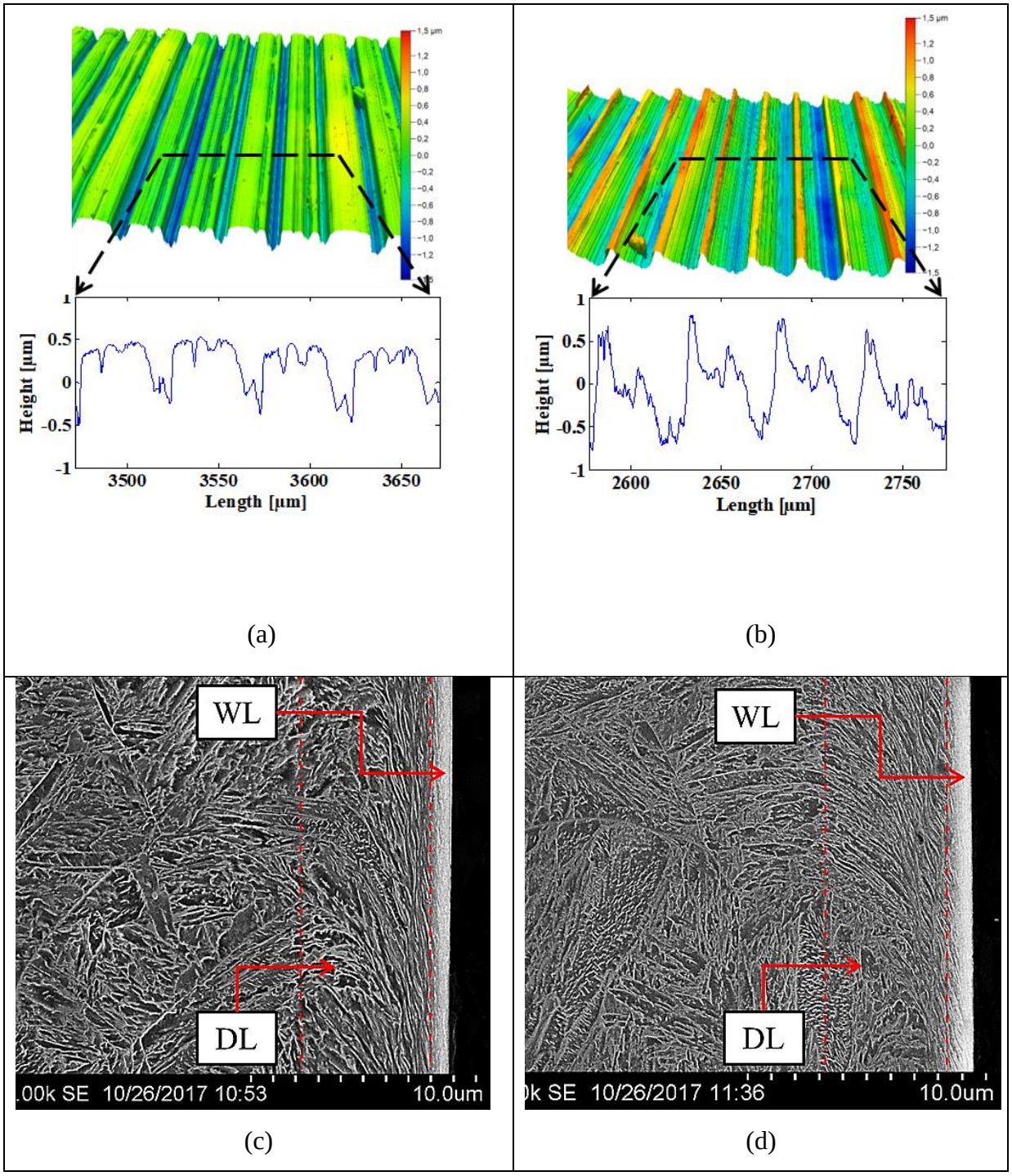

Figure 31: SEM images of white layer and surface topography for optimized conditions corresponding to a) and b) surface texture and c) and d) microstructure corresponding to GRA and PQLR optima, respectively.

4.6 Conclusion

The objective of the current study was to determine hard turning cutting conditions under which the surface integrity of 55 HRC 300M steel is optimized for fatigue performance. Starting from reference hard turning conditions used in production, various parameters were changed and samples manufactured according to industrial surface integrity requirements. One single-response and two multiple-responses optimization approaches were used to obtain a set of optimum cutting conditions. Multiple-responses optimizations were carried using the principle component analysis (PCA) combined to both grey relational analysis (GRA) and proportion of quality loss reduction (PQLR) methodologies. Results from those different methods were analyzed and compared, allowing to draw the following conclusions:

- The Taguchi single-response optimization approach provided an optimum for each response optimized. The most significant optimum was obtained by generating a 257% increase in compressive axial residual stresses. Nonetheless, considering that only one characteristic at a time is optimized, no improvement can be guaranteed for the other surface integrity characteristics.
- The Taguchi single-response optimization method is not an accurate approach for optimizing several surface integrity characteristics at the same time because of the existing interactions between the various control factors. For this reason, two multi-responses optimization methods based on the PCA approach were used in order to take into account the correlated variables and generate weighting factors.
- Both optimum conditions obtained by PCA-based GRA and PCA-based PQLR generate significantly improved surface integrity compared to the reference condition.
- The surface integrity obtained using the optimum generated by the PCA-based GRA was better that that produced by the PCA-based PQLR optimum. For instance, the former

decreased *Rz* by 44% and increased compressive *HSRS* by 74% while the latter decreased *Rz* by 32% and increased compressive *HSRS* by 36%.

- Confirmation tests and predicted data showed that PCA-based GRA is more reliable than PCA-based PQLR. In fact, the relative error between the experimental and predicted GRGs is about 17% while it can reach values as high as 246 % for PQLR scores.
- The best set of surface characteristics generated by hard turning of 55 HRC 300M for fatigue considerations is obtained under conditions where a mixed ceramic insert is used along with low cutting speed (V = 50 m/min), low feed rate (f = 0.051 mm/rev) and large depth of cut (D = 0.762 mm).
- A detailed investigation of the surface texture and microstructure revealed some other interesting surface integrity aspects which cannot be captured with usual roughness parameters such as the deformed layer thickness.

4.7 Acknowledgments

This work was supported by the Consortium for Research and Innovation in Aerospace in Quebec (CRIAQ), MITACS, the Natural Sciences and Engineering Research Council (NSERC), Héroux-Devtek and Pratt & Whitney Canada.

4.8 References

1. Totten, G.E., *Effects of Alloying Elements on the Heat Treatment of Steel*, in *Steel Heat Treatment: Metallurgy and Technologies*, C. Press, Editor. 2006. p. 166-211.
2. Liu, F., et al., *Microstructure and mechanical properties of laser solid formed 300M steel.* Journal of Alloys and Compounds, 2015. **621**: p. 35-41.
3. Manigandan, K., et al., *Cyclic Strain Resistance, Stress Response, Fatigue Life, and Fracture Behavior of High Strength Low Alloy Steel 300 M.* Journal of Materials Engineering and Performance, 2014. **23**(5): p. 1799-1814.

4. Carvalho, S.M.d. and M.S.F.d. Lima, *Laser beam welding tempered 300M ultrahigh mechanical strength steel.* Journal of the Brazilian Society of Mechanical Sciences and Engineering, 2012. **34**(1): p. 18-23.
5. Davis J.R., M.K.M., Lampman S.R., *Ultrahigh-Strength Steels*, in *Properties and Selection: Irons, Steels, and High-Performance Alloys*, A. International, Editor. 1990.
6. Davim, J.P., *Machining: fundamentals and recent advances*. 2008: Springer Science & Business Media.
7. Altintas, Y., *Manufacturing automation: metal cutting mechanics, machine tool vibrations, and CNC design*. 2012: Cambridge university press.
8. Grzesik, W., *Chapter Three - Trends in Metal Cutting Theory and Pratice*, in *Advanced Machining Processes of Metallic Materials*, W. Grzesik, Editor. 2008, Elsevier: Amsterdam. p. 17-26.
9. Matsumoto, Y., F. Hashimoto, and G. Lahoti, *Surface integrity generated by precision hard turning.* CIRP Annals - Manufacturing Technology, 1999. **48**(1): p. 59-62.
10. Tönshoff, H.K., C. Arendt, and R.B. Amor, *Cutting of Hardened Steel.* CIRP Annals, 2000. **49**(2): p. 547-566.
11. König, W., A. Berktold, and K.F. Koch, *Turning versus Grinding – A Comparison of Surface Integrity Aspects and Attainable Accuracies.* CIRP Annals, 1993. **42**(1): p. 39-43.
12. Huiping, Z., Z. Hongxia, and L. Yinan, *Surface roughness and residual stresses of high speed turning 300 M ultrahigh strength steel.* Advances in Mechanical Engineering, 2014. **2014**.
13. Varela, P.I., C.S. Rakurty, and A.K. Balaji. *Surface integrity in hard machining of 300M Steel: Effect of cutting-edge geometry on machining induced residual stresses*. in *Procedia CIRP*. 2014.
14. Zheng, G., et al., *Effect of cutting parameters on wear behavior of coated tool and surface roughness in high-speed turning of 300M.* Measurement, 2018. **125**: p. 99-108.
15. Rashid, W.B., et al., *Parametric design optimization of hard turning of AISI 4340 steel (69 HRC).* International Journal of Advanced Manufacturing Technology, 2016. **82**(1-4): p. 451-462.
16. Mandal, N., B. Doloi, and B. Mondal, *Predictive modeling of surface roughness in high speed machining of AISI 4340 steel using yttria stabilized zirconia toughened alumina turning insert.* International Journal of Refractory Metals and Hard Materials, 2013. **38**: p. 40-46.
17. Agrawal, A., et al., *Prediction of surface roughness during hard turning of AISI 4340 steel (69 HRC).* Applied Soft Computing Journal, 2015. **30**: p. 279-286.
18. Sohrabpoor, H., S.P. Khanghah, and R. Teimouri, *Investigation of lubricant condition and machining parameters while turning of AISI 4340.* International Journal of Advanced Manufacturing Technology, 2014. **76**(9-12): p. 2099-2116.
19. Tzeng, C.-J., et al., *Optimization of turning operations with multiple performance characteristics using the Taguchi method and Grey relational analysis.* Journal of Materials Processing Technology, 2009. **209**(6): p. 2753-2759.
20. Nalbant, M., H. Gökkaya, and G. Sur, *Application of Taguchi method in the optimization of cutting parameters for surface roughness in turning.* Materials and Design, 2007. **28**(4): p. 1379-1385.
21. Kuo, Y., T. Yang, and G.-W. Huang, *The use of a grey-based Taguchi method for optimizing multi-response simulation problems.* Engineering Optimization, 2008. **40**(6): p. 517-528.

22. Dickinson, G. *The Influence of Machining on the Performance of Ultra High Strength Steels*. in *ASME 1970 International Gas Turbine Conference and Products Show*. 1970. American Society of Mechanical Engineers.
23. Bag, A., et al., *Statistical analysis of high cycle fatigue life and inclusion size distribution in shot peened 300M steel.* International Journal of Fatigue, 2019. **118**: p. 126-138.
24. Pistochini, T.E. and M.R. Hill, *Effect of laser peening on fatigue performance in 300M steel.* Fatigue and Fracture of Engineering Materials and Structures, 2011. **34**(7): p. 521-533.
25. Putatunda, S.K., M. Nambiar, and N. Clark, *Influence of laser hardening on mechanical properties of a low alloy steel.* Surface Engineering, 1997. **13**(5): p. 407-414.
26. Hill, M.R., T.E. Pistochini, and A.T. DeWald, *Fatigue Performance of Laser Peened Materials.* 2005(41928): p. 203-207.
27. Rech, J. and A. Moisan, *Surface integrity in finish hard turning of case-hardened steels.* International Journal of Machine Tools and Manufacture, 2003. **43**(5): p. 543-550.
28. Zhang, X., C.R. Liu, and Z. Yao, *Experimental study and evaluation methodology on hard surface integrity.* International Journal of Advanced Manufacturing Technology, 2007. **34**(1-2): p. 141-148.
29. Javidi, A., U. Rieger, and W. Eichlseder, *The effect of machining on the surface integrity and fatigue life.* International Journal of Fatigue, 2008. **30**(10–11): p. 2050-2055.
30. Akcan, S., et al., *Formation of white layers in steels by machining and their characteristics.* Metallurgical and Materials Transactions A: Physical Metallurgy and Materials Science, 2002. **33**(4): p. 1245-1254.
31. Capello, E., et al., *Relaxation of residual stresses induced by turning and shot peening on steels.* Journal of Strain Analysis for Engineering Design, 2004. **39**(3): p. 285-290.
32. Chinchanikar, S. and S.K. Choudhury, *Effect of work material hardness and cutting parameters on performance of coated carbide tool when turning hardened steel: An optimization approach.* Measurement: Journal of the International Measurement Confederation, 2013. **46**(4): p. 1572-1584.
33. Chinchanikar, S. and S.K. Choudhury, *Investigations on machinability aspects of hardened AISI 4340 steel at different levels of hardness using coated carbide tools.* International Journal of Refractory Metals and Hard Materials, 2013. **38**: p. 124-133.
34. Coto, B., et al., *Influences of turning parameters in surface residual stresses in AISI 4340 steel.* The International Journal of Advanced Manufacturing Technology, 2011. **53**(9-12): p. 911-919.
35. Çydaş, U., *Machinability evaluation in hard turning of AISI 4340 steel with different cutting tools using statistical techniques.* Proceedings of the Institution of Mechanical Engineers, Part B: Journal of Engineering Manufacture, 2010. **224**(7): p. 1043-1055.
36. Lima, J.G., et al., *Hard turning: AISI 4340 high strength low alloy steel and AISI D2 cold work tool steel.* Journal of Materials Processing Technology, 2005. **169**(3): p. 388-395.
37. Navas, V.G., O. Gonzalo, and I. Bengoetxea, *Effect of cutting parameters in the surface residual stresses generated by turning in AISI 4340 steel.* International Journal of Machine Tools and Manufacture, 2012. **61**: p. 48-57.
38. Sahu, S. and B.B. Choudhury, *Optimization of Surface Roughness Using Taguchi Methodology & Prediction of Tool Wear in Hard Turning Tools.* Materials Today: Proceedings, 2015. **2**(4): p. 2615-2623.

39. Suresh, R., et al., *Machinability investigations on hardened AISI 4340 steel using coated carbide insert.* International Journal of Refractory Metals and Hard Materials, 2012. **33**: p. 75-86.
40. Jomaa, W., V. Songmene, and P. Bocher, *An Investigation of Machining-Induced Residual Stresses and Microstructure of Induction-Hardened AISI 4340 Steel.* Materials and Manufacturing Processes, 2016. **31**(7): p. 838-844.
41. Datta, S., et al., *Application of PCA-based hybrid Taguchi method for correlated multicriteria optimization of submerged arc weld: a case study.* The International Journal of Advanced Manufacturing Technology, 2009. **45**(3): p. 276.
42. Wu, F.-C. and C.-C. Chyu, *Optimization of correlated multiple quality characteristics robust design using principal component analysis.* Journal of Manufacturing Systems, 2004. **23**(2): p. 134-143.
43. Lu, H.S., et al., *Grey relational analysis coupled with principal component analysis for optimization design of the cutting parameters in high-speed end milling.* Journal of Materials Processing Technology, 2009. **209**(8): p. 3808-3817.
44. Fung, C.P. and P.C. Kang, *Multi-response optimization in friction properties of PBT composites using Taguchi method and principle component analysis.* Journal of Materials Processing Technology, 2005. **170**(3): p. 602-610.
45. Huang, J.T. and Y.S. Liao, *Optimization of machining parameters of Wire-EDM based on Grey relational and statistical analyses.* International Journal of Production Research, 2003. **41**(8): p. 1707-1720.
46. Grzesik, W. and T. Wanat, *Surface finish generated in hard turning of quenched alloy steel parts using conventional and wiper ceramic inserts.* International Journal of Machine Tools and Manufacture, 2006. **46**(15): p. 1988-1995.
47. Poulachon, G., et al., *The influence of the microstructure of hardened tool steel workpiece on the wear of PCBN cutting tools.* International Journal of Machine Tools and Manufacture, 2003. **43**(2): p. 139-144.
48. Griffiths, B., *4 - Surface Finish Characterization*, in *Manufacturing Surface Technology*, B. Griffiths, Editor. 2001, Kogan Page Science: Oxford. p. 109-151.
49. Robertson, G.T., *The Effects of Shot Size on the Residual Stresses Resulting from Shot Peening*. 1971, SAE International.
50. Murakami, Y., T. Nomoto, and T. Ueda, *Factors influencing the mechanism of superlong fatigue failure in steels.* Fatigue & Fracture of Engineering Materials & Structures, 1999. **22**(7): p. 581-590.
51. Murakami, Y., S. Kodama, and S. Konuma, *Quantitative evaluation of effects of non-metallic inclusions on fatigue strength of high strength steels. I: Basic fatigue mechanism and evaluation of correlation between the fatigue fracture stress and the size and location of non-metallic inclusions.* International Journal of Fatigue, 1989. **11**(5): p. 291-298.
52. De la Cruz, P., M. Odén, and T. Ericsson, *Influence of plasma nitriding on fatigue strength and fracture of a B-Mn steel.* Materials Science and Engineering: A, 1998. **242**(1-2): p. 181-194.

CHAPTER 5 ARTICLE 2: HIGH CYCLE FATIGUE BEHAVIOR OF HARD TURNED 300M ULTRA-HIGH STRENGTH STEEL

J. Ajaja, W. Jomaa, P. Bocher, R. R. Chromik, M. Brochu. International Journal of Fatigue. Published online November 22nd 2019.

5.1 Abstract

Although the effects of hard turning on surface integrity have been extensively studied over the past decades, the fatigue behavior of hard turned ultra-high strength steels is still not completely understood. This study investigated the influence of surface integrity characteristics generated by hard turning on the rotating bending fatigue life of 55 HRC 300M steel. Four finish cutting conditions were used to generate different combinations of surface integrity characteristics. Resulting fatigue lives ranged between 1.01·105 and 9.84·106 cycles for a stress amplitude of 965 MPa. A single distribution was able to fit the entire fatigue life data showing that the finish hard turning conditions evaluated are comparable. A fractographic analysis showed that specimens failed under two different crack initiation mechanisms: surface feed marks and subsurface Al2O3·CaO·MgO inclusions. Murakami's K_max equation for surface defects underestimates the severity of machined surfaces and cannot explain the competition between the two crack initiation mechanisms.

5.2 Introduction

Landing gear components such as struts are manufactured from hardened 300M ultra-high strength steel, a modified version of the well known AISI 4340. Finishing operations involved in the production of those cylindrical parts are performed by hard turning because it produces parts with acceptable surface integrity, that is with dimensional accuracy, surface roughness and residual stress levels that should not promote early fatigue failures.

The following literature survey gathers the very few studies published on the influence of machining on the fatigue behavior of 300M and 4340 steels. Dickinson et al. [1] studied the influence of various machining processes on the fatigue strength of 56-58 HRC 300M steel at R =

0. Under optimum cutting conditions, it was found that turning generated surfaces resulting in higher fatigue strength (993 MPa) at a million cycles in comparison with milling (827 MPa), but lower in comparison with grinding (1007 MPa). Further, a series of ground specimens was stress relieved to study the effect of residual stresses generated by machining on fatigue strength. It was found that the removal of those residual stresses reduced the bending fatigue life of ground hardened 300M steel although this reduction was not quantified. Matsumoto et al. [2] compared the performance of 54 HRC 4340 steel specimens machined under fly cutting and finish grinding conditions subjected to axial fatigue at R = 0.1. They observed that fly cutting generated surfaces leading to higher fatigue strength when compared with finish grinding due to a greater depth of compressive residual stresses and a lower maximum height of the profile roughness parameter Rz. Results presented in Siqueira et al. [3] show that the presence of machining tool marks resulting from roughing conditions (Ra = 5.38 mm) in 30 HRC 4340 steel promoted crack initiation at the surface and decreased fatigue strength by 30% under rotating bending fatigue when compared to the polished material. Buddy Damm [4] investigated the influence of surface finish generated by grinding on the fatigue strength of 52 HRC 4340 steel. They produced specimens with three types of surface finish: fine (Ra = 0.10 ± 0.11 μm), medium (Ra = 0.25 ± 0.09 μm) and rough (Ra = 0.77 ± 0.10 μm). The fatigue strength at 107 cycles was found to be 958 MPa for the fine surface finish in comparison with 827 MPa for the rough surface finish. Further, the percentage of failures initiating at the surface varied from 80% to 46% to 100% for the fine, medium and rough surface finishes respectively. Therefore, a medium surface finish generated less failures initiating at surface inclusions than a fine surface finish, but this unexpected behavior was not explained.

Studies published on the influence of surface integrity resulting from surface treatments such as peening on the fatigue behavior of 300M steel are also very limited. Pistochini et al. [5] studied the effect of peening on the fatigue performance of 54 HRC 300M steel subjected to four-point bending fatigue loading conditions at a stress ratio R = 0.1. They compared the fatigue strength of laser peened specimens with the one of low stress grinded and conventionally shot peened specimens. Results showed that specimens in their as-machined condition had a fatigue strength of 881 MPa at 106 cycles and that laser and shot peening increased fatigue strength by 55% and 39% respectively. Such increase was explained by the large and deep field of compressive residual stresses [5, 6]. Crack nucleation was reported at the surface for as-machined specimens and at

subsurface inclusions for shot peened specimens, at depths greater than the depth affected by shot peening (250 µm). Bag et al. [7] also studied the effects of shot peening on the high cycle fatigue (HCF) life of 54 HRC 300M steel subjected to fully reversed axial fatigue loading and compared the fatigue behavior of shot peened specimens with that of polished and machined specimens. When compared to the polished condition, results demonstrated that machining and shot peening were responsible for over 100% increase in fatigue life. As-peened specimens were characterized by a surface roughness parameter Ra varying between 0.75 and 1.44 µm while as-machined specimens were characterized by an Ra of 0.31 µm. Although shot peening generated much higher surface compressive residual stresses (in the order of -1000 MPa) when compared to machining (-400 MPa), no significant difference in terms of fatigue life was found between the two processes. The authors reported that under the peening conditions studied, only one specimen failed due to a crack initiating at the surface. The other specimens' failures were all caused by cracks originating from internal inclusions.

In summary, only a few studies investigated the fatigue behavior of machined 300M and 4340 steels. The machined condition is typically used as a reference to compare with fatigue properties generated by other surface treatments such as shot peening. Therefore, considering the limited amount of data gathered from the presented literature, complete conclusions cannot be drawn on the influence of machining processes and surface integrity on the fatigue performance of 300M and 4340 steels. Under bending loading conditions, surface and in-depth residual stresses were reported as beneficial for fatigue strength [1, 5, 6] in some cases while in others, the same levels of surface and in-depth residual stresses were found to have no influence on fatigue life [7]. The effect of surface roughness on fatigue is not well understood either but it is believed that surface roughness and residual stress influence fatigue strength together [2]. No study investigated the relationship between cutting parameters, generated surface characteristics and resulting fatigue life or strength in 300M and 4340 steels. In order to tackle this challenge, the current study investigates the influence of surface characteristics, namely surface roughness and surface residual stresses, generated by different hard turning cutting conditions on the rotating bending fatigue life of 55 HRC 300M steel.

5.3 Experimental procedure

5.3.1 Work material

The material used in the current study is 300M ultra-high strength steel. Its chemical composition (weight %) was measured by spark atomic emission spectrometry as per ASTM E415-14 and found below the maximum requirements prescribed by AMS6257E as shown in Table 20. The material was quenched and tempered to a hardness of 55 HRC as per AMS2759-2F. Tensile properties were measured according to ASTM E8-8M and compared to the minimum requirements prescribed by AMS6257E as shown in Table 21. The microstructure of the material in its quenched and tempered state is a lath martensite (Figure 32a) and the average diameter of the prior-austenitic grain (Figure 32b) is 9.5 µm (ASTM 10.5). To measure the grain size, a sample was etched using a solution heated to 80-90 °C consisting of water saturated with picric acid and mixed with HCl (1 mL in 500 mL of water) and 15 mL of wetting agent. The grain size was measured on three different images taken at a 1000X magnification on a Keyence digital microscope.

Table 20: Chemical composition (wt.%) of 300M ultra-high strength steel.

	C	Mn	Si	P	S	Cr	Ni	Mo	V	Cu	Fe
300M	0.36	0.84	1.53	0.008	0.001	0.73	1.76	0.39	0.07	0.25	bal.
AMS6257E max.	0.44	0.90	1.80	0.010	0.008	0.95	2.00	0.45	0.10	0.35	bal.

Table 21: Average monotonic mechanical properties of 300M ultra-high strength steel based on four measurements.

	YS [MPa]	UTS [MPa]	El [%]
300M	1701 ± 17	2018 ± 9	12 ± 1
AMS6257E min.	1586	1931	8

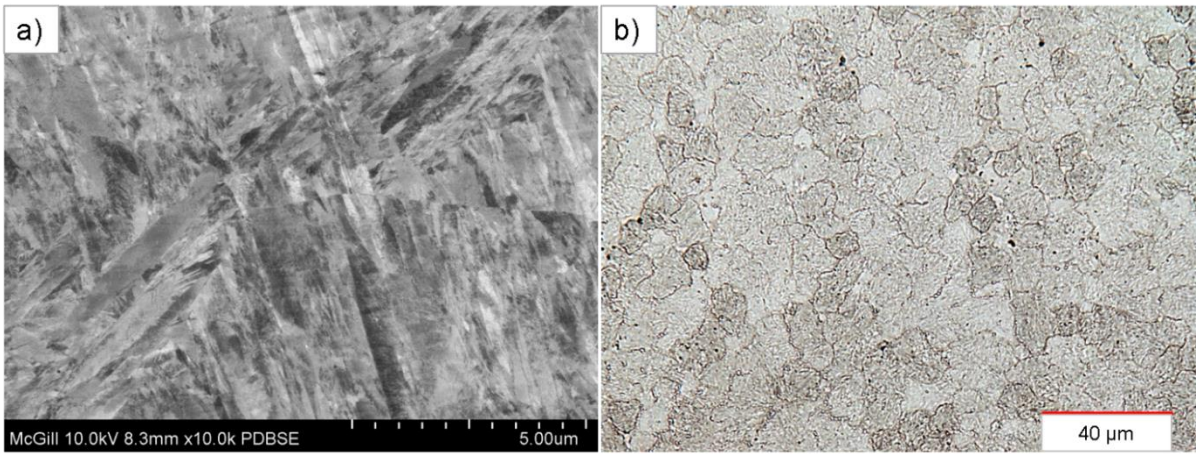

Figure 32: Microstructure of the material studied showing a) martensite laths observed by electron channeling contrast imaging (ECCI) and b) prior-austenitic grains.

5.3.2 Hard turning of fatigue specimens

Fatigue specimens were machined from 15 mm heat treated diameter bars to the geometry and dimensions illustrated in Figure 33.

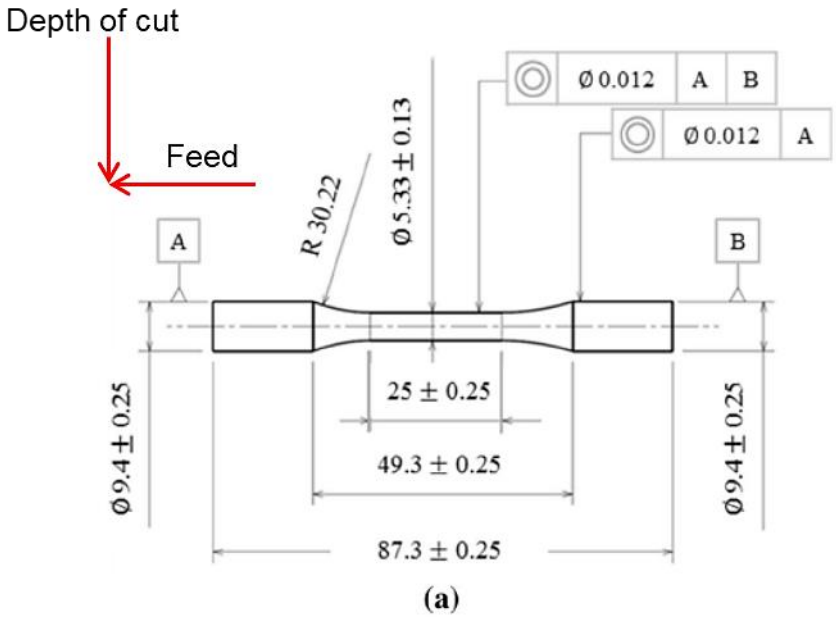

Figure 33: RR Moore rotating bending fatigue test specimens. Dimensions given in millimetres.

A three-step machining procedure including roughing, semi-finishing and finishing operations was used to control final surface integrity characteristics. Various finishing operations carried out under wet conditions were tested using PVD AlTiN coated cemented carbide (DNGA150408 -grade

KC5010) inserts. The selected cutting parameters used to machine the fatigue specimens are presented in Table 22 and were based on cutting tools manufacturers recommendations and a previous investigation [81]. The cutting speed *V*, feed rate *f* and depth of cut *D* were varied between 55 – 100 m/min, 0.053 and 0.152 mm/rev and 0.245 – 0.490 mm respectively. The main objective was to produce fatigue specimens with an arithmetic average surface roughness (*Ra*) meeting the industrial requirement in terms of surface finish (*Ra* < 1 µm).

Table 22: Hard turning cutting conditions used to machine RR Moore fatigue specimens

Cutting Condition	Number of specimens	Cutting speed, *V* [m/min]	Feed rate, *f* [mm/rev]	Depth of Cut, *D* [mm]
C1	3	85	0.053	0.490
C2	3	55	0.152	0.245
C3	3	100	0.053	0.490
C4	4	69	0.053	0.319

5.3.3 Surface integrity characterization

5.3.3.1 Surface roughness

Surface finish was characterized by surface roughness measurements in the feed direction using a laser confocal microscope with a cut-off length of 0.8 mm. Seven different parameters were measured including four amplitude parameters (*Ra*, *Rt*, *Rq* and *Rv*), one spacing parameter (*Rsm*) and two statistical parameters (*Rsk*, *Rku*). A detailed description of surface roughness parameters is given in Petropoulos et al. [82].

5.3.3.2 Surface residual stresses

Surface and in-depth residual stresses were measured in axial and hoop directions according to the cos(α) single-angle method using a Pulstec µ-X360 portable X-ray residual stress analyzer with a Cr source with a 1 mm beam aperture and an angle of 35°. In-depth residual stresses were measured within a maximum depth of 140 µm corresponding to the machined affected layer. To measure in-depth residual stresses, specimens were electropolished using a saline solution to uncover a new surface at varying interval depths. Three measurements were taken on three locations per specimen and used to calculate the average residual stress values.

5.3.3.3 White layer thickness

One specimen per cutting condition was metallographically prepared to measure the white layer thickness. Specimens were cut in the transverse direction using a precision cutter, grinded from 120 grits and polished to 0.05 μm using an automated specimen preparation system. Polished specimens were etched using a Nital 2% solution to reveal the white layer thickness and measurements were performed on SEM images obtained using a 25 kV voltage on a SU3700. Ten measurements were taken on each specimen along the feed direction to account for the inhomogeneity of the white layer thickness distribution along the circumference of a given cross-sectional plane.

5.3.4 Fatigue tests and fractography

Fatigue tests were carried out on a RR Moore high-speed rotating beam fatigue testing machine at a rotation speed of 3300 rpm, under a stress amplitude σ_a of 965 MPa and a stress ratio R of -1. The number of tested machined specimens is reported in Table 22. A test was interrupted if the specimen had not failed following 10 million cycles. Fractographic images were taken on all failed specimens using a SU3700 scanning electron microscope at 25 kV.

5.4 Results and discussion

5.4.1 Surface integrity characteristics

5.4.1.1 Surface finish

Average surface roughness values for all studied surface roughness parameters and cutting conditions are presented in

Table 23. All machining conditions produced an arithmetic average roughness *Ra* < 1 µm except condition C2 for which the *Ra* value was found to be a little higher (1.1 µm). This condition produced the highest amplitude surface roughness parameters, namely *Ra*, maximum peak-to-valley *(Rt)*, root mean square *(Rq)* and deepest valley *(Rv)* due to the high feed rate (f = 0.152 mm/rev) used. This result is in agreement with a general trend observed in machining processes and in particular by Varela et al. [2] who investigated the influence of turning cutting parameters on surface roughness in 52 HRC 300M steel. The authors work showed that increasing feed rate increases surface roughness for constant cutting speed and depth of cut.

In an ideal surface roughness profile, the mean spacing of the asperities *Rsm* should correspond to the feed rate [83]. In this study, the *Rsm* values for conditions C1, C3 and C4 range between 2 to 4 times the feed rate used (53 µm) while they are in the same order of magnitude as the feed rate used for condition C2. These results suggest that the surface roughness formation mechanisms vary not only due to feed rate but also to cutting speed, depth of cut and their interactions. The surface profiles presented in Figure 34 show that the feed marks are barely recognizable in conditions C1 (Figure 34 b), C3 (Figure 34 d), and C4 (Figure 34 e). For these conditions, the surface profiles are dominated by many sharp peaks and low valleys, resulting in kurtosis *Rku* values above 3. Additionally, surface roughness profiles for conditions C1 and C4 exhibit blunt features with deep scratches, resulting in negative skewness values (*Rsk* = -0.07; -0.36), while condition C3 generated a surface profile with shallow valleys and high peaks, resulting in a relatively high positive skewness (*Rsk* = 1).

The profiles presented in Figure 34 along with the surface roughness parameters presented in

Table 23 show that conventional amplitude roughness parameters are not sufficient to describe the complexity of the surface features that can possibly influence fatigue life. For instance, although cutting conditions C1, C3 and C4 have the same level of *Ra*, their *Rsm* and *Rsk* are significantly different. Thus, in the present study, in addition to the conventional amplitude parameters, spacing and statistical parameters including the mean spacing of the asperities (*Rsm*), the kurtosis (*Rku*) and the skewness (*Rsk*) will be used to describe the fatigue behavior of hard turned specimens.

Table 23: Average surface roughness parameters.

Roughness parameters	Polished	Hard turning conditions			
	C0	C1	C2	C3	C4
Ra [µm]	0.00±0.00	0.35±0.05	1.10±0.14	0.31±0.08	0.30±0.06
Rt [µm]	0.06±0.01	3.43±0.20	5.55±0.23	3.94±1.74	2.44±0.74
Rq [µm]	0.01±0.00	0.44±0.05	1.26±0.15	0.42±0.14	0.37±0.06
Rv [µm]	0.01±0.00	1.64±0.06	2.16±0.08	1.27±0.31	1.06±0.37
Rsm [µm]	2±0	100±31	151±0	234±144	133±68
Rku	3.11±0.19	3.43±1.00	2.04±0.19	5.96±3.24	3.00±1.00
Rsk	0.24±0.09	-0.36±0.13	0.50±0.11	1.00±1.11	-0.07±0.68

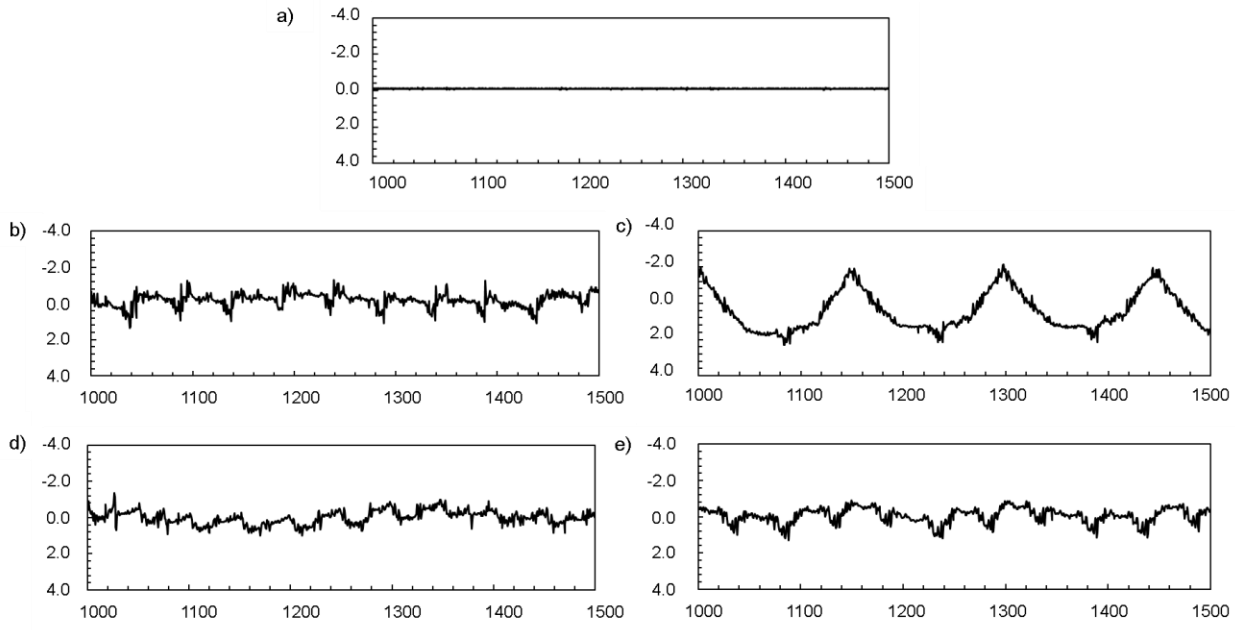

Figure 34: Surface profiles for polished (reference) and hard cutting conditions: a) C0, b) C1, c) C2, d) C3 and e) C4.

5.4.1.2 Residual stresses

In-depth residual stresses were measured in the axial and hoop directions as shown in Figure 35. An average of three surface residual stress measurements was reported for each cutting condition as well as for polished specimens in Table 24. Mechanical polishing did not reduce the level of axial surface residual stresses to zero. In fact, removal of the machined layer (≈ 200 µm) by automated mechanical polishing generated a minimum axial surface residual stress (*ASRS*) of -240

MPa, consistent with the value of -230 MPa reported by Bag et al. [4] in polished 54 HRC 300M. Hard turning generated compressive axial surface residual stress (*ASRS*) for all tested machining conditions, except for condition C2. Machining conditions with low feed rates (C1, C3, and C4) generated similar levels of compressive average *ASRS* (-301 to -438 MPa). Results for conditions C1 and C3 show that increasing cutting speed from 85 to 100 m/min increases compressive *ASRS* by 45 % while shifting *HSRS* from tensile (131 MPa) to compressive (-27 MPa). As shown in Figure 35 where a comparison between axial and hoop residual stresses is made, *HSRS* values are very low compared to *ASRS*. Moreover, the maximum axial residual stress beneath the machined surface is higher and less deep when compared to hoop residual stresses.

Table 24: Average axial (*ASRS*), hoop (*HSRS*) and hydrostatic (σ_h) surface residual stresses calculated based on three measurements per specimen.

Cutting condition	*ASRS* [MPa]	*HSRS* [MPa]	$\boldsymbol{\sigma_h}$ [MPa]
C0	-337 ± 69	NA	-
C1	-301 ± 103	131 ± 62	-57 ± 55
C2	14 ± 86	-50 ± 100	-12 ± 62
C3	-438 ± 78	-27 ± 124	-155 ± 67
C4	-348 ± 82	-35 ± 68	-128 ± 50

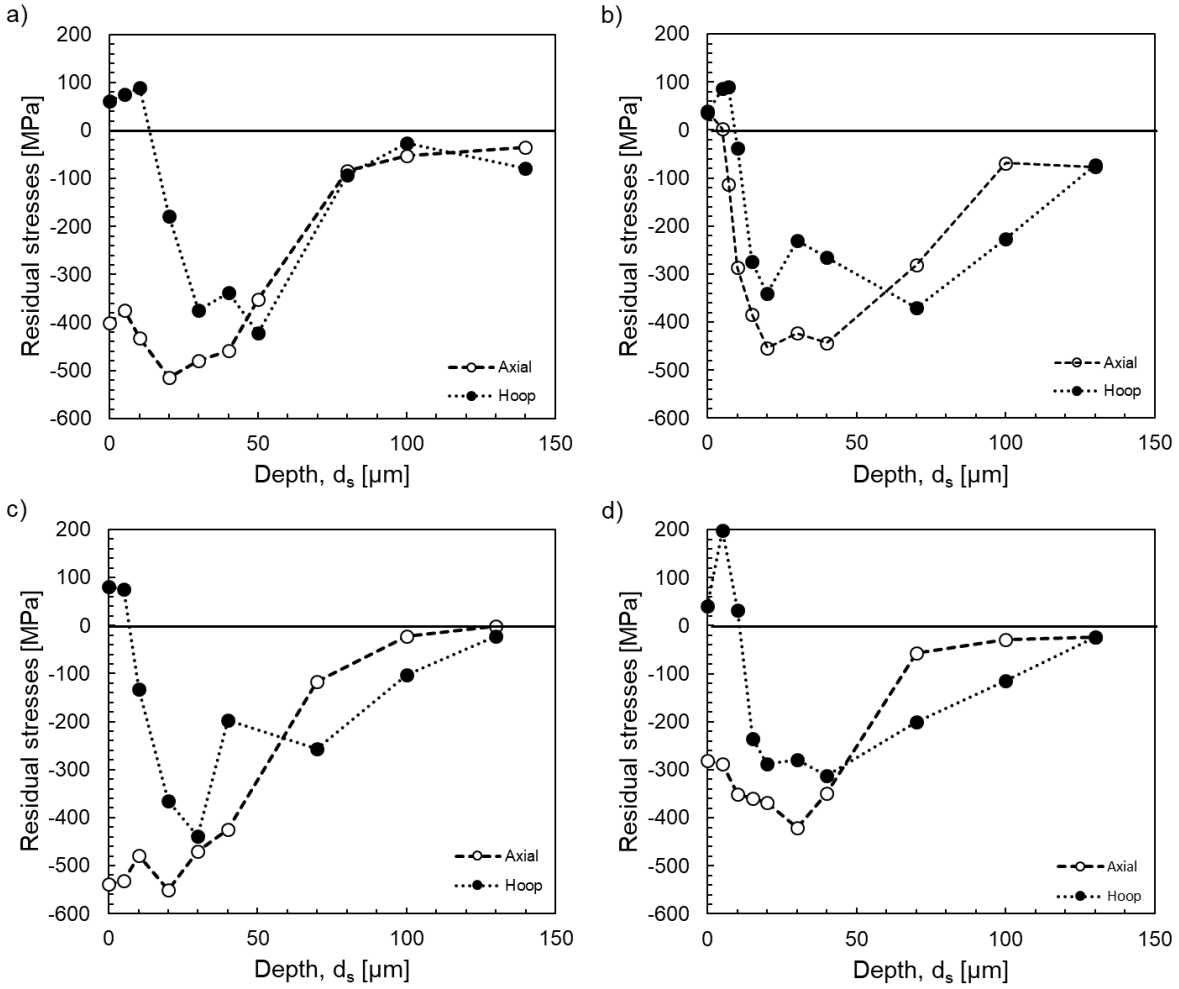

Figure 35:Axial and hoop residual stress profiles for cutting condition a) C1, b) C2, c) C3 and d) C4. The dashed lines are used to connect the measured data points to account for the continuity of the residual stress profile between the measured points.

The hydrostatic residual stress provides additional information on the residual stress state (compressive or tensile). It characterizes the combined influence of axial and hoop residual stresses. The residual stress state at each measured depth is assumed to be an in-plane stress state because (i) the depth of the residual stress profile is negligible with respect to the specimen's diameter and is considered to be the near-surface and (ii) the penetration depth of the X-rays in the radial direction is negligible. Thus, the hydrostatic stress σ_h values were calculated using Equation (37) and presented in Table 24 [84]:

$$\sigma_h = \frac{1}{3}\left(\sigma_{Axial} + \sigma_{hoop}\right) \qquad \text{Equation (37)}$$

Figure 36 shows the hydrostatic residual stress profiles calculated using Equation (37). Condition C4 generated the highest maximum compressive stress beneath the surface while condition C2 generated the largest width of maximum compressive stress.

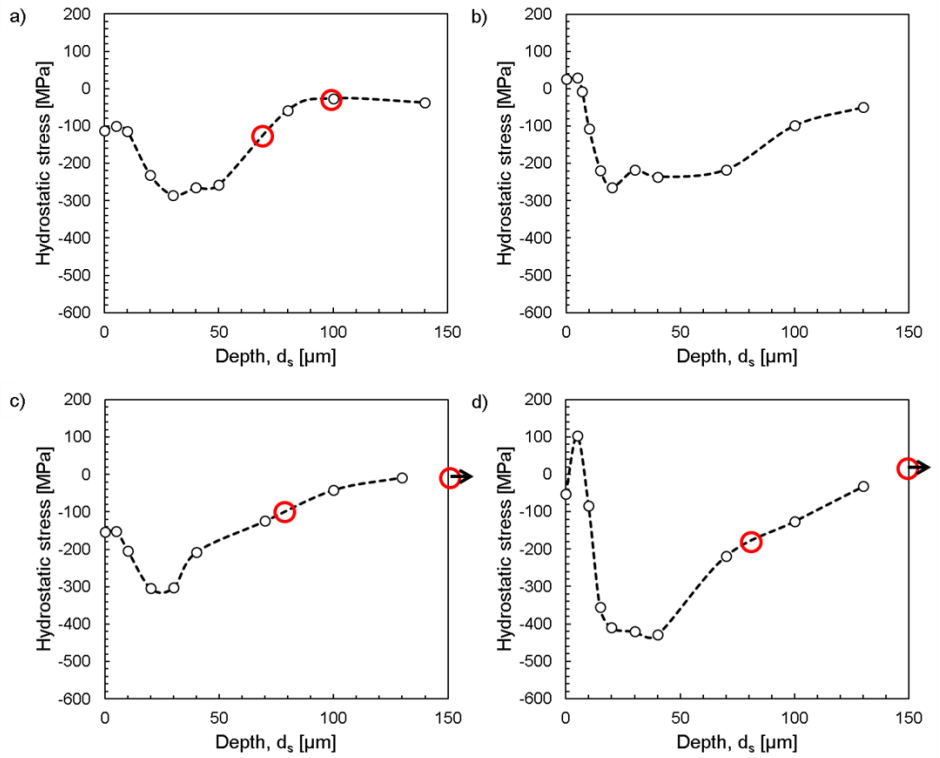

Figure 36: Hydrostatic stress profiles for cutting condition a) C1, b) C2, c) C3 and d) C4. Red circles represent the depth at which subsurface inclusions responsible for crack initiations are located (see section 3.2).

5.4.1.3 Microstructural alterations

The microstructural analysis on cross-sections extracted from different specimens machined under the conditions presented in Table 2 reveals the presence of a white layer on the machined surfaces as well as distorted martensite laths as shown in Figure 37. The white layer thicknesses measured on all studied specimens varied between 0.40 and 0.63 µm and thus, did not vary significantly from

one cutting condition to another. For this reason, only the influence of surface roughness parameters and residual stresses on fatigue life will be discussed in the next section.

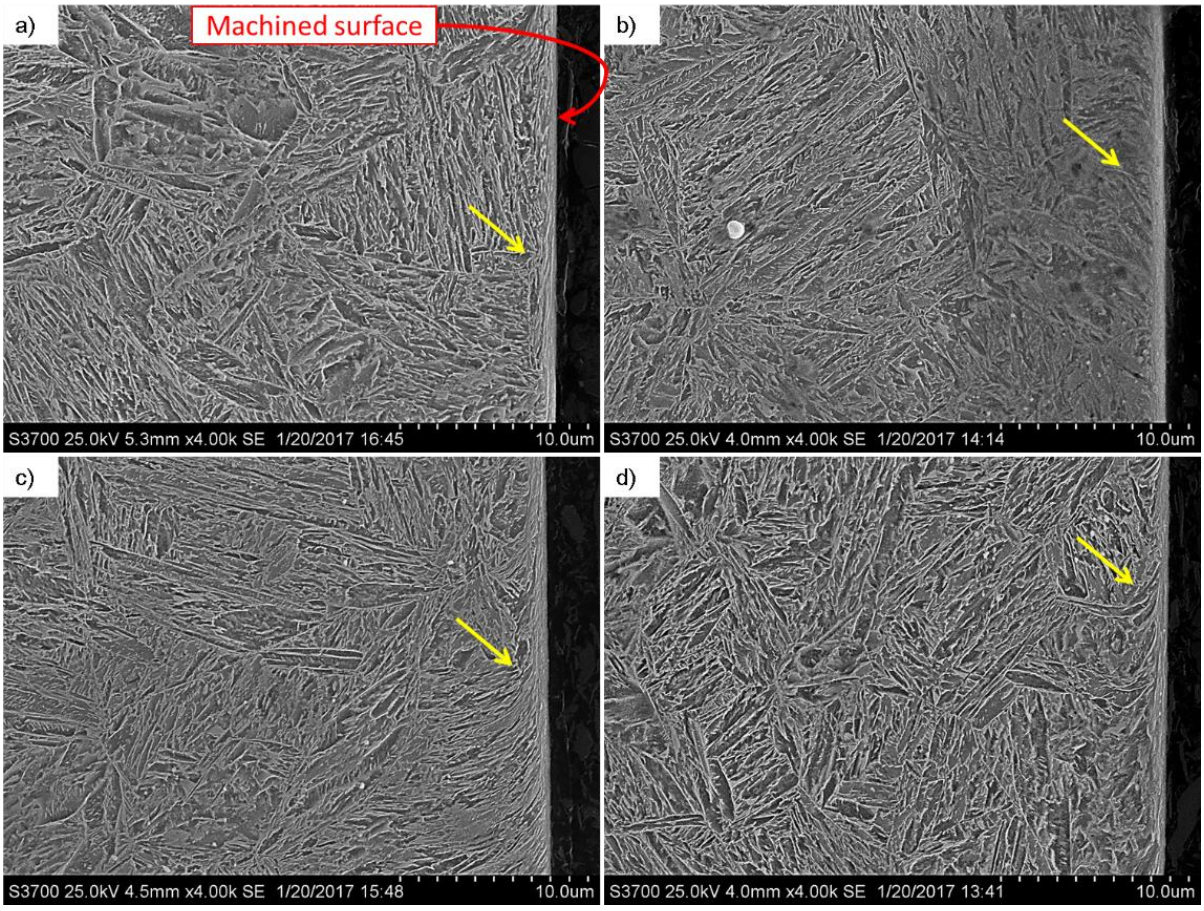

Figure 37: SEM images showing the presence of a white layer thickness on specimens cut in the transverse direction for machining conditions a) C1, b) C2, c) C3 and d) C4. Arrows show the distorted martensite laths.

5.5 Analysis of the fatigue behavior

The analysis of the fatigue behavior of finish hard turned 55 HRC 300M steel was performed according to the following procedure. First, the fatigue life of machined specimens was compared to that of polished specimens (reference condition). Then, to assess the probability of failure in the material, the fatigue life data was subjected to a parametric distribution analysis. Next, a fractographic analysis was carried out to establish the origin of the cracks in order to better describe the influence of the machining process and material defects on crack initiation and fatigue life.

5.5.1 Fatigue life and failure analysis

Fatigue lives obtained for all tested specimens are presented in Figure 38, including for polished specimens (C0, reference). The targeted minimum fatigue life was set to 10^6 cycles to fulfill an industrial requirement for finish hard turned components and was reached by 86% of the total specimen's population. The lower and higher average fatigue life was obtained for cutting conditions C2 ($1.6 \cdot 10^6$ cycles) and C3 ($6.8 \cdot 10^6$ cycles) respectively. The resulting fatigue lives of machined specimens varied between $2.6 \cdot 10^5$ and $9.8 \cdot 10^6$ cycles while the resulting fatigue lives of polished specimens varied between $6.2 \cdot 10^4$ and $8.3 \cdot 10^6$ cycles, showing both that machined specimens can perform better than polished specimens and that polished specimens presented a larger dispersion in fatigue life. This larger dispersion in life data for polished specimens may be explained by analyzing the fractured surfaces as will be discussed later.

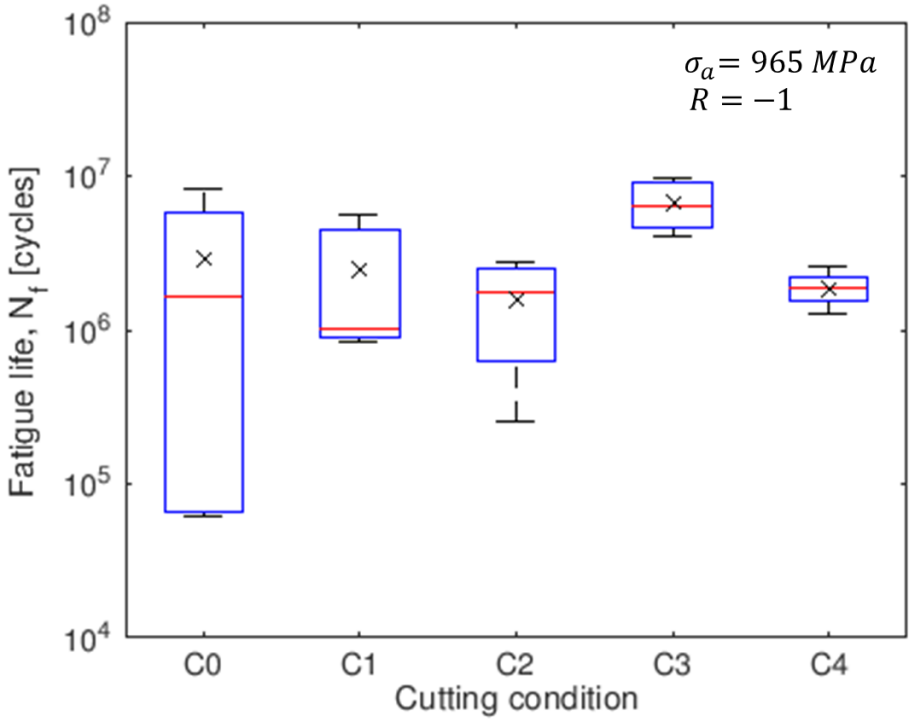

Figure 38: Fatigue life for polished and machined specimens. The extremes of a typical box represent the minimum and maximum values while the top and bottom represent respectively the first and third quartiles. The x sign represents the mean value and the line the median.

A two-parameter Weibull distribution was used to describe the fatigue life data. Such distribution is commonly used to model reliability data and provides reasonably accurate failure predictions [85]. Equation (38) describes the probability density function (PDF) of the Weibull distribution

where α and $\beta \geq 0$ and represent respectively the scale and shape parameters of the distribution function while x refers to fatigue life N_f.

$$f(x) = \frac{\beta}{\alpha}\left(\frac{x}{\alpha}\right)^{\beta-1} e^{-\left(\frac{x}{\alpha}\right)^{\beta}} \quad \text{Equation (38)}$$

The scale parameter α represents the characteristic life corresponding to the number of cycles at which 63.2% of the population is expected to fail. The studied set of data was found to be best defined by a α of $3.24 \cdot 10^6$ and a β of 1.25 which describes a right-skewed distribution for which the data is significantly spread out.

Figure 39 represents the cumulative percent failure (*CPF*) plot showing life data according to cutting conditions. To assess the goodness of the two-parameter Weibull fit, the Anderson-Darling (*AD*) test statistic was used and calculated as follows:

$$AD = -N - \sum_{i=1}^{N} \frac{(2i-1)}{N}\left[\ln F(Y_i) + \ln\left(1 - F(Y_{N+1-i})\right)\right] \quad \text{Equation (39)}$$

where F represents the cumulative distribution function and Y_i the ordered life data. The calculated *AD* value of 0.285 was then compared to a critical *AD* value which depends on the type of distribution, sample size and significance level. For a two-parameter Weibull distribution, a sample size n of 14 and a significance level of 0.05, a critical *AD** value of 0.74 is obtained [86]. Considering that *AD* < *AD**, we can conclude with 95% confidence that a two-parameter Weibull distribution can fit adequately the fatigue life data. Consequently, we can also conclude that although the four cutting conditions studied generated different surface integrity characteristics, particularly C2, those differences did not result in a level of variability in the fatigue data that would necessitate to consider those conditions as non-equivalent in terms of fatigue life and therefore, to fit one Weibull for each one of those conditions.

In summary, results demonstrated that different finishing cutting conditions could generate similar fatigue lives. In fact, a single distribution was effectively used to estimate the probability of failure in 55 HRC 300M specimens hard turned using cutting conditions C1 to C4. However, as shown in Figure 39, the distribution was found to underestimate the probability of failure of the material for

a group of results corresponding to cutting conditions C2 and C4 (see red rectangle). Therefore, the conclusions presented in this section are valid for the small number of specimens tested only and further testing would allow to determine if each cutting condition would be better described by its own distribution.

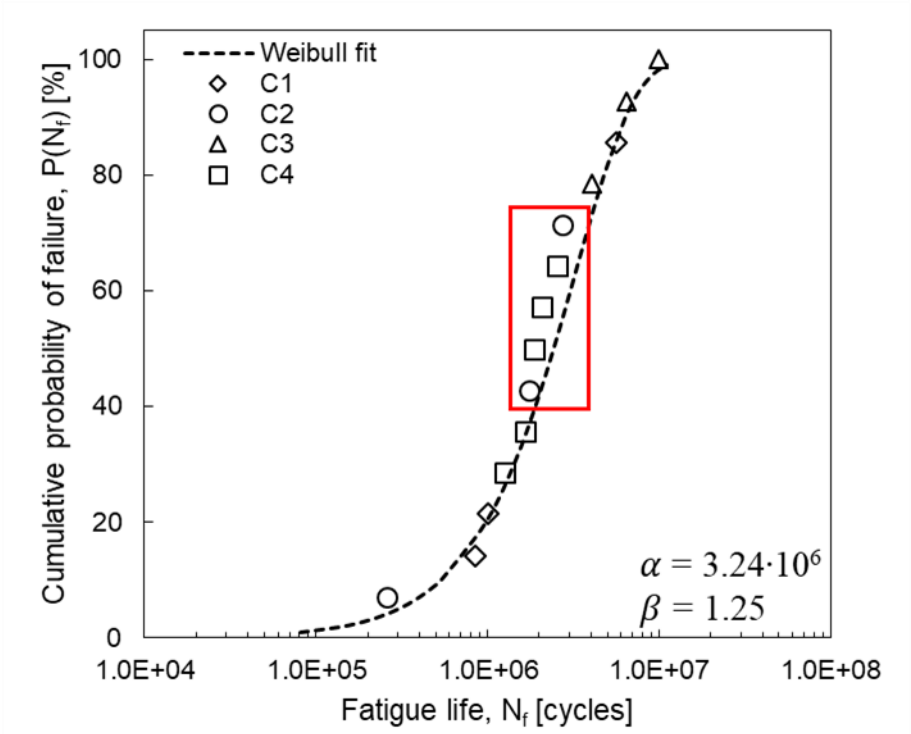

Figure 39: Weibull cumulative percent failure (*CPF*) plot based on the entire set of fatigue data and represented according to cutting conditions.

5.5.2 Fractographic analysis

To better explain the fatigue results obtained, a fractographic analysis was performed on all tested specimens to determine the crack initiation types leading to fatigue failure in hard turned 55 HRC 300M steel and to compare them with those leading to fatigue failure in the reference material (C0).

Five polished specimens with the surface integrity described in sections 3.1.1 and 3.1.2 were tested and their fracture surfaces analyzed as shown in Figure 40. Failures initiated at surface inclusions in three specimens, from a subsurface $Al_2O_3{\cdot}CaO$ inclusion located at 44 μm from the surface in

one specimen (c) and could not be determined in one specimen (b). Further, the inclusions acting as initiation sites were found to have a diameter varying between 15 and 23 μm.

Under the HCF rotating bending loading conditions studied, most failures in polished 300M 55 HRC steel initiated from surface inclusions where the applied stress is maximal. Interestingly, under axial loading conditions, where the applied stress is constant throughout the volume, results published by Bag et al. [4] show that all failures in polished 300M 54 HRC occurred at subsurface inclusions with the exception of one specimen where failure initiated from a surface inclusion. This demonstrates the influence of stress gradient on the position from which crack initiation occurs.

The fractographic analysis on machined specimens revealed that 57% of fatigue failures initiated from a feed mark and 43% from a subsurface Al_2O_3·CaO·MgO inclusion. Figure 41 a) shows a typical feed mark initiation where several short cracks emanating from features in a feed length create a crack front propagating into the material. Figure 41 b) shows a fish-eye of circular shape surrounding an Al_2O_3·CaO·MgO inclusion which has been commonly reported in high strength steels [87], including in shot peened 54 HRC 300M [4]. As reported in Table 25, subsurface inclusions-based initiations were characteristic of inclusions with diameter d_i ranging between 16 and 23 μm and distance from the surface $d_s$varying between 69 and 259 μm. All crack initiations in specimens machined under cutting condition C2 occurred at feed marks while they occurred under both initiation mechanisms in specimens machined under cutting conditions C1, C3 and C4. As reported earlier, surfaces generated by C2 are characterized by tensile *ASRS* and the highest roughness amplitude parameters.

Overall, results for machined specimens show that the shortest and longest life times were the result of a specimen machined under C2 and C3 respectively. In the former case, a fatigue crack initiated at a feed mark while in the latter, a fatigue crack initiated at a subsurface inclusion. However, as stated earlier, 86% of the machined specimens failed at a number of cycles ranging between 10^6-10^7 cycles regardless of the type of crack initiation. Therefore, the two crack initiation types observed in finish hard turned 55HRC 300M steel generated comparable fatigue lives. Also, although a comparison with the reference material allows to conclude that the removal of the machined layer by mechanical polishing causes fatigue cracks to initiate mostly from surface inclusions, results for specimens machined under conditions C1, C3 and C4, show that the presence

of compressive surface residual stresses did not prevent the occurrence of surface crack initiations. Last, as shown in Figure 42 where fatigue life is plotted against crack initiation position, there is more dispersion in fatigue life when crack initiation occurs at the surface than when it occurs in the subsurface layers which may explain the larger dispersion in fatigue life for polished specimens illustrated in Figure 38.

Table 25: Summary of cutting conditions, crack initiation type, surface integrity characteristics and fatigue life for all machined specimens listed in order of increasing fatigue life.

CC	Initiation Type	d_i [µm]	d_s [µm]	*Ra* [µm]	*Rsm* [µm]	*ASRS* [MPa]	N_f [cycles]
C2	Feed mark			1.164	151	95	$2.57 \cdot 10^5$
C1	Subsurface Inclusion	19.7	97	0.358	92	-222	$8.46 \cdot 10^5$
C1	Subsurface Inclusion	23.0	69	0.366	79	-417	$1.01 \cdot 10^6$
C4	Subsurface Inclusion	27.3	259	0.300	126	-466	$1.27 \cdot 10^6$
C4	Feed mark			0.350	143	-306	$1.66 \cdot 10^6$
C2	Feed mark			1.210	151	73	$1.75 \cdot 10^6$
C4	Subsurface Inclusion	19.0	83	0.236	142	-397	$1.87 \cdot 10^6$
C4	Feed mark			0.296	81	-271	$2.08 \cdot 10^6$
C4	Feed mark			0.321	87	-259	$2.55 \cdot 10^6$
C2	Feed mark			0.921	152	-18	$2.75 \cdot 10^6$
C3	Feed mark			0.322	173	-414	$4.07 \cdot 10^6$
C1	Feed mark			0.287	142	-265	$5.64 \cdot 10^6$
C3	Subsurface Inclusion	17.7	77	0.246	406	-526	$6.47 \cdot 10^6$
C3	Subsurface Inclusion	15.8	230	0.259	241	-375	$9.84 \cdot 10^6$

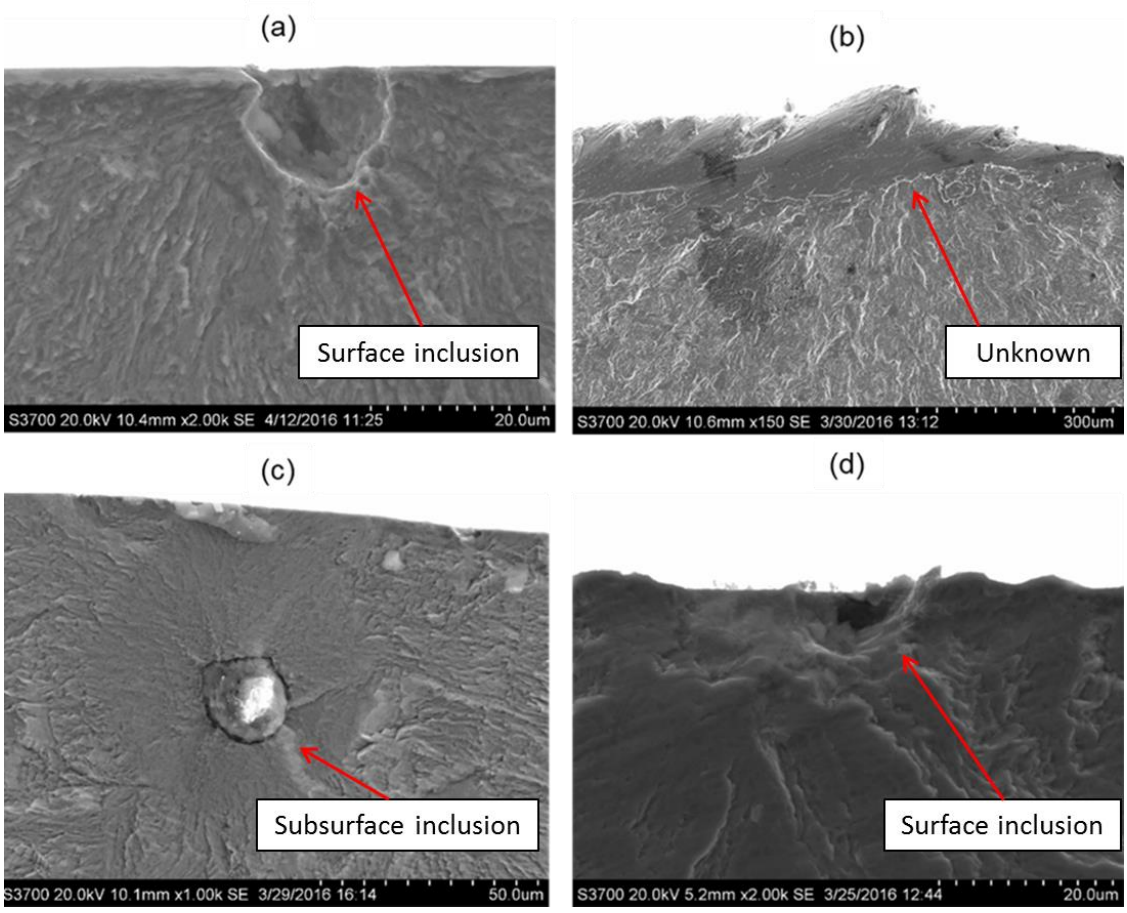

Figure 40: Fatigue crack initiation features observed in polished 55 HRC 300M tested under rotating bending fatigue at σ_a = 965 MPa. In order of increasing fatigue life: (a) $6.8 \cdot 10^4$, (b) $1.9 \cdot 10^5$, (c) $3.2 \cdot 10^6$ and (d) $8.3 \cdot 10^6$ cycles.

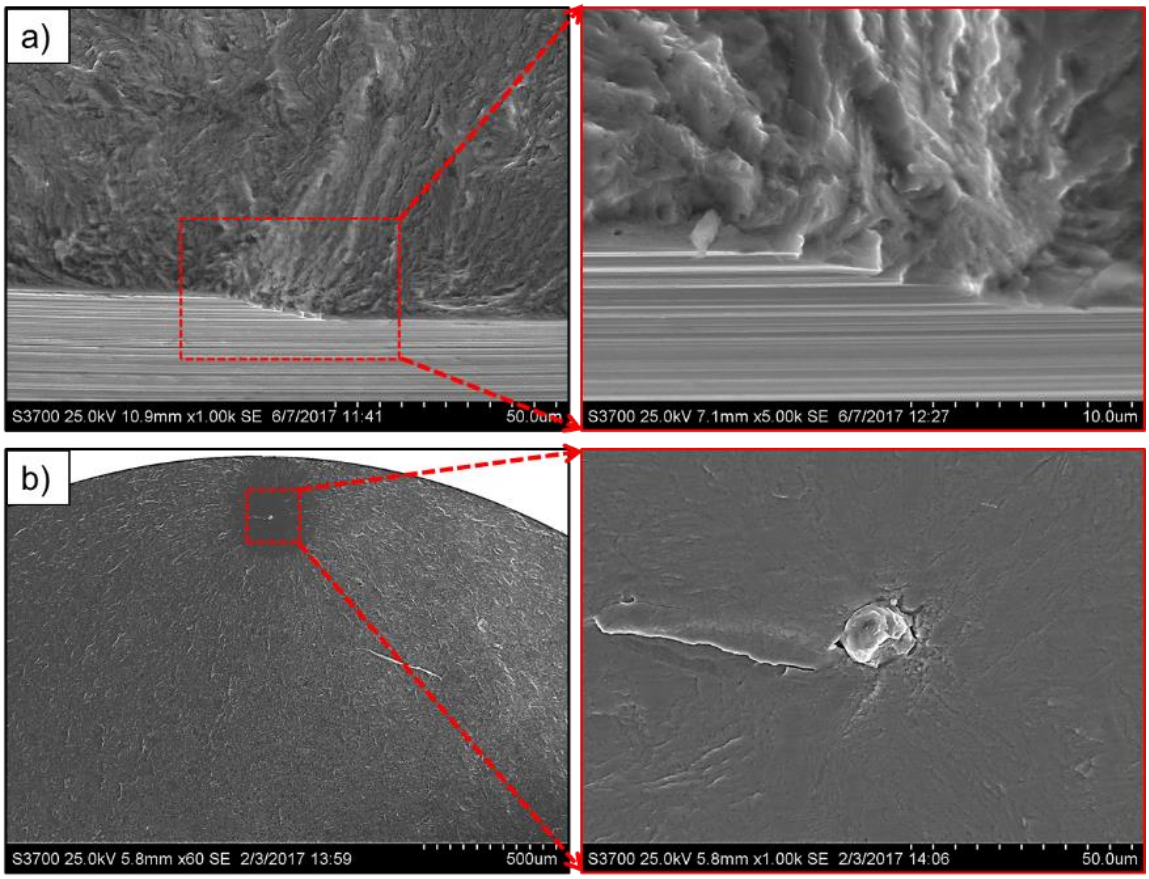

Figure 41: Fatigue crack initiation features observed in hard turned 55 HRC 300M tested under rotating bending fatigue at σ_a = 965 MPa: a) feed mark, $N_f = 1.75 \cdot 10^6$ cycles and b) subsurface inclusion, $N_f = 9.84 \cdot 10^6$ cycles.

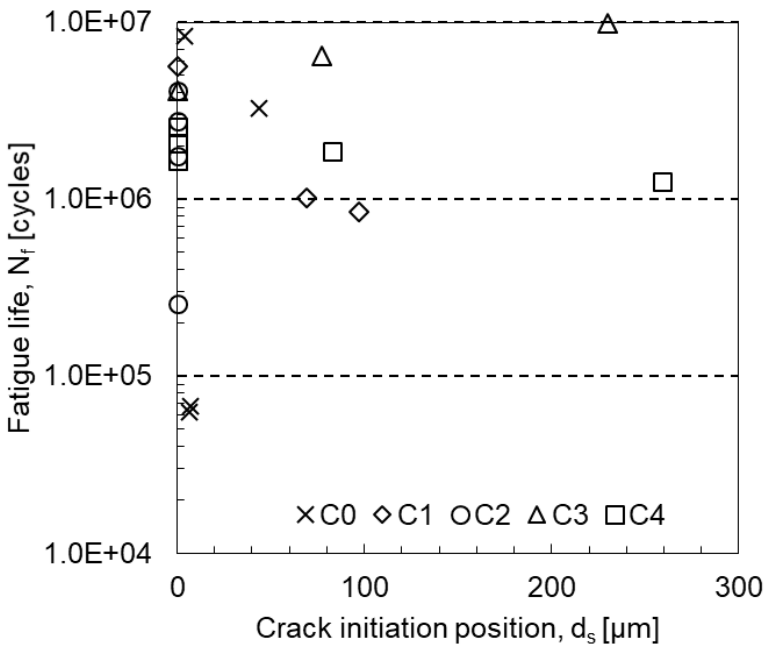

Figure 42: Fatigue life as a function of crack initiation position for each cutting condition studied (C1 to C4) and the reference material (C0). Crack initiations at feed marks are attributed a value d_s = 0 µm while crack initiations at inclusions are attributed a value d_s corresponding to the position of the center of the inclusion with respect to the surface of the specimen.

Since 300M steel (AMS6257E) is vacuum remelted to ensure its cleanliness, it was initially expected that crack initiation would only occur at the surface due to hard turning-induced surface alterations. However, unlike expected, the previous analysis showed that 43% of fatigue failures were caused by cracks originating from material inclusions. Therefore, the following section will only consider the data representative of crack initiation at feed marks to evaluate the influence of surface characteristics on fatigue life and determine if any parameter can explain better the variability in the data.

5.5.3 Influence of surface integrity on fatigue life

Figure 43 shows the influence of all surface integrity parameters characterized earlier on fatigue life. Results show a large dispersion in the data which makes difficult any attempt to assess the existence of trends between surface roughness parameters and/or residual stresses and fatigue life. Therefore, to determine which characteristics among surface integrity features are most relevant to

fatigue life, a multivariate analysis based on the nonparametric Spearman's rank-order correlation coefficient was performed.

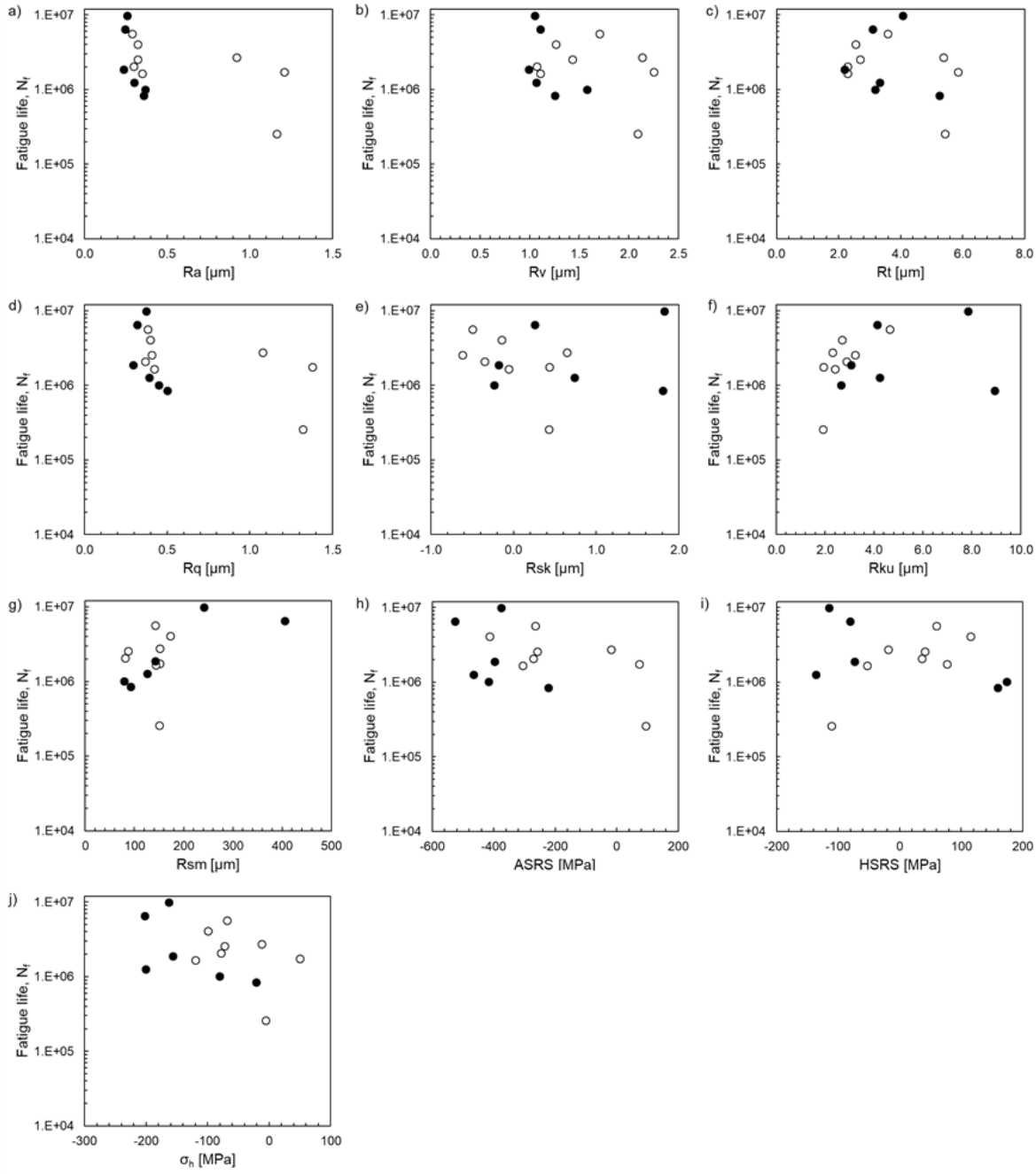

Figure 43: Influence of surface roughness parameters, surface residual stresses on fatigue life: a) *Ra*, b) *Rv*, c) *Rt*, d) *Rq*, e) *Rsk*, f) *Rku*, g) *Rsm*, h) *ASRS* and i) *HSRS* and j) σ_h. Empty circles represent crack initiation at feed marks while filled circles represent crack initiation at subsurface inclusions.

The Spearman's correlation coefficient measures the strength of the monotonic association between two variables. Unlike the Pearson's correlation coefficient, it does not assume linearity of the relationship between two variables [88] and it is robust against the presence of outliers [89]. Its value ranges between ± 1, a value of 0 corresponding to no correlation, and its sign provides the direction of the relationship. For instance, the coefficient is negative if one variable tends to increase while the other decreases. For two variables *x* and *y*, the Spearman correlation coefficient ρ is determined by calculating the Pearson correlation coefficient between the ranks of two given variables:

$$\rho = \frac{\sum_{i=1}^{n}(X_i - \bar{X})(Y_i - \bar{Y})}{(n-1)S_X S_Y} \qquad \text{Equation (40)}$$

where $\bar{X}$ and $\bar{Y}$ represent the sample mean rank of the first and second variable, S_X and S_Y their standard deviation and *n* the number of observations. The Spearman correlation coefficients are listed in Table 26 along with their 95% confidence interval and corresponding p-values. The relationship between two variables is considered to be statistically significant if the correspond p-value is below or equal to the 0.05 alpha level.

Table 26: Spearman coefficient for each parameter with respect to fatigue life N_f.

Parameter	Spearman coefficient (p-value)	95% confidence interval
Rv	-0.19 (0.52)	(-0.66, 0.39)
Rt	-0.19 (0.45)	(-0.66, 0.39)
Ra	**-0.59 (0.03)**	(-0.87, -0.04)
Rq	**-0.56 (0.04)**	(-0.85, 0.00)
Rsk	-0.13 (0.66)	(-0.62, 0.43)
Rku	0.34 (0.23)	(-0.25, 0.75)
Rsm	**0.54 (0.05)**	(-0.03, 0.85)
ASRS	-0.28 (0.33)	(-0.71, 0.31)
HSRS	-0.15 (0.61)	(-0.63, 0.42)
σ_h	-0.35 (0.22)	(-0.75, 0.24)

The interpretation of the Spearman correlation coefficients must not be done without the 95% confidence intervals reported because each interval contains the true population's correlation coefficient for the parameter evaluated at the confidence level chosen. The parameters showing a statistically significant association with fatigue life at a 95% confidence interval are surface

roughness parameters *Ra*, *Rq* and *Rsm*. The corresponding correlation coefficients calculated are respectively -0.59, -0.56 and 0.54 and thus, while fatigue life decreases with increasing *Ra* and *Rq*, it increases with increasing *Rsm*. This result shows that amplitude and spacing surface roughness parameters have an opposite effect on fatigue life although not all amplitude parameters were found to have a statistically significant association with fatigue life. Further, the confidence intervals reported in Table 26 confirm the direction of the trends established by the small specimen size evaluated. However, the wide range of values representative of the 95% confidence intervals shows that this analysis do not allow concluding on the strength of the associations between *Ra*/*Rq*/*Rsm* and N_f. For instance, a p-value of 0.03 indicates that there is a strong relationship between *Ra* and N_f. However, at a 95% confidence level, the calculated Spearman coefficient can lie anywhere between -0.87 and -0.04 showing that we cannot conclude on the strength of the relationship between *Ra* and N_f with such a confidence level.

In summary, results from the Spearman correlation analysis allow to conclude on the existence of a statistically significant correlation between surface roughness parameters *Ra*, *Rq*, *Rsm* and fatigue life at a 95% confidence interval. However, although the direction of the relationships between the different variables was established, no conclusions could be drawn on their strength.

5.5.4 Influence of the maximum stress intensity factor K_{max} on fatigue life

In a final attempt to identify a parameter that unifies fatigue results generated with varying surface integrity characteristics, the maximum stress intensity factor K_{max} was calculated for all tested specimens using equations (41) and (42) [38] for respectively surface feed mark and subsurface inclusions initiations where $K_{max,surf}$, $K_{max,sub}$, σ_{net}, $\sqrt{area_R}$ and $\sqrt{area_{inc}}$ represent respectively the maximum surface intensity factor, maximum subsurface intensity factor, net applied stress, Murakami's equivalent square root area function for surface roughness and Murakami's square root area function for an inclusion.

$$K_{max,surf} = 0.65 \cdot \sigma_{net} \cdot \sqrt{\pi\sqrt{area_R}} \qquad \text{Equation (41)}$$

$$K_{max,sub} = 0.50 \cdot \sigma_{net} \cdot \sqrt{\pi\sqrt{area_{inc}}} \qquad \text{Equation (42)}$$

The net stress represents the net applied stress at the crack initiation site position and can be calculated using equations (43) and (44) for rotating bending loading conditions where $\sigma_{app}(d_s)$, $\sigma_{RS}(d_s)$ and *r* represent respectively the applied stress at the position of the crack initiation site, the axial residual stress at the position of the crack initiation site and the specimen's radius.

$$\sigma_{net} = \sigma_{app}(d_s) + \sigma_{RS}(d_s) \quad \text{Equation (43)}$$

$$\sigma_{app}(d_s) = 965\left(1 - \frac{d_s}{r}\right) \quad \text{Equation (44)}$$

Murakami's equivalent square root area function for surface roughness is represented by Equation (45) [90] where *a* and *b* represent surface roughness parameters *Rt* and *Rsm* respectively.

$$\sqrt{area_R} = 2b \cdot \left[2.97\left(\frac{a}{2b}\right) - 3.51\left(\frac{a}{2b}\right)^2 - 9.74\left(\frac{a}{2b}\right)^3\right] \quad \text{Equation (45)}$$

Because the Spearman's analysis demonstrated the absence of a statistically significant correlation between *Rt* and N_f, the calculation of $\sqrt{area_R}$ was performed using *Ra* for which a statistically significant correlation was found with N_f. This approach is in line with results reported in Itoga et al. [90] where fatigue limits for varying surface roughness levels were calculated using Murakami's equation based on $\sqrt{area_R}$. The authors used both *Ra* and *Rt* to calculate $\sqrt{area_R}$ and showed that the use of *Ra* resulted in better fatigue limit predictions. They suggested that a plausible explanation to this result is the overestimation of $\sqrt{area_R}$ with *Rt* because the value calculated represents the area of a surface roughness profile with periodic cracks of depths equal to *Rt*. Considering that a real surface roughness profile is constituted of randomly distributed features with depths mostly smaller than *Rt*, it can be concluded that *Ra* provides a better estimation of $\sqrt{area_R}$ [90].

The highest K_{max} values (3.04 to 3.89 MPa·m^{½}) were obtained for crack initiations at subsurface inclusions (*SBI*). Those inclusions are characterized with a size $\sqrt{area_{inc}}$ varying between 15.1 and 25.4 µm^{½} and a position d_s varying between 69 and 259 µm. Figure 44 a) shows that the calculated $K_{max,surf}$ values for crack initiations at feed marks were found to be lower than all the $K_{max,sub}$ values obtained. Since the reverse trend is expected, this result implies that either no big enough inclusion was found within a relatively small distance d_s (maximum d_s observed = 259 µm)

in specimens where failure was caused by a crack originating from a feed mark feature, either the factor 0.65 in equation (41) underestimates the severity of a surface defect such as surface roughness. For comparison purposes, $K_{max,surf}$ was also calculated using $a = Rt$ as shown in Figure 44 b). In this case, the values calculated show that cutting condition C2, which is the only condition with tensile axial surface residual stresses, are greater than the obtained $K_{max,sub}$ values. This result demonstrate that either (i) equation (45) underestimates the $\sqrt{area_R}$ values characterizing a surface roughness profile with non-uniform machining marks as reported by Bag et al. [91], either (ii) the factor 0.65 in equation (41) underestimates the severity of a surface defect such as surface roughness, either both (i) and (ii). Since the threshold for crack propagation at $R = -1$ is in the range of 4.2 MPa·m^{½}, as reported in Bag et al. [91], (i) calculated $K_{max,sub}$ values should correspond to the threshold, considering that material inclusions are the limiting factor for crack propagation when no more severe defect can be found at the surface, and (ii) $K_{max,surf}$ values should fall above the threshold for crack propagation. This supports the hypothesis that equation (41) underestimates the real K_{max} values.

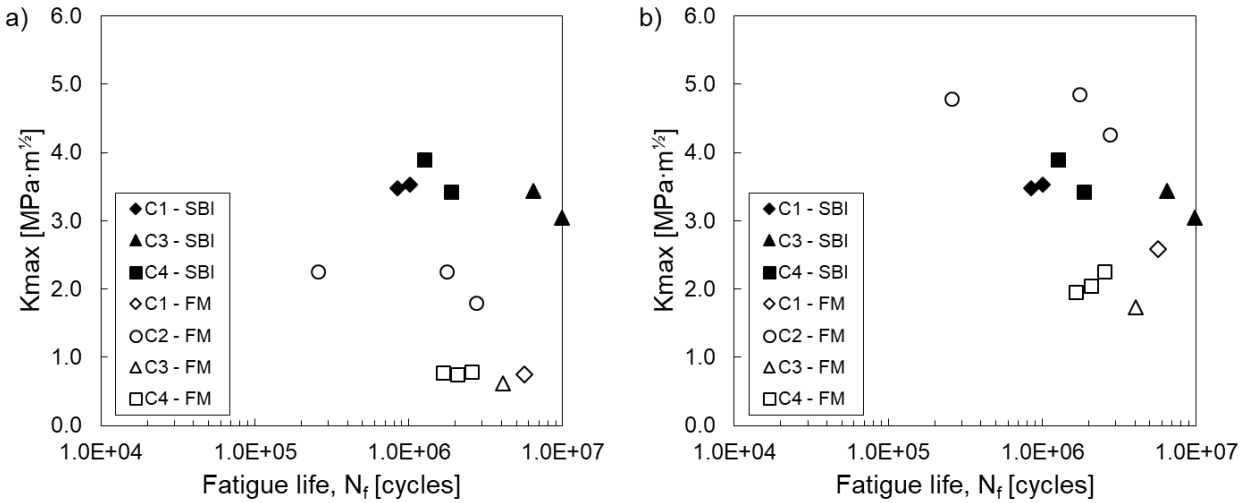

Figure 44: Influence of the maximum stress intensity factor K_{max} on fatigue life calculated using a) $a = Ra$ and b) $a = Rt$. SBI and FM represent subsurface inclusions and feed mark crack initiations respectively.

In summary, K_{max} was used to gather together fatigue data resulting from the propagation of cracks from two different features. Both defect size and residual stresses were taken into account in the calculation of this factor. Results show that cutting conditions C1, C3 and C4 generated surfaces with similar K_{max} levels while C2 generated surfaces with higher severity. Considering that a

fatigue crack should only propagate from a material inclusion if there is no surface defect with higher severity, results either demonstrate the limitation of equation (41) in characterizing accurately K_{max} values for machined surfaces, either demonstrate that the propagation of short cracks cannot be described directly using a K_{max} value. Results depicted in Figure 44 also demonstrate that finish cutting conditions C1, C3 and C4 cannot be optimized further for fatigue life for the material studied considering that they all generate failures from subsurface inclusions. Thus, if the need be, efforts to optimize fatigue life should be invested into making the material cleaner prior to any attempt in optimizing further the machining process.

5.6 Conclusions

The main objective of the current study was to better understand the fatigue behavior of finish hard turned 55 HRC 300M steel. A total of four cutting conditions were selected to generate a range of surface characteristics representative of production finish hard turning cutting conditions. Specimens were tested under rotating bending fatigue under a stress amplitude of 965 MPa and a target of 10^6 cycles. Results from the analysis of the fatigue life and fractographic data allowed drawing the following conclusions:

- A single distribution can be used to estimate the probability of failure in finish hard turned 55 HRC 300M steel. This demonstrates that although cutting condition C2 generated surface integrity characteristics that are significantly different (tensile *ASRS* and higher *Ra*) when compared to cutting conditions C1, C3 and C4 (compressive *ASRS*, lower *Ra*), resulting fatigue lives do not reflect this difference.
- The removal of the machined layer by mechanical polishing causes fatigue cracks to initiate mostly from surface inclusions in polished specimens resulting in more dispersed fatigue lives.

- No simple statistical model was able to describe the relationship between surface integrity characteristics generated by finish hard turning cutting conditions and fatigue life in samples where cracks originated from surface feed marks. However, a Spearman correlation analysis demonstrates the existence of a statistically significant correlation between surface roughness parameters *Ra*, *Rq*, *Rsm* and fatigue life with 95% confidence.
- Finish cutting conditions C1, C3 and C4 cannot be optimized further for fatigue life because results demonstrate that fatigue cracks in specimens machined under those conditions propagated from subsurface inclusions which is the material's limiting factor.
- The maximum surface intensity factor K_{max} was not effective in unifying the fatigue life data resulting from two different crack initiation mechanisms. $K_{max,surf}$ values calculated using Murakami's equation demonstrated that the equation underestimates the severity of a surface defect such as surface roughness.

5.7 Acknowledgements

This work was supported by the Consortium for Research and Innovation in Aerospace in Quebec (CRIAQ), MITACS, the Natural Sciences and Engineering Research Council (NSERC), Héroux-Devtek and Pratt & Whitney Canada. The authors would like to acknowledge the technical assistance received from Cristina del Vasto (Héroux-Devtek) and Nicolas Brodusch (McGill University) during this project.

5.8 References

1. Tönshoff, H.K., C. Arendt, and R.B. Amor, *Cutting of Hardened Steel.* CIRP Annals, 2000. **49**(2): p. 547-566.
2. Dickinson, G. *The Influence of Machining on the Performance of Ultra High Strength Steels*. in *ASME 1970 International Gas Turbine Conference and Products Show*. 1970. American Society of Mechanical Engineers.
3. Pistochini, T.E. and M.R. Hill, *Effect of laser peening on fatigue performance in 300M steel.* Fatigue and Fracture of Engineering Materials and Structures, 2011. **34**(7): p. 521-533.

4. Hill, M.R., T.E. Pistochini, and A.T. DeWald, *Fatigue Performance of Laser Peened Materials.* 2005(41928): p. 203-207.
5. Bag, A., et al., *Statistical analysis of high cycle fatigue life and inclusion size distribution in shot peened 300M steel.* International Journal of Fatigue, 2019. **118**: p. 126-138.
6. Siqueira, C.P., et al., *Effects of nitriding and shot peening treatments and stress concentration on the fatigue strength of AISI 4340 steel.* SAE Technical Papers, 2001.
7. Matsumoto, Y., et al., *Effect of machining processes on the fatigue strength of hardened AISI 4340 steel.* Journal of Manufacturing Science and Engineering, Transactions of the ASME, 1991. **113**(2): p. 154-159.
8. Buddy Damm, E. *4340 Steel fatigue initiation and performance in rotating bending fatigue as a function of surface finish and melt practice*. in *Materials Science and Technology*. 2005.
9. Petropoulos, G.P., C.N. Pandazaras, and J.P. Davim, *Surface Texture Characterization and Evaluation Related to Machining*, in *Surface Integrity in Machining*, J.P. Davim, Editor. 2010, Springer London: London. p. 37-66.
10. Varela, P.I., C.S. Rakurty, and A.K. Balaji. *Surface integrity in hard machining of 300M Steel: Effect of cutting-edge geometry on machining induced residual stresses*. in *Procedia CIRP*. 2014.
11. Petropoulos, G.P., et al., *Multi-parameter identification and control of turned surface textures.* The International Journal of Advanced Manufacturing Technology, 2006. **29**(1): p. 118-128.
12. Stout, K., *How smooth os smooth? Surface measurements and their relevance in manufacturing.* Production Engineer, 1980. **59**(5): p. 17-22.
13. Gadelmawla, E.S., et al., *Roughness parameters.* Journal of Materials Processing Technology, 2002. **123**(1): p. 133-145.
14. Sakin, R. and İ. Ay, *Statistical analysis of bending fatigue life data using Weibull distribution in glass-fiber reinforced polyester composites.* Materials & Design, 2008. **29**(6): p. 1170-1181.
15. Murakami, Y. and H. Usuki, *Quantitative evaluation of effects of non-metallic inclusions on fatigue strength of high strength steels. II: Fatigue limit evaluation based on statistics for extreme values of inclusion size.* International Journal of Fatigue, 1989. **11**(5): p. 299-307.
16. MURAKAMI, Y., N.N. YOKOYAMA, and J. NAGATA, *Mechanism of fatigue failure in ultralong life regime.* Fatigue & Fracture of Engineering Materials & Structures, 2002. **25**(8-9): p. 735-746.
17. Itoga, H., et al., *Effect of surface roughness on step-wise S–N characteristics in high strength steel.* International Journal of Fatigue, 2003. **25**(5): p. 379-385.
18. Yang, Z.G., et al., *On the critical inclusion size of high strength steels under ultra-high cycle fatigue.* Materials Science and Engineering: A, 2006. **427**(1): p. 167-174.
19. Nakajima, M., et al., *Effect of loading condition on very high cycle fatigue behavior in a high strength steel.* International Journal of Fatigue, 2010. **32**(2): p. 475-480.

CHAPTER 6 GENERAL DISCUSSION

This section first summarizes results presented in chapters 4 and 5. Then, the influence of hard turning cutting parameters on the surface integrity of 55 HRC 300M steel is compared with results published in the literature. Finally, the fatigue behavior of finished hard turned 55 HRC 300M steel is discussed with respect to fatigue life and crack initiation type.

6.1 Influence of Hard Turning Cutting Parameters on Surface Integrity

This section will answer the following two research questions: (i) What is the influence of finishing hard turning conditions on the surface integrity of hardened 300M and (ii) What finish hard turning cutting conditions are the most effective in minimizing simultaneously surface roughness and tensile residual stresses.

As shown in this table, a few combinations of cutting parameters generated similar surface characteristics. For example, for varying *T*, *V*, *f* and *D*, cutting conditions T1, T4 and T8 generated an *Ra* value of 0.26 ± 0.01 µm and an *ASRS* value of 178 ± 22 MPa. However as illustrated in Figure 45, their microgeometries are different which can be captured by other surface characteristics, namely the skewness *Rsk* and kurtosis *Rku* surface roughness parameters as reported in chapter 4. Therefore, the use of surface characteristic parameters that are less conventional is essential in understanding the influence of cutting parameters on the surface integrity of a part and the possibly resulting effect on its performance.

Table 27 provides a summary of selected surface integrity characteristics for all cutting conditions studied. Overall, three different cutting tool materials were used: carbide, ceramic and PCBN. Cutting parameters *V*, *f*, and *D* ranged between 50 – 100 m/min, 0.051 – 0.203 mm/rev and 0.245 – 0.762 mm respectively while resulting surface characteristics *Ra*, *Rv*, *ASRS* and *HSRS* ranged between 0.26 – 1.62 μm, 0.77 – 2.80 μm, -953 – 26 MPa and -384 – 326 MPa respectively. As shown in this table, a few combinations of cutting parameters generated similar surface characteristics. For example, for varying *T*, *V*, *f* and *D*, cutting conditions T1, T4 and T8 generated an *Ra* value of 0.26 ± 0.01 μm and an *ASRS* value of 178 ± 22 MPa. However as illustrated in Figure 45, their microgeometries are different which can be captured by other surface characteristics, namely the skewness *Rsk* and kurtosis *Rku* surface roughness parameters as reported in chapter 4. Therefore, the use of surface characteristic parameters that are less conventional is essential in understanding the influence of cutting parameters on the surface integrity of a part and the possibly resulting effect on its performance.

Table 27 : Summary of selected surface integrity characteristics for all cutting conditions studied. Bold values represent minimum and maximum values.

Cutting condition	*T*	*V* [m/min]	*f* [mm/rev]	*D* [mm]	*Ra* [µm]	*Rv* [µm]	*ASRS* [MPa]	*HSRS* [MPa]
T1	Carbide	50	0.051	0.254	0.28	1.13	-199	54
T2	Carbide	75	0.127	0.508	0.69	1.63	-234	-219
T3	Carbide	100	0.203	0.762	1.58	**2.80**	-78	-325
T4	Ceramic	50	0.127	0.762	**0.26**	**0.77**	-179	-145
T5	Ceramic	75	0.203	0.254	0.44	0.98	**26**	203
T6	Ceramic	100	0.051	0.508	0.40	1.11	-836	-252
T7	PCBN	50	0.203	0.508	**1.62**	2.63	-121	**-384**
T8	PCBN	75	0.051	0.762	0.27	0.89	-155	38
T9	PCBN	100	0.127	0.254	0.62	1.04	-154	-109
T10	Ceramic	75	0.051	0.254	0.38	1.14	-938	-298
T11	Carbide	100	0.127	0.508	0.27	0.78	84	**326**
T12	Ceramic	50	0.051	0.762	0.35	1.13	**-953**	-380
T13	Ceramic	75	0.051	0.254	0.38	1.14	-938	-298
C1	Carbide	85	0.053	0.490	0.35	1.64	-301	131
C2	Carbide	55	0.152	0.245	1.10	2.16	14	-50
C3	Carbide	100	0.053	0.490	0.31	1.27	-438	-27
C4	Carbide	69	0.053	0.319	0.30	1.06	-348	-35

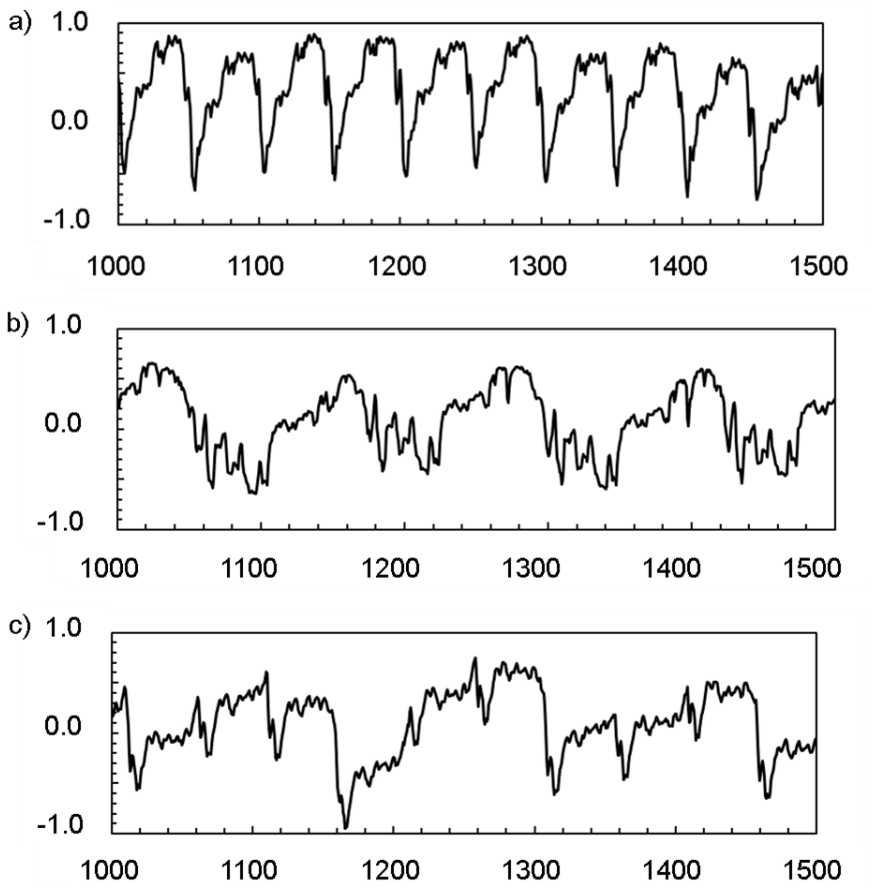

Figure 45: Varying microgeometry for varying cutting parameters but identical *Ra* and *ASRS* characteristics: a), T1 b) T4 and c) T8. Units given in micrometers where X and Y axes represent the length and height of a profile respectively.

Because most of the cutting conditions combinations (*T, f, V, D*) studied as part of this work vary from the ones reported in the literature for both 4340 and 300M, it is difficult to make comparisons on a one-to-one basis. However, general comparisons can be made using Table 5 and Table 6 where the minimum and maximum *Ra, ASRS* and *HSRS* values published in the literature are reported along with the cutting conditions used to generate those surface characteristics. First, all studies reported a minimum roughness *Ra* value for their lowest feed rate tested, regardless of *T, V,* and *D*. This is in agreement with our results for the conditions where a carbide or PCBN tool was used (T1, T8, C3 and C4). Second, Table 6 shows that lower feed rates lead to more compressive *ASRS* which is also in agreement with our results as shown in As shown in this table, a few combinations of cutting parameters generated similar surface characteristics. For example, for varying *T, V, f* and

D, cutting conditions T1, T4 and T8 generated an *Ra* value of 0.26 ± 0.01 µm and an *ASRS* value of 178 ± 22 MPa. However as illustrated in Figure 45, their microgeometries are different which can be captured by other surface characteristics, namely the skewness *Rsk* and kurtosis *Rku* surface roughness parameters as reported in chapter 4. Therefore, the use of surface characteristic parameters that are less conventional is essential in understanding the influence of cutting parameters on the surface integrity of a part and the possibly resulting effect on its performance.

Table 27. Therefore, a low feed rate generates low surface roughness values and highly compressive *ASRS* which is in agreement with the literature as shown in Table 5 and Table 6.

As reported in chapter 4, the factor with the highest contribution to surface roughness is feed rate. This is in agreement with the literature on 4340 steel where the influence of a single cutting tool material on surface roughness was evaluated [21-23, 27]. In order of decreasing contribution, Table 14 shows that following feed rate, the factors with the highest contribution to surface roughness are cutting tool material, depth of cut and cutting speed. This shows that the selection of a cutting tool material is important in generating desired level of surface roughness as reported by Çaydaş et al. [19]. Table 14 also shows the contribution ranking for other surface characteristics evaluated, namely *ASRS*, *HSRS* and *WL*. The factors with the highest contribution to *ASRS*, *HSRS* and *WL* are *f*, *D* and *V* respectively. This shows the varying response of surface characteristics to cutting parameters and justifies the existence of one optimum per surface characteristic optimized as shown in Table 15. However, considering the complexity of the hard turning process, it is usually desired to optimize several responses at a time which cannot be achieved using a single-objective optimization approach. Therefore, the use of a multi-objective optimization methodology becomes necessary as explained in chapter 4. Different methods can be used but the most appropriate approach in an industrial perspective, must respond to a series of criteria including being time-, cost- and user- friendly as well as generating accurate results. A survey from the literature showed that a hybrid Taguchi-GRA-PCA method was an appropriate method for solving a hard turning optimization problem which has been confirmed by the results presented in Table 19 from chapter 4. Results showed that a combination of low surface roughness (*Ra, Rv, Rz*) and highly compressive *ASRS* and *HSRS* were obtained using a ceramic tool, a f = 0.051 mm/rev, a V = 50 m/min and a D = 0.762 mm. In fact, a 50% reduction in *Ra* was achieved combined with a 307% increase in compressive *ASRS*.

Residual stress profiles obtained for conditions C1 to C4 were presented in chapter 5. The maximum experimental compressive residual stress and the depth at which it is located are reported in Table 28 for both axial and hoop residual stresses. The maximum axial compressive residual stress is located between 20 and 30 µm beneath the surface and its magnitude varies between -550 and -421 MPa whereas the maximum hoop compressive residual stress is located at a depth ranging between 20 and 70 µm and its magnitude varies between -438 and -288 MPa. The maximum

compressive stress in both directions was obtained for condition C4 for which the feed rate is the lowest (*f* = 0.053 mm/rev) and the cutting speed the highest (*V* = 100 m/min). This is in agreement with results obtained for 4340 showing that minimum tensile *ASRS* were obtained for the condition with the lowest *f* and highest *V* as shown in Table 6. Finally, as mentioned in chapter 2, Zhang et al. [1] demonstrated that either increasing *f, V* or *D* resulted in an increase in the maximum compressive residual stress below the surface when keeping other parameters constant. This could explain the slight increase in max *ARS* from C1 to C4 where for constant *f* and *D, V* was increased by 15 m/min.

Table 28 : Magnitude and position of the axial/hoop maximum compressive residual stress.

Cutting condition	max. *ARS* [MPa]	Depth [µm]	Max. *HRS* [MPa]	Depth [µm]
C1	-515	20	-422	50
C2	-454	20	-370	70
C3	-550	20	-438	30
C4	-421	30	-288	20

In summary, results generated as part of this study demonstrated the complexity of the interactions between the various parameters studied which influences the way surface integrity is altered. Nevertheless, it is clear that as previously reported in the literature, feed rate plays a predominant role for surface roughness and *ASRS* in hardened 300M although it is not the most contributing factor to *HSRS* and *WL*. Results also demonstrated that hard turning cutting parameters can be optimized to minimize simultaneously surface roughness and tensile residual stresses. In fact, the use of a ceramic tool combined with *f, V* and *D* values of 0.051 mm/rev, 50 m/min and 0.762 mm, resulted in *Ra, ASRS* and *HSRS* values of 0.35 µm, -953 MPa and -380 MPa respectively.

6.2 Fatigue Behavior of Finish Hard Turned 300M Steel

This section will answer the following two research questions: (i) Is there a relationship between surface integrity characteristics and fatigue life under rotating bending loading conditions and (ii) what HCF crack initiation types are observed in finish hard turned 55 HRC 300M steel.

Complete fatigue life results are presented in Figure 46 and compared to MMPDS data [32] generated for polished specimens at the same stress ratio (R = -1) but under axial loading conditions. Overall, both polished and machined specimens tested under rotating bending loading conditions resulted in higher fatigue lives when compared to polished specimens tested under axial fatigue loading conditions showing an influence of loading conditions on fatigue life. However, as reported in Chapter 5, the variation in surface integrity characteristics from one specimen to another cannot explain the corresponding variation in fatigue lives. For this reason, it was decided not to pursue with a model of the type Navarro-Rios to model fatigue life from surface characteristics since such a model assumes that varying surface integrities should lead to different fatigue lives and vice-versa.

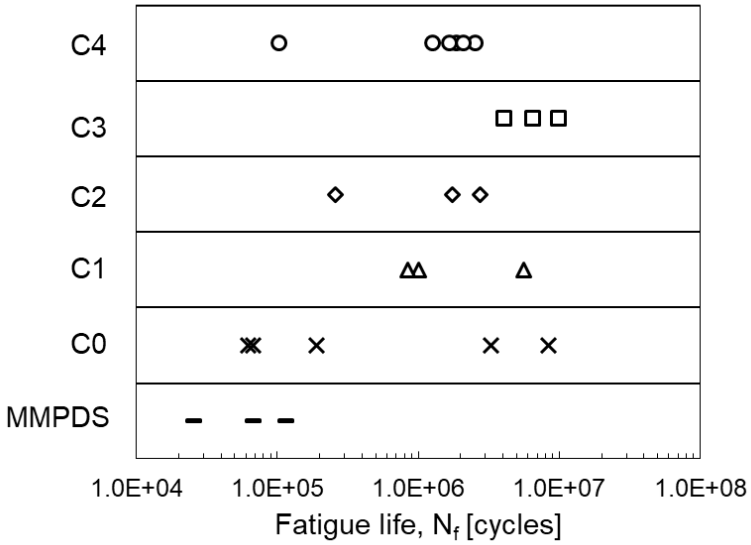

Figure 46: Fatigue life results compared to MMPDS data generated at R = -1 under axial loading conditions. All tests were performed at a maximum stress of 965 MPa.

Fractographic results presented in Chapter 5 showed that apart from cutting condition C2, other conditions generated failures initiating from both feed marks and subsurface inclusions. This is believed to be related to the combination of a high surface roughness (Ra > 1 um) and tensile *ASRS* considering that it is the only cutting condition for which this statement holds true. However, even when considering the existence of two initiation types, no simple statistical model could describe the relationship between surface integrity characteristics and fatigue life in specimens where failure

initiated at feed marks. Moreover, an attempt to compare fatigue lives resulting from specimens with varying surface integrities using a unifying parameter was not successful. In fact, results showed that the use of Murakami's equation for the calculation of K_{max} values underestimated the severity associated with machined surfaces and could not explain the competition between the two crack initiation features observed. This is in agreement with results published by Andreau et al. [92] where Murakami's equation was used to explain the competition between surface and internal crack initiations. Their results demonstrated that although the calculated K_{max} was higher for internal defects in some specimens, crack initiation occurred from surface defects showing that Murakami's equation underestimates the severity of surface defects.

The fractographic results presented in Chapter 5 also showed that where failure initiated from subsurface inclusions, the position of the inclusion was found to be located outside the region of maximum compressive residual stress. This shows that although in-depth residual stresses were not found to influence fatigue life directly, they influenced the position where cracks initiated which is in agreement with results reported by Bag et al. [4] for shot peened 54 HRC 300M steel. Therefore, although fatigue life could not be related to surface characteristics, this result shows that surface integrity characteristics still have an influence on the fatigue behavior of hard turned 55 HRC 300M. However, the nature of this influence could not be established within the scope of the current study which lays the groundwork for future work.

In summary, the fatigue behavior of hard turned 55 HRC 300M steel has been analyzed in terms of fatigue life and crack initiation type. Failures initiated from a surface feed mark in 57% of the specimens while it initiated from a subsurface Al_2O_3-CaO-MgO inclusion in 43% of the specimens. This means that in 43% of all tested machined specimens, the size of surface defects was smaller than that of the largest inclusion contained in the control volume and located outside of the layer affected by machining-induced residual stresses. It was also demonstrated that although the data available for the limited amount of specimens tested did not allow developing a statistical model capable of predicting fatigue life according to surface characteristics, results showed both that in-depth compressive residual stresses were responsible for pushing crack initiation deeper in the material and that the combination of tensile *ASRS* and higher *Ra* lead to surface initiations only.

CHAPTER 7 CONCLUSIONS AND RECOMMENDATIONS

7.1 Conclusions

The objectives of the current project were to determine hard turning cutting conditions under which the surface integrity of 55 HRC 300M steel was optimized for fatigue performance (low surface roughness and compressive surface residual stresses) and to understand the fatigue behavior of finish hard turned 55 HRC 300M steel.

The first study demonstrated that a hybrid Taguchi-PCA-GRA optimization approach proved itself to be effective in solving a problem with complicated relationships between process parameters and allowed evaluating multiple parameters (*T*, *V*, *f*, *D*) and optimizing several responses at the same time (*Ra*, *Rv*, *Rz*, *ASRS*, *HSRS*, *WL*). The results obtained as part of this study are valid for the range of cutting conditions evaluated only and the main conclusions drawn are as follows:

- Because a single optimization method can only optimize one characteristic at a time, the improvement of other surface integrity characteristics is not guaranteed;
- Optimum conditions generated using the hybrid Taguchi-PCA-GRA method allowed decreasing *Ra* by 44% and increasing compressive by 307%;
- The following optimized hard turning cutting conditions allowed generating simultaneously low surface roughness and highly compressive surface residual stresses: *T* = ceramic, *V* = 50 m/min, *f* = 0.051 mm/rev and *D* = 0.762 mm.

The second study demonstrated that the relationship between surface characteristics generated by finish hard turning conditions and fatigue life in 55 HRC 300M steel could not be described by a simple statistical model. The results are valid for the limited range of conditions evaluated and the small number of specimens tested. The main conclusions of this study are the following:

- Although cutting condition C2 generated surface integrity characteristics that are significantly different ($Ra > 1$ μm and tensile *ASRS*) from C1, C3 and C4 ($Ra \ll 1$ μm and compressive *ASRS*), this difference is not reflected by fatigue life results.
- Although a Spearman correlation analysis revealed the existence of a statistically significant correlation between *Ra* & N_f, *Rq* & N_f and *Rsm* & N_f with 95% confidence, no

simple statistical model could model the relationship between those surface roughness parameters and fatigue life.

- Cutting conditions C1, C3 and C4 cannot be optimized further (in terms of fatigue life) because fatigue cracks in specimens machined under such conditions propagate from subsurface inclusions rather from surface feed marks.
- The use of Murakami's equation to generate maximum stress intensity factors was found to be ineffective in assessing the severity associated with surface roughness.

7.2 Recommendations

A few recommendations can be made and divided into two groups. The first recommendation is of interest for the industry while the other recommendations are of interest for future academic projects.

1. Steel cleanliness: As demonstrated in this project, inclusions were responsible for 43% of all fatigue failures in finish hard turned specimens. Therefore, processing of 300M should be improved to make it cleaner because optimizing cutting conditions is useless if cracks are not initiating from the surface.
2. Machining tests: preliminary tests should be performed to assess the capacity of the equipment to be used to machine small diameter specimens. If the material to be tested has a significantly high hardness and/or contains hard particles (e.g. carbides, inclusions), it may be impossible to machine such specimens using conditions characterized with high feed rates and cutting speeds without creating machining defects associated with specimen vibration and/or improper tool engagement in the material.
3. Specimen size: As a result of the previous recommendation and when possible, it is recommended to design specimens with larger diameters in order to lower or eliminate vibration during machining. The use of larger diameters should lower or eliminate the occurrence of machining defects attributed to elevated vibration levels. Specimens with machining defects cannot be tested for fatigue because those defects act as preferential sites for crack initiation.

4. Specimen design: Specimens' grips should be designed with internal fillets because fretting occurs with the collets due to the material's high hardness and possibly to its Si content. Fretting leads to slipping of the specimens during testing and causes material loss both in terms of specimens and collets.
5. Machining conditions: A design of experiment should be developed with roughing conditions to establish if outside finishing conditions, significant correlations exist between surface characteristics and fatigue life in 55 HRC 300M steel.

BIBLIOGRAPHY

1. Zhang, H., H. Zhang, and Y. Lai, *Surface Roughness and Residual Stresses of High Speed Turning 300 M Ultrahigh Strength Steel*. Advances in Mechanical Engineering, Vol. 2014. 2014: p. 1-7.
2. Varela, P.I., C.S. Rakurty, and A.K. Balaji. *Surface integrity in hard machining of 300M Steel: Effect of cutting-edge geometry on machining induced residual stresses*. in Procedia CIRP. 2014.
3. Zheng, G., et al., *Effect of cutting parameters on wear behavior of coated tool and surface roughness in high-speed turning of 300M.* Measurement, 2018. 125: p. 99-108.
4. Bag, A., et al., *Statistical analysis of high cycle fatigue life and inclusion size distribution in shot peened 300M steel.* International Journal of Fatigue, 2019. 118: p. 126-138.
5. Dickinson, G. *The Influence of Machining on the Performance of Ultra High Strength Steels*. in *ASME 1970 International Gas Turbine Conference and Products Show*. American Society of Mechanical Engineers, 1970.
6. Hill, M.R., T.E. Pistochini, and A.T. DeWald, *Fatigue Performance of Laser Peened Materials.* Proceedings of the ASME 2005 Pressure Vessels and Piping Conference. Vol. 7. 2005: p. 203-207.
7. Pistochini, T.E. and M.R. Hill, *Effect of laser peening on fatigue performance in 300M steel.* Fatigue and Fracture of Engineering Materials and Structures, 2011. 34(7): p. 521-533.
8. Totten, G.E., *Effects of Alloying Elements on the Heat Treatment of Steel*, in *Steel Heat Treatment: Metallurgy and Technologies*, C. Press, Editor. 2006. p. 166-211.
9. Liu, F., et al., *Microstructure and mechanical properties of laser solid formed 300M steel.* Journal of Alloys and Compounds, 2015. 621: p. 35-41.
10. Manigandan, K., et al., *Cyclic Strain Resistance, Stress Response, Fatigue Life, and Fracture Behavior of High Strength Low Alloy Steel 300 M.* Journal of Materials Engineering and Performance, 2014. 23(5): p. 1799-1814.
11. Carvalho, S.M.d. and M.S.F.d. Lima, *Laser beam welding tempered 300M ultrahigh mechanical strength steel.* Journal of the Brazilian Society of Mechanical Sciences and Engineering, 2012. 34(1): p. 18-23.
12. Davis J.R., M.K.M., Lampman S.R., *Ultrahigh-Strength Steels*, in *Properties and Selection: Irons, Steels, and High-Performance Alloys*, A. International, Editor. 1990.
13. Matsumoto, Y., F. Hashimoto, and G. Lahoti, *Surface integrity generated by precision hard turning.* CIRP Annals - Manufacturing Technology, 1999. 48(1): p. 59-62.
14. Tönshoff, H.K., C. Arendt, and R.B. Amor, *Cutting of Hardened Steel.* CIRP Annals, 2000. 49(2): p. 547-566.
15. König, W., A. Berktold, and K.F. Koch, *Turning versus Grinding – A Comparison of Surface Integrity Aspects and Attainable Accuracies.* CIRP Annals, 1993. 42(1): p. 39-43.
16. Davim, J.P., *Machining: fundamentals and recent advances*. 2008: Springer Science & Business Media.
17. Altintas, Y., *Manufacturing automation: metal cutting mechanics, machine tool vibrations, and CNC design*. 2012: Cambridge university press.

18. Grzesik, W., *Chapter Three - Trends in Metal Cutting Theory and Pratice*, in *Advanced Machining Processes of Metallic Materials*, W. Grzesik, Editor. 2008, Elsevier: Amsterdam. p. 17-26.
19. Çaydaş, U., *Machinability evaluation in hard turning of AISI 4340 steel with different cutting tools using statistical techniques.* Proceedings of the Institution of Mechanical Engineers, Part B: Journal of Engineering Manufacture, 2010. 224(7): p. 1043-1055.
20. Lima, J.G., et al., *Hard turning: AISI 4340 high strength low alloy steel and AISI D2 cold work tool steel.* Journal of Materials Processing Technology, 2005. 169(3): p. 388-395.
21. Coto, B., et al., *Influences of turning parameters in surface residual stresses in AISI 4340 steel.* The International Journal of Advanced Manufacturing Technology, 2011. 53(9-12): p. 911-919.
22. Navas, V.G., O. Gonzalo, and I. Bengoetxea, *Effect of cutting parameters in the surface residual stresses generated by turning in AISI 4340 steel.* International Journal of Machine Tools and Manufacture, 2012. 61: p. 48-57.
23. Sudhansu, R.D., P. Asutosh, and D. Debabrata, *Hard turning of AISI 4340 steel using coated carbide insert: Surface roughness, tool wear, chip morphology and cost estimation.* Materials Today: Proceedings, 2018. 5(2, Part 2): p. 6560-6569.
24. Chinchanikar, S. and S.K. Choudhury, *Investigations on machinability aspects of hardened AISI 4340 steel at different levels of hardness using coated carbide tools.* International Journal of Refractory Metals and Hard Materials, 2013. 38: p. 124-133.
25. Singh, B.K., B. Mondal, and N. Mandal, *Machinability evaluation and desirability function optimization of turning parameters for Cr2O3 doped zirconia toughened alumina (Cr-ZTA) cutting insert in high speed machining of steel.* Ceramics International, 2016. 42(2, Part B): p. 3338-3350.
26. Suresh, R., et al., *Machinability investigations on hardened AISI 4340 steel using coated carbide insert.* International Journal of Refractory Metals and Hard Materials, 2012. 33: p. 75-86.
27. Rashid, W.B., et al., *Parametric design optimization of hard turning of AISI 4340 steel (69 HRC).* International Journal of Advanced Manufacturing Technology, 2016. 82(1-4): p. 451-462.
28. Zhang, G.D., et al., *High cycle fatigue failure mechanism of 300M ultra-high strength steel and its electron beam welded joints.* Hangkong Cailiao Xuebao/Journal of Aeronautical Materials, 2014. 34(1): p. 69-75.
29. Umezawa, O. *Cyclic damage of some high strength alloys showing subsurface crack generation in high-cycle fatigue*. in Proceedings Second International Symposium on Environmentally Conscious Design and Inverse Manufacturing. 2001.
30. Murakami, Y., *Chapter 16 - Effect of Surface Roughness on Fatigue Strength*, in *Metal Fatigue*, Y. Murakami, Editor. 2002, Elsevier Science Ltd: Oxford. p. 305-320.
31. Campbell, F.C., *14.2 High-Cycle Fatigue*, in *Elements of Metallurgy and Engineering Alloys*. ASM International.
32. Defense, U.S.D.o., *2. Steel*, in *Military Handbook - MIL-HDBK-5H: Metallic Materials and Elements for Aerospace Vehicle Structures (Knovel Interactive Edition)*. 2003, U.S. Department of Defense.

33. Hong, Y., et al., *The formation mechanism of characteristic region at crack initiation for very-high-cycle fatigue of high-strength steels.* International Journal of Fatigue, 2016. 89: p. 108-118.
34. Liu, Y.B., et al., *Dependence of fatigue strength on inclusion size for high-strength steels in very high cycle fatigue regime.* Materials Science and Engineering A, 2009. 517(1-2): p. 180-184.
35. Spriestersbach, D., P. Grad, and E. Kerscher, *Influence of different non-metallic inclusion types on the crack initiation in high-strength steels in the VHCF regime.* International Journal of Fatigue, 2014. 64: p. 114-120.
36. Matsumoto, Y., et al., *Effect of machining processes on the fatigue strength of hardened AISI 4340 steel.* Journal of Manufacturing Science and Engineering, Transactions of the ASME, 1991. 113(2): p. 154-159.
37. Buddy Damm, E. *4340 Steel fatigue initiation and performance in rotating bending fatigue as a function of surface finish and melt practice*. in Materials Science and Technology. 2005.
38. Murakami, Y., S. Kodama, and S. Konuma, *Quantitative evaluation of effects of non-metallic inclusions on fatigue strength of high strength steels. I: Basic fatigue mechanism and evaluation of correlation between the fatigue fracture stress and the size and location of non-metallic inclusions.* International Journal of Fatigue, 1989. 11(5): p. 291-298.
39. Campos, P., et al., *Modeling and optimization techniques in machining of hardened steels: a brief review.* Rev Adv Mater Sci, 2013. 34(2): p. 141-7.
40. Davim, J.P., *Machining of hard materials*. 2011: Springer Science & Business Media.
41. Lin, C.L., *Use of the Taguchi Method and Grey Relational Analysis to Optimize Turning Operations with Multiple Performance Characteristics.* Materials and Manufacturing Processes, 2004. 19(2): p. 209-220.
42. Rajesh, S., et al., *Multi-response optimization of machining parameters on red mud-based aluminum metal matrix composites in turning process.* The International Journal of Advanced Manufacturing Technology, 2013. 67(1): p. 811-821.
43. Tzeng, C.-J., et al., *Optimization of turning operations with multiple performance characteristics using the Taguchi method and Grey relational analysis.* Journal of Materials Processing Technology, 2009. 209(6): p. 2753-2759.
44. Nalbant, M., H. Gökkaya, and G. Sur, *Application of Taguchi method in the optimization of cutting parameters for surface roughness in turning.* Materials and Design, 2007. 28(4): p. 1379-1385.
45. Kuo, Y., T. Yang, and G.-W. Huang, *The use of a grey-based Taguchi method for optimizing multi-response simulation problems.* Engineering Optimization, 2008. 40(6): p. 517-528.
46. McEvily, A.J., *The Growth of Short Fatigue Cracks: A Review.* Materials Science Research International, 1998. 4(1): p. 3-11.
47. Newman, J.C., *A review of modelling small-crack behavior and fatigue-life predictions for aluminum alloys.* Fatigue & Fracture of Engineering Materials & Structures, 1994. 17(4): p. 429-439.
48. Chan, K.S. and J. Lankford, *A crack-tip strain model for the growth of small fatigue cracks.* Scripta Metallurgica, 1983. 17(4): p. 529-532.

49. HOBSON, P.D., *The formulation of a crack growth equation for short cracks*. Fatigue & Fracture of Engineering Materials & Structures, 1982. 5(4): p. 323-327.
50. Navarro, A. and E.R.d. Rios, *A model for short fatigue crack propagation with an interpretation of the short-long crack transition.* Fatigue & Fracture of Engineering Materials & Structures, 1987. 10(2): p. 169-186.
51. Navarro, A. and E.R. de los Rios, A *microstructurally-short fatigue crack growth equation.* Fatigue & Fracture of Engineering Materials & Structures, 1988. 11(5): p. 383-396.
52. De Los Rios, E.R., M. Trull, and A. Levers, *Modelling fatigue crack growth in shot-peened components of Al 2024-T351.* Fatigue & Fracture of Engineering Materials & Structures, 2000. 23(8): p. 709-716.
53. Curtis, S., et al., *Analysis of the effects of controlled shot peening on fatigue damage of high strength aluminium alloys.* International Journal of Fatigue, 2003. 25: p. 59-66.
54. Navarro, A. and E.R. de los Rios, *Short and long fatigue crack growth: A unified model.* Philosophical Magazine A, 1988. 57(1): p. 15-36.
55. Kuroda, M. and T.J. Marrow, *Modelling the effects of surface finish on fatigue limit in austenitic stainless steels.* Fatigue & Fracture of Engineering Materials & Structures, 2008. 31(7): p. 581-598.
56. Prevey, P.S., *X-ray diffraction residual stress techniques.* ASM International, ASM Handbook., 1986. 10: p. 380-392.
57. Delbergue, D., et al. *Comparison of two X-Ray residual stress measurement methods: Sin2 ψ and Cos α, through the determination of a martensitic steel X-Ray elastic constant*. in Residual Stresses 2016: ICRS-10. 2016.
58. Rech, J. and A. Moisan, *Surface integrity in finish hard turning of case-hardened steels.* International Journal of Machine Tools and Manufacture, 2003. 43(5): p. 543-550.
59. Tonshoff, H.K., C. Arendt, and R. Ben Amor, *Cutting of hardened steel.* CIRP Annals - Manufacturing Technology, 2000. 49(2): p. 547-566.
60. Zhang, X., C.R. Liu, and Z. Yao, *Experimental study and evaluation methodology on hard surface integrity.* International Journal of Advanced Manufacturing Technology, 2007. 34(1-2): p. 141-148.
61. Javidi, A., U. Rieger, and W. Eichlseder, *The effect of machining on the surface integrity and fatigue life.* International Journal of Fatigue, 2008. 30(10-11): p. 2050-2055.
62. Akcan, S., et al., *Formation of white layers in steels by machining and their characteristics.* Metallurgical and Materials Transactions A: Physical Metallurgy and Materials Science, 2002. 33(4): p. 1245-1254.
63. Capello, E., et al., *Relaxation of residual stresses induced by turning and shot peening on steels.* Journal of Strain Analysis for Engineering Design, 2004. 39(3): p. 285-290.
64. Chinchanikar, S. and S.K. Choudhury, *Effect of work material hardness and cutting parameters on performance of coated carbide tool when turning hardened steel: An optimization approach.* Measurement: Journal of the International Measurement Confederation, 2013. 46(4): p. 1572-1584.
65. Coto, B., et al., *Influences of turning parameters in surface residual stresses in AISI 4340 steel.* International Journal of Advanced Manufacturing Technology, 2011. 53(9-12): p. 911-919.

66. Çydaş, U., *Machinability evaluation in hard turning of AISI 4340 steel with different cutting tools using statistical techniques.* Proceedings of the Institution of Mechanical Engineers, Part B: Journal of Engineering Manufacture, 2010. 224(7): p. 1043-1055.
67. Sahu, S. and B.B. Choudhury, *Optimization of Surface Roughness Using Taguchi Methodology & Prediction of Tool Wear in Hard Turning Tools.* Materials Today: Proceedings, 2015. 2(4): p. 2615-2623.
68. Huiping, Z., Z. Hongxia, and L. Yinan, *Surface roughness and residual stresses of high speed turning 300 M ultrahigh strength steel.* Advances in Mechanical Engineering, 2014. 2014.
69. Jomaa, W., V. Songmene, and P. Bocher, *An Investigation of Machining-Induced Residual Stresses and Microstructure of Induction-Hardened AISI 4340 Steel.* Materials and Manufacturing Processes, 2016. 31(7): p. 838-844.
70. Agrawal, A., et al., *Prediction of surface roughness during hard turning of AISI 4340 steel (69 HRC).* Applied Soft Computing Journal, 2015. 30: p. 279-286.
71. Mandal, N., B. Doloi, and B. Mondal, *Predictive modeling of surface roughness in high speed machining of AISI 4340 steel using yttria stabilized zirconia toughened alumina turning insert.* International Journal of Refractory Metals and Hard Materials, 2013. 38: p. 40-46.
72. Sohrabpoor, H., S.P. Khanghah, and R. Teimouri, *Investigation of lubricant condition and machining parameters while turning of AISI 4340.* International Journal of Advanced Manufacturing Technology, 2014. 76(9-12): p. 2099-2116.
73. Datta, S., et al., *Application of PCA-based hybrid Taguchi method for correlated multicriteria optimization of submerged arc weld: a case study.* The International Journal of Advanced Manufacturing Technology, 2009. 45(3): p. 276.
74. Wu, F.-C. and C.-C. Chyu, *Optimization of correlated multiple quality characteristics robust design using principal component analysis.* Journal of Manufacturing Systems, 2004. 23(2): p. 134-143.
75. Lu, H.S., et al., *Grey relational analysis coupled with principal component analysis for optimization design of the cutting parameters in high-speed end milling.* Journal of Materials Processing Technology, 2009. 209(8): p. 3808-3817.
76. Fung, C.P. and P.C. Kang, *Multi-response optimization in friction properties of PBT composites using Taguchi method and principle component analysis.* Journal of Materials Processing Technology, 2005. 170(3): p. 602-610.
77. Huang, J.T. and Y.S. Liao, *Optimization of machining parameters of Wire-EDM based on Grey relational and statistical analyses.* International Journal of Production Research, 2003. 41(8): p. 1707-1720.
78. Grzesik, W. and T. Wanat, *Surface finish generated in hard turning of quenched alloy steel parts using conventional and wiper ceramic inserts.* International Journal of Machine Tools and Manufacture, 2006. 46(15): p. 1988-1995.
79. Poulachon, G., Bandyopadhyay, B.P., Jawahir, I.S., Pheulpin, S., Seguin, E., *The influence of the microstructure of hardened tool steel workpiece on the wear of PCBN cutting tools.* International Journal of Machine Tools and Manufacture, 2003. 43(2): p. 139-144.
80. Griffiths, B., *4 - Surface Finish Characterization*, in *Manufacturing Surface Technology*, B. Griffiths, Editor. 2001, Kogan Page Science: Oxford. p. 109-151.

81. Ajaja, J., et al., *Hard turning multi-performance optimization for improving the surface integrity of 300M ultra-high strength steel.* The International Journal of Advanced Manufacturing Technology, 2019.
82. Petropoulos, G.P., C.N. Pandazaras, and J.P. Davim, *Surface Texture Characterization and Evaluation Related to Machining*, in *Surface Integrity in Machining*, J.P. Davim, Editor. 2010, Springer London: London. p. 37-66.
83. Petropoulos, G.P., et al., *Multi-parameter identification and control of turned surface textures.* The International Journal of Advanced Manufacturing Technology, 2006. 29(1): p. 118-128.
84. Pusavec, F., et al., *Surface integrity in cryogenic machining of nickel based alloy—Inconel 718.* Journal of Materials Processing Technology, 2011. 211(4): p. 773-783.
85. Abernethy, R.B., *The New Weibull handbook: reliability and statistical analysis for predicting life, safety, supportability, risk, cost and warranty claims*. 2004: Dr. Robert B. Abernethy.
86. Evans, J.W., R.A. Johnson, and D.W. Green, *Two-and three-parameter Weibull goodness-of-fit tests*. Vol. 493. 1989: US Department of Agriculture, Forest Service, Forest Products Laboratory.
87. Murakami, Y. and H. Usuki, *Quantitative evaluation of effects of non-metallic inclusions on fatigue strength of high strength steels. II: Fatigue limit evaluation based on statistics for extreme values of inclusion size.* International Journal of Fatigue, 1989. 11(5): p. 299-307.
88. Hauke, J. and T. Kossowski, *Comparison of values of Pearson's and Spearman's correlation coefficients on the same sets of data.* Quaestiones geographicae, 2011. 30(2): p. 87-93.
89. Schober, P., C. Boer, and L. A. Schwarte, *Correlation Coefficients: Appropriate Use and Interpretation.* Anesthesia & Analgesia, 2018. 126: p. 1.
90. Itoga, H., et al., *Effect of surface roughness on step-wise S–N characteristics in high strength steel.* International Journal of Fatigue, 2003. 25(5): p. 379-385.
91. Bag, A., et al., *Effect of different shot peening conditions on the fatigue life of 300M steel submitted to high stress amplitudes.* Manuscript submitted for publication, 2019.
92. Andreau O. et al. *A competition between the contour and hatching zones on the high cycle fatigue behaviour of a 316 stainless steel: Analyzed using X-ray computed tomography.* Materials Science and Engineering: A 757 (2019): 146-159.757: p. 146-159.